INLET TURBULENCE GENERATION FOR LARGE EDDY SIMULATION: APPLICATIONS TO FLUID-STRUCTURE INTERACTION PROBLEMS

by

Hugo Guillermo Castro

A dissertation submitted to the Postgraduate Department of the

FACULTAD DE INGENIERÍA Y CIENCIAS HÍDRICAS

for partial fulfillment of the requirements

for the degree of

DOCTOR IN ENGINEERING

Field of Computational Mechanics

of the

UNIVERSIDAD NACIONAL DEL LITORAL

2013

INLET TURBULENCE GENERATION FOR LARGE EDDY SIMULATION: APPLICATIONS TO FLUID-STRUCTURE INTERACTION PROBLEMS

Thesis advisors:

Rodrigo R. Paz   INTEC (CONICET-UNL)
Facultad de Ingeniería y Ciencias Hídricas - UNL

Victorio E. Sonzogni INTEC (CONICET-UNL)
Facultad de Ingeniería y Ciencias Hídricas - UNL

Evaluation committee members:

Dr. César Aguirre   (UNER-CONICET)

Dr. Axel Larreteguy (UADE)

Dr. Jorge Delía   (UNL-CONICET)

FACULTAD DE INGENIERÍA Y CIENCIAS HÍDRICAS

UNIVERSIDAD NACIONAL DEL LITORAL

2013

A mi esposa Vanesa.

A mis abuelas Elba y Milagros.

Acknowledgements

During the development of this dissertation at Centro Internacional de Métodos Computacionales en Ingeniería (CIMEC) I have received help and encouragment from many people which I would like to acknowledge. First of all, I would like to thank Rodrigo Paz who had always time for discussions and suggestions on my work. Without him this thesis would not have been possible. I could never be thankful enough for his guidance.

To Mario Storti and Victorio Sonzogni for their support and interest that they have always shown on my research. It has been a privilege to have worked at CIMEC with such extraordinary people.

To my friends at CIMEC, especially those who had shared so many hours with me since my first trips to Santa Fe. Federico, Juan José and Omar, I will always be grateful that you have honored me with your friendship.

To the Public Education.

To the Universidad Tecnológica Nacional, Facultad Regional Resistencia.

Finally, I would like to thank my family: my mother and father, Hugo and Mercedes, and my brothers, Alejandro and Daniel. To my wife, Vanesa, for the love and patience.

Author's Legal Declaration

This dissertation have been submitted to the Postgraduate Department of the *Facultad de Ingeniería y Ciencias Hídricas* for partial fulfillment of the requirements for the degree of *Doctor in Engineering - Field of Computational Mechanics* of the *Universidad Nacional del Litoral*. A copy of this document will be available at the University Library and it will be subjected to the Library's legal normative.

Some parts of the work presented in this thesis have been published in the following journals: *Latin American Applied Research, Advances in Engineering Software and Journal of Computational Physics*.

Any comment about the ideas and topics discussed and developed through this document will be highly appreciated.

Hugo Guillermo CASTRO

Abstract

The Large Eddy Simulation (LES) method has become practically a standard approach for the resolution of the Navier-Stokes (NS) equations when the simulation of a turbulent flow is required. This is not only due to the high accuracy and feasibility of LES but also to the growing computational power and affordability that have taken place in recent years.

However, there are a number of issues that are still being intensively studied: mesh generation strategies, inlet and boundary conditions, subgrid-scale (SGS) models, among others, in order to extend the set of problems that can be solved by LES or to reduce the computational cost involved. This scenario is further complicated if the fluid-structure interaction (FSI) problem is added: coupling algorithm and mesh moving strategy must be defined for every problem.

A particular field where the Computational Fluid Dynamics (CFD) and FSI meet is in the road vehicle aerodynamics study. Until recently (and even at present days) it has been preferred the experimental rather than numerical simulation of such problems due to the reliability gained by wind tunnels. Nevertheless, this experimental tool has also shortcomings that can be corrected and even strengths that can be improved by the use of numerical simulation.

It is the aim of this thesis to study the applicability of LES on road vehicle aerodynamics including inlet turbulence generation and fluid-structure interaction. In order to do that, a turbulent flow over a simplified car model known as *Ahmed's body* is simulated. The results obtained in this work lead to the conclusion that it is possible to analyze the aerodynamic properties of road vehicle models in a complementary way with experimental and computational tools.

Contents

List of Figures

List of Tables

LIST OF TABLES

Introduction

Motivation

Aerodynamics is the study of a solid body moving through the air and the interaction between the body surface and the surrounding fluid with different relative velocities and directions. Road vehicle aerodynamics add another source of complexity given that the existence of the atmospheric boundary layer (ABL). The wind in the ABL generates a turbulent flow environment, impacting on the mean velocity experienced by the moving vehicle. Furthermore, this turbulence along with the vehicle wake unsteadiness can affect unsteady aerodynamic forces acting on it. If the frequency of these forces matches the natural frequency of the body, it can induce noise and vibrations which could seriously affect the comfort of the driver. The complexity associated with time-varying flows causes that the vast part of the investigations has been limited to the time-averaged behaviour.

Computational Fluid Dynamics (CFD) enable us to perform studies on road vehicle aerodynamics by means of the numerical simulation of the governing equations of the physical system. Owing to the large spread in length and time scales included in the problems mentioned above, it is generally required a high degree of refinement in the finite element (or finite volume) mesh, resulting in a very large computational resource requirement. Newer technologies and even faster and powerful (super-)computers make now possible to solve numerically this kind of complex problems.

In the study of road vehicle aerodynamics it is often assumed that the vehicle is rigid, i.e., its natural frequency being several times greater than the frequency of the more energetic gusts of the flow. However, that is not the case of real vehicles on the

road. They interact with the incident wind, which change of intensity and direction in an unpredictable way and also with bumps and surface imperfections of the road. The interaction between wind and vehicle can be numerically modeled as a fluid-structure interaction (FSI) problem while the road imperfections as an stochastic input force in the system.

In FSI problems, fluid and structure dynamics influence each other: the structure deforms under the effect of the fluid forces and the fluid follows the structure displacement. This interaction means not only that the fluid velocity equals the structure at the interface, but that the domain changes as a consequence of the structure motion.

Even at present days, with huge increases in computing power, the experimental simulation is preferred to the numerical simulation in the study of vehicle aerodynamics and even in the analysis of fluid-structure interaction problems due to the reliability gained by wind tunnels. Nevertheless, this experimental tool has also shortcomings that can be corrected and even strengths that can be improved by using numerical simulation.

The aim of this thesis is to investigate the feasibility of using a computational code to reproduce the experimental conditions in a wind tunnel test section. This study is focused not only on the aerodynamics of a fixed body but also on its dynamic interaction with an incident wind flow.

The overall objective is to demonstrate that the computational codes developed in this work can be used not to replace wind tunnel tests but as complementary tools. This observation is based in the fact that a wind tunnel enables the *measurement* and not the *estimation* of aerodynamic forces, provided that the physics of the fluid flow in the wind tunnel is correct. Also, the wind tunnel has shown a notable correlation with road tests and is a fast, cost-effective and reliable tool (Cooper, 2004). On the other hand, CFD provides the possibility to execute the following tasks:

- to perform a detailed analysis of the problem, isolating any aspect of the body geometry if required,

- to further understand the physics of the problem, by means of powerful visualization tools,

- to modify the test conditions in a time and cost efficient manner.

All these characteristics suggests that, if used with experimental tests complementarily, it would accelerate the development cycle of road vehicles.

Objectives

Two general objectives in this work are pursued. First of all is to propose a synthetic turbulence generator that can be used to provide a physically realistic velocity fluctuating field for LES. Secondly is to numerically simulate the fluid-structure interaction between the air flow and a simplified road vehicle model during an experimental test in a wind tunnel.

These objectives must be implemented in one efficient, robust and accurate computational tool that use finite element technology to solve the problem under study. In order to do that, the PETSc-FEM code (http://www.cimec.org.ar/petscfem) is used. This code is a general purpose, parallel, multiphysics finite element program that has been used in many applications including analysis of petroleum refinery processes, aerospace industry, environmental impact assessment and siderurgical processes (Storti et al., 2002; Paz et al., 2006).

The particular objectives are:

- To review the state of the art for inlet turbulence boundary condition generation and fluid-structure interaction analysis.

- To develop a new methodology for the generation of synthetic turbulence in order to impose inlet boundary conditions in Large Eddy Simulation.

- To numerically simulate the wind tunnel test conditions including wind turbulence and fluid-structure interaction.

Outline

This thesis work is organized as follows:

Chapter 1. As the computational simulations are performed using the Large Eddy Simulation (LES) method, an analysis of this model of the Navier-Stokes equations is made in this Chapter. Furthermore, a review of the different inlet turbulence generation methods is performed.

Chapter 2. In this chapter a synthesized turbulence method based in previous methodologies is developed. A detailed discussion of the method along with several test cases are presented.

Chapter 3. This chapter deals with the basic equations to solve fluid-structure interaction in incompressible flow problems. The coupling strategies for FSI problems are explained. The finite element formulation described in Chapter 1 is extended to account for moving fluid domains by means of the arbitrary Lagrangian-Eulerian formulation. A description of the algorithm for the weak and strong coupling used in this work is made. Finally, an example problem is presented to illustrate the coupling between the structure, fluid and mesh problems.

Chapter 4. In this chapter the study of road vehicle aerodinamics by means of LES is made. All the previously analyzed computational tools, i.e. turbulence synthesis and fluid-structure interaction are applied.

Chapter 5. Here the conclusions and achievements of this work are presented.

Chapter 1

Large Eddy Simulation of Turbulent Flows

1.1 Introduction

Turbulence is a complex phenomenon that it is often found in many natural processes and, as a consequence, has been the subject of study for more than a hundred years. Nowadays, the prediction and manipulation of turbulent flows is of extreme importance due to their implication in many technological applications that goes from transportation systems (cars, buses, aircraft and ships) to geophysical systems (weather prediction, pollutant dispersion). One of the key points for the development of more accurate design and performance of these applications is the need for suitable models of turbulent flows.

Numerical solution of problems that involve turbulent flows can be accomplished by different methodologies, with diverse levels of approximation, yielding more or less detailed descriptions of the state of the flow (Piomelli and Chasnov, 1996). A first approximation to a mathematical description of any turbulent flow can be made by time averaging the equations of motion by means of the well-known Reynolds' averaging process. This results in the Reynolds-averaged Navier-Stokes equations (RANS) which describe the evolution of the mean quantities in the flow. The effects of turbulent fluctuations are included in the Reynolds stress tensor, which introduces additional

1

1. LARGE EDDY SIMULATION OF TURBULENT FLOWS

unknowns to the governing equations that require to be modeled in order to close the system. However, the most commonly used turbulence models for the RANS equations lack generality, since the constants inherent to each model are set according to known theoretical solutions or well-documented experiments. Thus, if such a model is used in flows that are very different from the ones used for calibration, the constants may have to be adjusted in order to yield accurate predictions. This lack of generality in RANS turbulence models is related to the fact that the models must describe the eddies behavior in a very wide range of scales. The small scales of the flow depend mainly on the viscosity and therefore their character is more universal than the large ones, which are influenced very strongly by the boundary conditions. These facts lead to the conclusion that it is not possible to model the effect of large scales in the same way in very different flows.

The most accurate method of solving turbulence in fluids is the direct numerical simulation (DNS) of turbulence in which the domain is discretized in elements that are small enough to resolve even the smallest scales of motion. By this method one can obtain an accurate three-dimensional, time-dependent solution of the Navier-Stokes equations without introducing any modeling assumptions. The DNS approach has been used in the past years for the study of fluid flows with simple boundaries which become turbulent and at present it is feasible only at low or moderate Reynolds numbers (Re). These usage limitations respond to two main subjects. Firstly, it is necessary to use highly accurate, high-order schemes (like spectral methods) to limit dispersion and dissipation errors which tend to have problems in handling complex geometries and general boundary conditions. Secondly, in order to resolve all scales of motion, it is required a number of nodes $N \sim L/\eta$, where L is the computational domain characteristic dimension and η is the smallest scale of motion, known as *Kolmogorov length scale*. Due to this ratio is proportional to $Re^{3/4}$, the number of nodes required by a DNS in three dimensions is $N^3 \sim Re^{9/4}$ (Lesieur, 2008, Sec. 6.6, pp. 205-206). The ratio of the integral time-scale of the flow to the Kolmogorov time scale is also proportional to $Re^{3/4}$, meaning that the number of time-steps required to advance the computation a given fixed period has the same dependence on Re. Assuming that the CPU time required by a computational code is proportional to the number of nodes N, the cost of the simulation will depend on the number of nodes times the number of time-steps, that is, to Re^3. This means that if it is required to double the Reynolds number the computational cost will increase by (at least) a factor of 8.

The intermediate technique between RANS and DNS is known as large-eddy simulation (LES) method. In LES, only the large, energy-carrying structures are fully resolved while the effect of the small scale motions is modeled. Because of the large scale unsteady motions are represented explicitly, LES can be expected to be more accurate and reliable than RANS models for flows in which large-scale unsteadiness is significant, such as the flow over bluff bodies, which involves unsteady separation and vortex shedding (Pope, 2003). LES and DNS provide a three-dimensional, time dependent solution of the Navier-Stokes but the former can be used at much higher Reynolds numbers than DNS. In the following sections several aspects of the theory and application of LES will be discussed.

1.2 Incompressible Navier-Stokes Equations

A number of important phenomena in fluid mechanics are well represented by the Navier-Stokes equations. These equations are a statement of the dynamical effect of the externally applied forces and the internal forces of a fluid which, for the scope of this work, it will assume to be Newtonian.

Let's consider a bounded flow region $\Omega \in \mathbb{R}^{n_{\mathrm{sd}}}$, where n_{sd} is the number of space dimensions, and a temporal domain $(0, t_+]$. The boundary $\Gamma = \partial\Omega$ is assumed to be Lipschitz continuous (a closed and sufficiently regular surface). Thus, the incompressible version of these equations is

$$\rho\left(\frac{\partial \boldsymbol{u}}{\partial t} + \boldsymbol{u} \cdot \nabla \boldsymbol{u}\right) - \nabla \cdot \boldsymbol{\sigma} - \rho \mathbf{g} = \mathbf{0} \qquad \text{in} \ \ \Omega \times (0, t_+] \tag{1.1}$$

$$\nabla \cdot \boldsymbol{u} = 0 \qquad \text{in} \ \ \Omega \times (0, t_+], \tag{1.2}$$

Equation (1.1) represents the conservation of momentum for Newtonian fluids of density ρ and dynamic viscosity μ, under the action of a gravitational field of acceleration $\mathbf{g}$. Also, $\boldsymbol{\sigma} = -p\mathbf{I} + \mu(\nabla \boldsymbol{u} + \nabla \boldsymbol{u}^T)$ is the stress tensor due to pressure p and viscous forces while $\mathbf{I}$ represents the identity tensor. Equation (1.2) expresses the mass conservation of incompressible fluids.

The boundary and initial conditions are

$$
\begin{aligned}
\boldsymbol{u} &= \boldsymbol{u}_D & &\text{on } \Gamma_D \\
\mathbf{n} \cdot \boldsymbol{\sigma} &= \mathbf{h} & &\text{on } \Gamma_N, \\
\boldsymbol{u}(t=0) &= \boldsymbol{u}_0 & &\forall \boldsymbol{x} \in \Omega \\
p(t=0) &= p_0 & &\forall \boldsymbol{x} \in \Omega,
\end{aligned}
\tag{1.3}
$$

where Γ_D and Γ_N are the Dirichlet and Neumann boundaries, respectively, such that

$$
\begin{aligned}
\Gamma_D \cup \Gamma_N &= \Gamma \\
\Gamma_D \cap \Gamma_N &= \emptyset
\end{aligned}
\tag{1.4}
$$

1.2.1 Finite element formulation

The incompressible Navier-Stokes equations present two important difficulties for its solution with a finite element method (Paz, 2006). First, the character of the equation becomes highly advective dominant when the Reynolds number increases. Stabilization techniques, such as Streamline-upwind Petrov-Galerkin (SUPG), Galerkin/Least-Squares (GLS), Sub-Grid Scale (SGS) or Least-Squares (LS) must be used to provide meaningful finite element solutions at high Reynolds numbers (Donea and Huerta, 2003, Sec. 2.4, pp. 59-70).

In addition, the incompressibility condition does not represent an evolution equation but a constraint on the velocity field which must be divergence free. In this way, the role of the pressure variable in the momentum equation (1.1) is to adjust itself instantaneously in order to satisfy the condition of divergence-free velocity. This is a drawback because only some combination of interpolation spaces for velocity and pressure can be used with the Galerkin formulation, namely those ones that satisfy the so-called Ladyzhenskaya-Brezzi-Babuška (LBB) condition. In the formulation of Tezduyar et al. (1992) advection is stabilized with the well known SUPG stabilization term (Hughes and Brooks, 1979; Brooks and Hughes, 1982), and a similar stabilization term, called pressure-stabilizing/Petrov-Galerkin (PSPG) (Tezduyar et al., 1986) is included in order to stabilize incompressibility. In this way, it is possible to use stable equal

order interpolations, i.e. to use equal-order functions without generating oscillations in the pressure field. Once these equations are discretized in space, the resulting system of ODE's is discretized in time with the standard trapezoidal rule (backward Euler and Crank-Nicolson schemes are allowed to be used). The resulting non-linear system of equations is solved iteratively at every time step.

Spatial Discretization. The spatial discretization of the equations (1.1) and (1.2) has equal order for the pressure and velocity and is stabilized through the addition of two operators. Advection at high Reynolds numbers is stabilized with the well known SUPG operator, while the PSPG operator stabilizes the incompressibility condition, which is responsible of the checkerboard pressure modes.

The computational domain Ω is divided in n_{el} finite elements Ω_e, $e = 1, \ldots, n_{\text{el}}$; $\mathcal{E}$ is the set of these elements, and H^{1h} the finite dimensional space defined by

$$H^{1h} = \left\{ \phi^h \mid \phi^h \in C^0(\overline{\Omega}) : \phi^h|_{\Omega^e} \in P^1, \ \forall \Omega^e \in \mathcal{E} \right\}, \tag{1.5}$$

with P^1 representing first-degree polynomials. The functional spaces for the interpolation and test functions are defined as

$$\begin{aligned}
S_{\boldsymbol{u}}^h &= \{ \ \boldsymbol{u}^h \mid \boldsymbol{u}^h \in (H^{1h})^{n_{\text{sd}}}, \ \boldsymbol{u}^h \doteq \boldsymbol{u}_D^h \ \text{ on } \Gamma_D \ \} \\
V_{\boldsymbol{u}}^h &= \{ \ \mathbf{w}^h \mid \mathbf{w}^h \in (H^{1h})^{n_{\text{sd}}}, \ \mathbf{w}^h \doteq \mathbf{0} \ \text{ on } \Gamma_D \ \} \\
S_p^h &= \{ \ q \mid q \in H^{1h} \ \}.
\end{aligned} \tag{1.6}$$

where n_{sd} is the number of space dimensions.

The SUPG-PSPG scheme is then written as follows: *Find $\boldsymbol{u}^h \in S_{\boldsymbol{u}}^h$ and $p^h \in S_p^h$ such that*

$$
\int_\Omega \mathbf{w}^h \cdot \rho\Big(\frac{\partial \boldsymbol{u}^h}{\partial t} + \boldsymbol{u}^h \cdot \nabla \boldsymbol{u}^h\Big)\,d\Omega \ + \int_\Omega \nabla \mathbf{w}^h : \boldsymbol{\sigma}^h\,d\Omega \ - \int_\Omega \mathbf{w}^h \cdot \rho \mathbf{g}\,d\Omega \ +
$$

$$
+ \underbrace{\sum_{e=1}^{n_{\mathrm{el}}} \int_\Omega \tau_{\mathrm{SUPG}}(\boldsymbol{u}^h \cdot \nabla)\mathbf{w}^h \cdot \Big[\rho\Big(\frac{\partial \boldsymbol{u}^h}{\partial t} + \boldsymbol{u}^h \cdot \nabla \boldsymbol{u}^h\Big) - \nabla \cdot \boldsymbol{\sigma}^h - \rho \mathbf{g}\Big]\,d\Omega}_{\text{\textit{(SUPG term)}}} \ +
$$

$$
+ \underbrace{\sum_{e=1}^{n_{\mathrm{el}}} \int_\Omega \tau_{\mathrm{PSPG}}\frac{1}{\rho}\nabla q^h \cdot \Big[\rho\Big(\frac{\partial \boldsymbol{u}^h}{\partial t} + \boldsymbol{u}^h \cdot \nabla \boldsymbol{u}^h\Big) - \nabla \cdot \boldsymbol{\sigma}^h - \rho \mathbf{g}\Big]\,d\Omega}_{\text{\textit{(PSPG term)}}} \ +
$$

$$
+ \int_\Omega q^h \nabla \cdot \boldsymbol{u}^h\,d\Omega = \int_{\Gamma_h} \mathbf{w}^h \cdot \mathbf{h}^h\,d\Gamma, \qquad \forall\,\mathbf{w}^h \in V_{\mathbf{u}}^h\,,\,\forall\,q^h \in S_p^h, \tag{1.7}
$$

where the stabilization parameters are defined as (Tezduyar and Sathe, 2003):

$$
\tau_{\mathrm{SUPG}} = \tau_{\mathrm{PSPG}} = \left(\frac{1}{\tau_1^2} + \frac{1}{\tau_2^2} + \frac{1}{\tau_3^2}\right)^{-\frac{1}{2}},
$$

$$
\tau_1 = \frac{h_{\mathrm{SUPG}}}{2\,||\boldsymbol{u}^h||},
$$

$$
\tau_2 = \frac{\Delta t_{\mathrm{NS}}}{2},
$$

$$
\tau_3 = \rho \frac{h_{\mathrm{SUPG}}^2}{12\,\mu}. \tag{1.8}
$$

Here, Δt_{NS} is the time step size corresponding to a time discretization employing the midpoint rule and the characteristic element length scale along the streamline h_{SUPG} is computed as

$$
h_{\mathrm{SUPG}} = 2\,||\boldsymbol{u}^h|| \left(\sum_{a=1}^{n_{\mathrm{en}}} |\boldsymbol{u}^h \cdot \nabla N_a|\right)^{-1}, \tag{1.9}
$$

being n_{en} the number of nodes in the element and N_a is the shape function associated with node a. Note that the SUPG and the PSPG terms are defined on different functional spaces. These stabilizations terms act, at the linear system level, adding nonzero values on the diagonal entries associated with the pressure equations.

1.2.2 Filtered Navier-Stokes equations

As was mentioned in Sec. 1.1, LES can be viewed as a hybrid approach that performs partial simulation (large eddies) and partial modeling (small eddies). The idea is based on the fact that the large eddies are very dependent on the geometry of the flow, they are anisotropic and have a long lifetime, and therefore their structure will vary from one type of flow to another. On the contrary, the small eddies produced from inertial transfer tend to be more homogeneous and universal.

To separate the large from the small scales, LES is based on the definition of a filtering operation: a filtered (or resolved, large scale) variable, denoted by an overbar, defined as

$$\overline{f}(\boldsymbol{x}) = \int_{\Omega} f(\boldsymbol{x}') \ G(\boldsymbol{x}, \boldsymbol{x}') d\boldsymbol{x}' \tag{1.10}$$

where G is the *filter function*. The filter function determines the size and structure of the small scales. The most commonly-used filter functions are the sharp Fourier cutoff filter, the Gaussian filter and the tophat filter (Piomelli and Chasnov, 1996).

If the filtering operation (1.10) is applied to the governing equations, one obtains the filtered equations of motion, which are solved in large-eddy simulations. For an incompressible flow of a Newtonian fluid, they take the following form, e.g. see Lesieur (2008, Sec. 12.2.1, pp. 420-422):

$$\frac{\partial \overline{u}_i}{\partial x_i} = 0 \tag{1.11}$$

$$\frac{\partial \overline{u}_i}{\partial t} + \frac{\partial}{\partial x_j}(\overline{u}_i \overline{u}_j) = -\frac{1}{\rho}\frac{\partial \overline{p}}{\partial x_i} + \nu \frac{\partial^2 \overline{u}_i}{\partial x_j \partial x_j} + \frac{\partial T_{ij}}{\partial x_j}$$

$$= -\frac{1}{\rho}\frac{\partial \overline{p}}{\partial x_i} + \frac{\partial}{\partial x_j}(2\nu \overline{S}_{ij} + T_{ij}) \tag{1.12}$$

where $\overline{S}_{ij}$ is the large-scale strain-rate tensor,

$$\overline{S}_{ij} = \frac{1}{2}\Big(\frac{\partial \overline{u}_i}{\partial x_j} + \frac{\partial \overline{u}_j}{\partial x_i}\Big) \tag{1.13}$$

and the effect of the small scales appears through a subgrid-scale (SGS) stress term,

$$T_{ij} = \overline{u}_i\overline{u}_j - \overline{u_i u_j} \tag{1.14}$$

that must be modeled. The filtered Navier-Stokes equations written above, govern the evolution of the large, energy-carrying, scales of motion.

By analogy with what is done in the framework of RANS equations, the subgrid-scale tensor is usually expressed in terms of eddy viscosity in the form (Lesieur, 2008, Sec. 12.2.4, pp. 424-425)

$$T_{ij} = 2\nu_t(\boldsymbol{x}, t)\overline{S}_{ij} + \frac{1}{3}T_{kk}\delta_{ij} \tag{1.15}$$

then the equation (1.12) can be written as

$$\frac{\partial \overline{u}_i}{\partial t} + \frac{\partial}{\partial x_j}(\overline{u}_i\overline{u}_j) = -\frac{1}{\rho}\frac{\partial \overline{P}}{\partial x_i} + \frac{\partial}{\partial x_j}\Big[(\nu + \nu_t)\Big(\frac{\partial \overline{u}_i}{\partial x_j} + \frac{\partial \overline{u}_j}{\partial x_i}\Big)\Big] \tag{1.16}$$

where

$$\overline{P} = \overline{p} - \frac{1}{3}\rho T_{kk} \tag{1.17}$$

is a modified pressure (macropressure), which can be determined with the aid of the filtered continuity equation (Lesieur, 2008, Sec. 12.2.4, pp. 424-425).

Smagorinsky's model. The most widely used eddy-viscosity model is the one proposed by Smagorinsky. In his work, an eddy viscosity was introduced in order to take into account subgrid-scale dissipation through a Kolmogorov $k^{-5/3}$ cascade. In fact,

Smagorinsky's model is an adaptation of Prandtl's mixing-length theory to subgrid-scale modeling. In the mixing-length theory the eddy viscosity arising in RANS equations is proportional to a turbulence characteristic length scale multiplied by a turbulence characteristic velocity. Analogously, in the Smagorinsky's model the LES eddy viscosity is proportional to the subgrid-scale characteristic length Δ and to a characteristic subgrid-scale velocity

$$v = \Delta|\overline{S}| \tag{1.18}$$

based on the second invariant of the filtered-field strain rate tensor

$$|\overline{S}| = \sqrt{2\overline{S}_{ij}\overline{S}_{ij}} \tag{1.19}$$

which leads to the definition of the subgrid-scale eddy viscosity

$$\nu_t = (C_S\Delta)^2|\overline{S}| \tag{1.20}$$

Different optimized values for the Smagorinsky coefficient C_S had been proposed depending on the flow characteristics. A theoretical value of this parameter can be derived by considering that the spectrum is a Kolmogorov spectrum,

$$E(k) = C_K\epsilon^{2/3}k^{-5/3} \tag{1.21}$$

with $k \approx 1.4$ and that the filter is a sharp cutoff filter, yielding $C_S \approx 0.18$ (Lilly, 1967). Lower values should be used for shear flows, 0.1 for channel flow for example (Wagner et al., 2007).

Wall bounded flows. Near walls, boundary layers introduce dissipation in the flow, preventing the formation of eddies. In order to account for this effect, the Smagorinsky constant must be reduced to 0 as the boundary is approached. This can be accomplished by the introduction of the van Driest scaling (Berselli et al., 2006, Sec. 3.3.1, p. 78):

$$f_\nu = 1 - \exp(-y^+/A^+) \tag{1.22}$$

where $y^+ = y/y_w$ is the nondimensional distance from the nearest wall expressed in wall units $y_w = \nu/u^*$, where $u^* = (\tau_w/\rho)^{1/2}$ is the local friction speed, τ_w is the local wall shear stress and $A^+ = 25$ is the van Driest constant. The van Driest near-wall damping factor f_ν reduces the "turbulent" kinematic viscosity close to the solid walls but it introduces a non-local effect in the sense that ν_t inside an element also depends on the state of the fluid at the closest wall. It is a near-wall modification of the Prandtl's mixing length turbulence model and was found to be useful in attached flows. It is written in terms of y^+ so that in regions with significant wall friction this factor is relevant only in a thin layer near the body skin. On the other hand, in regions where the local friction speed u_τ takes a very low o null values (usually in the separation and reattachement regions) the influence of the damping factor f_ν is significant at large distance from the body. In order to prevent this drawback, it is possible to restrict it to act within a threshold distance, giving a modified scaling $\tilde{f}_\nu$:

$$\tilde{f}_\nu = f_\nu H(d - y^+) \tag{1.23}$$

where $H(d - y^+)$ is the Heaviside function and d is a certain threshold distance from the body surface. Finally, the "turbulent" viscosity equipped with the modified van Driest scaling and $\Delta = h_e$ being h_e the element size, is written as:

$$\nu_t = C_S^2 h_e^2 \tilde{f}_\nu |\overline{S}| \tag{1.24}$$

1.2.3 Inlet turbulence generation

When turbulent flows are simulated by Large-Eddy Simulation, inflow fluctuations are required to preserve the turbulent characteristics of the upstream flow that is not simulated. This is an important task since LES could demand a high execution time to obtain a fully developed turbulence if the inlet conditions are not properly prescribed, given that the flow behavior within the domain is strongly influenced by the inflow turbulence energy.

In view of these facts, several methods are available for the generation of inlet turbulence conditions and they follow different approaches that can be classified into two general methodologies (Tabor and Baba-Ahmadi, 2010): *precursor simulation methods* and *synthesis methods*. Both approaches present advantages and drawbacks and can be implemented in many different ways.

Precursor simulation methods involve the generation of turbulence by running a precomputation of the simulated flow in order to generate a 'library' or database, before or in concurrency with LES. Then, the generated fluctuations are introduced at the inlet boundary of the computational domain. The relation precomputation/main-calculation can be linked in different ways. If the domain is quite large, the computational implementation through LES may become a difficult task, as it is in the case of a fully developed flow in a pipe. A possible solution is to reintroduce the flow out of a smaller domain into the inlet by mapping the velocity components at the nodes. These *cyclic domains* methods allow to use a short section of the computational domain for the study of fully developed flows and have been used in the Direct Numerical Simulation of a turbulent channel flow (Kim et al., 1987) and in the LES of spatially developing boundary layers by modification of the Spalart method (Lund et al., 1998). Another possibility is to generate a *pre-prepared library* by sampling the data at specific locations of an auxiliary domain (where turbulence precomputation takes place) and storing them for a later introduction into the LES domain as an inlet condition. In particular, Lund et al. (1998) applied their modified Spalart method, in a *concurrent library generation* fashion, sampling the data as the simulation proceeded. An improvement of this methodology has been presented by Liu and Pletcher (2006).

All the precursor methodologies can be integrated into the main domain, sampling the turbulence in a downstream section and then mapping it back into the inlet (Baba-Ahmadi and Tabor, 2009). Thus, precursor simulation methods set the conditions for the LES implementation from a 'real' simulation of turbulence, hence, it is expected that the velocity fluctuation field could possess many of the required statistical characteristics, including energy spectrum, temporal and spatial correlation.

Another widely used methodology is the so called synthesized turbulence method. In this approach a pseudo-random coherent field of fluctuating velocities with spatial and time scales is superimposed on a predefined mean flow. The random perturbations can be generated in several different ways, such as the *Fourier techniques* (with its variants), the *digital filter based method* and the *proper orthogonal decomposition*

1. LARGE EDDY SIMULATION OF TURBULENT FLOWS

(POD) analysis (Tabor and Baba-Ahmadi, 2010). Fourier techniques are frequently implemented for the stochastic generation of turbulent velocities in a computationally efficient way in order to obtain time dependent turbulent fields satisfying statistical features. Basically, it consists of the generation of fluctuating time velocity series with random Fourier modes which are generally obtained by a Monte Carlo simulation with a specific target spectrum (Kondo et al., 1997; Lee et al., 1992; Kraichnan, 1970; Smirnov et al., 2001; Huang et al., 2010). The digital filter method is a signal modeling through the use of linear non-recursive filters which is basically an implementation via digital filters of a Gaussian stochastic process (di Mare et al., 2006; Klein et al., 2003). Xie and Castro (2008) proposed a modified form of this method, based on exponential (rather than Gaussian) velocity correlation functions for the simulation of street-scale flows. The third category is based on the use of POD to interpolate and extrapolate experimental data onto the domain inlet and to model the temporal and spatial characteristics of the flow (Druault et al., 2004). This is probably the least expensive approach (computationally speaking) but with the requirement of a suitable experimental database from hot-wire, Laser Doppler Anemometry (LDA) or Particle Image Velocimetry (PIV) measurements (Perret et al., 2006).

Chapter 2

Synthesized Turbulence Flow

2.1 Introduction

A well known synthetic turbulence generator that employs Fourier techniques is the random flow generation (RFG) method proposed by Smirnov et al. (2001). Developed on the basis of the work of Kraichnan (1970), this methodology involves scaling and orthogonal transformations where a transient flow field is generated in a three-dimensional domain as a superposition of harmonic functions with random coefficients. The method can generate an isotropic divergence-free fluctuating velocity field satisfying the Gaussian's spectral model as well as an inhomogeneous and anisotropic turbulence flow, provided that an anisotropic velocity correlation tensor is given. Smirnov et al. (2001) used their approach to set inlet boundary conditions to LES methods in the simulation of turbulent fluctuations in a ship wake as well as initial boundary conditions in the simulation of turbulent flow around a ship-hull. Another application successfully tested by the authors was the particle dynamics modeling (Smirnov et al., 2005). It should be noted that the RFG method has been included in the computational fluid dynamics (CFD) software FLUENT and was called *Spectral Synthesizer* (Fluent Inc., 2010).

All the features described above were taken into account in the method of Huang et al. (2010), with the advantage that the spatially correlated turbulent flow field can satisfy any arbitrary model spectrum. This property is particularly useful in computational wind engineering applications where the von Kármán model is widely adopted as

a target spectrum and the energy content of the inertial subrange cannot be discarded. Another remarkable feature of this method is its highly parallelizable algorithmic implementation since the generation of the fluctuating velocity series is independent for each node in the inlet plane of the computational domain; to the point that the procedure can be done in an embarrassingly parallel way. As this methodology implies discretizing and synthesizing procedures for the generation of the inlet turbulence the authors called this approach as *discretizing and synthesizing random flow generation* (DSRFG) method.

The results obtained by the application of the DSRFG method were compared with those of the RFG approach in the simulation of the atmospheric boundary layer flow over a prismatic building model (Huang et al., 2010). The authors concluded that the DSRFG method proved to be able to enhance the accuracy of the turbulent flow simulation and wind-induced forces on the building since a more realistic vortices production in the inlet turbulence flow is performed. Nevertheless, only a few comments about the statistical characteristics of the synthesized turbulence were made while there was no discussion about time correlation.

The aim of this Chapter is to propose a synthesized turbulence methodology that is essentially a modification of the DSRFG method. We shall focus on the derivation of the mathematical equations used to generate fluctuating velocity series and the statistical implications of its parameters. In contrast to the DSRFG method, the proposed methodology makes possible to simulate velocity series with an energy content that matches the target values of the physical problem with a desired degree of accuracy. Furthermore, the inclusion of a time scale parameter in the formulation shows that a time scale range of variation can be obtained.

The organization of this Chapter is as follows. Section §2.2 is devoted to the description of the basic mathematical models used for the implementation of inlet turbulence flow conditions, such as spectra, spatial and temporal scales. A review of the DSRFG method is presented in Section §2.3. Then, a detailed derivation of the proposed modifications is performed introducing time and spatial correlations in the mathematical formulation of the velocity fluctuation series. The new approach is then validated in a test case representing an inhomogeneous anisotropic turbulent flow (Section §2.4). Finally, the simulation of a turbulent flow over a simplified model vehicle in a wind tunnel is performed in Section §2.5 using the proposed method to generate the inlet boundary conditions. An extensive analysis and discussion of the obtained results is

made.

2.2   Basic mathematical models

2.2.1   Spectra

One of the characteristics of a turbulent flow is that the velocity field changes in a random fashion in the three space directions and time. The spatial two-point velocity correlation tensor R_{ij}, that is essential to any statistical representation of the turbulence behavior, is defined by

$$R_{ij}(\boldsymbol{x}, t) = \overline{u_i(\boldsymbol{x}, t)u_j(\boldsymbol{x} + \boldsymbol{r}, t)}, \tag{2.1}$$

where u_i is the $i-$th fluctuating velocity component and the over-bar indicates the expected value. If the turbulence is homogeneous, the correlation tensor is a function of the vector separation $\boldsymbol{r}$ only, i.e. $R_{ij}(\boldsymbol{r})$. The energy spectrum tensor Φ_{ij} is defined as the Fourier transform of the correlation tensor (Tennekes and Lumley, 1972, Sec. 8.1, pp. 250-251),

$$\Phi_{ij}(\mathbf{k}) = \frac{1}{(2\pi)^3} \iiint\limits_{-\infty}^{+\infty} \exp(-i\mathbf{k} \cdot \boldsymbol{r}) R_{ij}(\boldsymbol{r}) d\boldsymbol{r},$$
$$R_{ij}(\boldsymbol{r}) = \iiint\limits_{-\infty}^{+\infty} \exp(i\mathbf{k} \cdot \boldsymbol{r}) \Phi_{ij}(\mathbf{k}) d\mathbf{k}, \tag{2.2}$$

where $\mathbf{k}$ is the wave vector. In particular, it can be seen that when $|\boldsymbol{r}| = 0$,

$$R_{ij}(0) = \overline{u_i(\boldsymbol{x}, t)u_j(\boldsymbol{x}, t)} = \iiint\limits_{-\infty}^{+\infty} \Phi_{ij}(\mathbf{k}) d\mathbf{k}, \tag{2.3}$$

showing that $\Phi_{ij}(\mathbf{k})$ represents a density function, in the wave-number space, of contributions to $\overline{u_i(\boldsymbol{x}, t)u_j(\boldsymbol{x}, t)} \equiv \overline{u_i u_j}$. In order to establish the amount of energy (per

unit mass of the fluid) associated with any component of the fluctuating velocity it is necessary and sufficient to determine all components of the tensor $\overline{u_i u_j}$. Thus $\Phi_{ij}(\mathbf{k})$ describes a distribution of energy in $\mathbf{k}$-space (Batchelor, 1982) and the sum of the diagonal components of Φ_{ij} represents the kinetic energy at a given wave-number which is related to equation (2.1) and (2.2) considering $\mathbf{r} = 0$ (Einstein summation convention is assumed),

$$R_{ii}(0) = \overline{u_i u_i} = \overline{u_1^2} + \overline{u_2^2} + \overline{u_3^2} = \iiint\limits_{-\infty}^{+\infty} \Phi_{ii}(\mathbf{k}) d\mathbf{k}. \tag{2.4}$$

Three-dimensional Fourier transforms are suitable for functions of vector arguments but, generally, measurements are made only with respect to one space coordinate. In such conditions a one-dimensional spectrum function $\Theta_{ij}(k_1)$ is obtained (i.e., a Fourier transform of the corresponding unidirectional velocity correlation function) which can be derived by integrating the spectrum tensor Φ_{ij} over the lateral wave vector components. This spectrum function is generally called "longitudinal" spectrum if the direction coincides with x_1 coordinate direction or "lateral" spectrum if it corresponds to the x_2 or x_3 coordinate direction. As an example, the equation for a one-dimensional longitudinal spectrum is

$$\begin{aligned}
\Theta_{11}(k_1) &= \frac{1}{2\pi} \int\limits_{-\infty}^{+\infty} R_{11}(r_1, 0, 0) \, \exp(-ik_1 r_1) \, dr_1, \\
&= \iint\limits_{-\infty}^{+\infty} \Phi_{11}(k_1, k_2, k_3) \, dk_2 \, dk_3.
\end{aligned} \tag{2.5}$$

If we integrate $R_{ij}(\mathbf{r})$ and $\Phi_{ij}(\mathbf{k})$ over spherical shells of radius $r = |\mathbf{r}|$ and $k = |\mathbf{k}|$, respectively,

$$\begin{aligned}
S_{ij}(r) &= \frac{1}{4\pi r^2} \oiint R_{ij}(\mathbf{r}) \, d\boldsymbol{\sigma}(r), \\
\Psi_{ij}(k) &= \oiint \Phi_{ij}(\mathbf{k}) \, d\boldsymbol{\sigma}(k),
\end{aligned} \tag{2.6}$$

where $d\boldsymbol{\sigma}$ is the surface element of the shell, we obtain functions of the position vector magnitude r and the wave vector magnitude k (i.e., the wave number). In the

equations (2.6), $S_{ij}(r)$ represents an average correlation tensor and $\Psi_{ij}(k)$ the energy contribution from wave numbers between k and $k + dk$ to the energy tensor $\overline{u_i u_j}$. Particularly, integrating $\Phi_{ii}(\mathbf{k})$ over a spherical shell, i.e.,

$$E(k) = \frac{1}{2}\Psi_{ii}(k) = \frac{1}{2}\oiint \Phi_{ii}(\mathbf{k})d\boldsymbol{\sigma}, \tag{2.7}$$

the total energy at a wave number k is obtained. That is, the integral of the *energy spectrum function* $E(k)$ is equal to the kinetic energy per unit mass of fluid:

$$\int_0^\infty E(k)dk = \frac{1}{2}\int_0^\infty \left[\oiint \Phi_{ii}(\mathbf{k})d\boldsymbol{\sigma}\right] = \frac{1}{2}\iiint_{-\infty}^\infty \Phi_{ii}(\mathbf{k})\ d\mathbf{k} = \frac{1}{2}\overline{u_i u_i}. \tag{2.8}$$

In isotropic turbulence the energy spectrum function $E(k)$ is somewhat different to the one-dimensional spectrum $\Theta_{11}(k_1)$, which has its maximum value at $k_1 = 0$, while the spherically averaged spectrum approaches to zero as $k \to 0$ (Durbin and Pettersson-Reif, 2001), see figure (2.1).
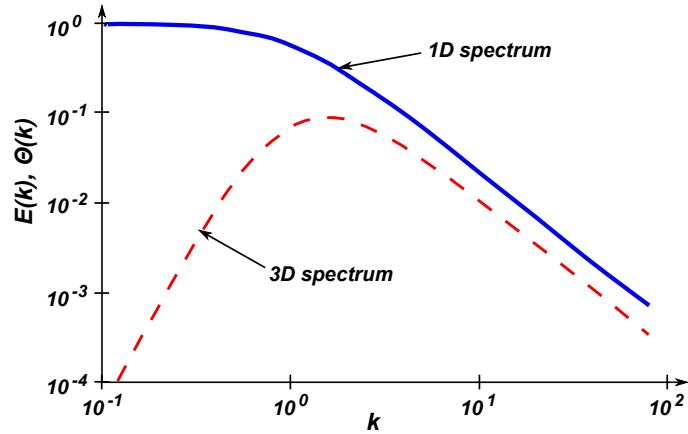
Figure 2.1: Comparison between one-dimensional and three-dimensional von Kármán spectra (Durbin and Pettersson-Reif, 2001).

The importance of defining a one-dimensional spectrum lies in its application to the experimental field since it can be measured as a frequency spectrum at a fixed point and then transformed to a spatial spectrum according to Taylor's hypothesis (frozen turbulence approximation).

2.2.2   Integral length scale

Integral scales of turbulence can be considered as measures of the average size of the eddies present in the turbulent flow. For an isotropic and homogeneous turbulent velocity field the integral length scales based on the two point correlations along the direction j are defined as

$$L_{ik,j}(\boldsymbol{x}) = \int_0^\infty \frac{\overline{u_i(\boldsymbol{x})u_k(\boldsymbol{x}+r\boldsymbol{e}_j)}}{\overline{u_i(\boldsymbol{x})u_k(\boldsymbol{x})}} dr, \tag{2.9}$$

where $\boldsymbol{e}_j$ is the unit vector in the $j-$direction. When the correlation and velocity directions are aligned, e.g. for $L_{11,1}$, a longitudinal integral scale is obtained:

$$L_{11,1} = \int_0^\infty \frac{\overline{u_1 u_1(r_1)}}{\overline{u_1^2}} dr_1 = \frac{1}{\overline{u_1^2}} \int_0^\infty R_{11}(r_1,0,0)\ dr_1, \tag{2.10}$$

where independence of the position $\boldsymbol{x}$ has been introduced. Interestingly, the values of the one-dimensional spectra at zero wave number determine the integral scales of the turbulence field, i.e., if in equation (2.5) $k_1 = 0$ then,

$$\Theta_{11}(0) = \frac{1}{2\pi} \int\limits_{-\infty}^{+\infty} R_{11}(r_1,0,0)\ dr_1 = \frac{\overline{u_1^2}}{\pi}\ L_{11,1}, \tag{2.11}$$

having used equation (2.10) and given that R_{11} is an even function.

2.2.3   Time scale

The spectra defined in Section §2.2.1 are related to velocity correlations taken from two different points in space at the same time. If a fixed point in space is considered, a Fourier transform of the correlation function of a varying time delay defines the time spectra $\psi_{ij}(\omega)$ (Tennekes and Lumley, 1972):

$$R_{ij} = \overline{u_i(\boldsymbol{x},t)u_j(\boldsymbol{x},t+\tau)} = \int_{-\infty}^\infty \exp(i\omega\tau)\ \psi_{ij}(\omega)\ d\omega,$$

where

$$\psi_{ij}(\omega) = \frac{1}{2\pi} \int_{-\infty}^{\infty} \exp(-i\omega\tau) \ R_{ij}(\tau) \ d\tau.$$

In homogeneous turbulence, the value of $\mathrm{tr}(\psi_{ij}(\omega))$ at $\omega = 0$ defines the integral time scale:

$$\psi_{ii}(0) = \frac{1}{2\pi} \int_{-\infty}^{\infty} R_{ii}(\tau) \ d\tau = \frac{T}{\pi}\overline{u_i u_i}, \tag{2.12}$$

where T is the Eulerian integral time scale.

2.3   A modified method to synthesize inlet turbulence

Huang et al. (2010) proposed a turbulence synthesis method called "discretizing and synthesizing random flow generation" (DSRFG) for the implementation of inlet turbulence conditions to perform LES. This method proved to have several advantages with respect to its predecessor, the random flow generation (RFG) by Smirnov et al. (2001). Nevertheless, a re-analysis of the DSRFG equations demonstrates that further improvements can be made. According to this, a brief description of the DSRFG method is performed in this section along with the introduction of the proposed modifications. For a more detailed discussion about the RFG and DSRFG methods, the reader is encouraged to refer to the original articles (Smirnov et al., 2001; Huang et al., 2010).

Following the DSRFG method, a homogeneous and isotropic turbulent flow velocity field $\boldsymbol{u}(\boldsymbol{x}, t)$ can be synthesized as follows:

$$u_i(\boldsymbol{x}, t) = \sum_{m=1}^{M} \sum_{n=1}^{N} \left[p_i^{m,n} \cos(\tilde{k}_j^{m,n}\tilde{x}_j + \omega_{m,n}t) + q_i^{m,n} \sin(\tilde{k}_j^{m,n}\tilde{x}_j + \omega_{m,n}t) \right], \tag{2.13}$$

where

$$\mathbf{p}^{m,n} = \frac{\boldsymbol{\zeta} \times \mathbf{k}^{m,n}}{|\boldsymbol{\zeta} \times \mathbf{k}^{m,n}|} \sqrt{a \frac{4E(k_m)}{N}}, \tag{2.14}$$

$$\mathbf{q}^{m,n} = \frac{\boldsymbol{\xi} \times \mathbf{k}^{m,n}}{|\boldsymbol{\xi} \times \mathbf{k}^{m,n}|} \sqrt{(1-a) \frac{4E(k_m)}{N}}, \tag{2.15}$$

$$\tilde{\mathbf{x}} = \frac{\mathbf{x}}{L_s}, \tag{2.16}$$

$$\tilde{\mathbf{k}}^{m,n} = \frac{\mathbf{k}^{m,n}}{k_0}, \tag{2.17}$$

with $\omega_{m,n} \in N(0, 2\pi f_m)$, $f_m = k_m U_{\text{avg}}$, a is a random number uniformly distributed between 0 and 1, $\boldsymbol{\zeta}$ and $\boldsymbol{\xi}$ are the vector form of ζ_i^n and ξ_i^n, which are random numbers selected independently from $N(0,1)$. Here, $N(\mu, \sigma)$ represents a normal distribution with mean μ and standard deviation σ. In equations (2.16) and (2.17) L_s is a scale factor related to the length scale of turbulence and k_0 is the lowest wavenumber of the discrete spectrum.

The factors $p_i^{m,n}$ and $q_i^{m,n}$ define the distribution of the three dimensional energy spectrum $E(k_m)$ in each of the spatial coordinate axes which in turn are functions of the space wave number $\mathbf{k}^{m,n}$ ($|\mathbf{k}^{m,n}| = k_m$) and normal random vectors $\boldsymbol{\zeta}$ and $\boldsymbol{\xi}$. When dealing with homogeneous and isotropic turbulence, the distribution of $\mathbf{k}^{m,n}$ is isotropic on the surface of a sphere and consequently the energy is uniformly distributed in space. In such conditions it is evident that the same spectrum will be obtained in the three principal directions but in the case of inhomogeneous and anisotropic turbulence the distribution of $\mathbf{k}^{m,n}$ must change according to the conditions of inhomogeneity and anisotropy.

To achieve this behavior, $p_i^{m,n}$ and $q_i^{m,n}$ must be *aligned* with the energy spectrum along a principal direction and, then, the distribution of $\mathbf{k}^{m,n}$ can be *remapped* on the surface of the sphere. To summarize, the method is implemented using equation (2.13) and

$$p_i^{m,n} = \text{sign}(r_i^{m,n})\sqrt{\frac{4}{N}E_i(k_m)\frac{(r_i^{m,n})^2}{1+(r_i^{m,n})^2}}, \tag{2.18}$$

$$q_i^{m,n} = \text{sign}(r_i^{m,n})\sqrt{\frac{4}{N}E_i(k_m)\frac{1}{1+(r_i^{m,n})^2}}, \tag{2.19}$$

$$\mathbf{k}^{m,n} \cdot \mathbf{p}^{m,n} = 0, \tag{2.20}$$

$$\mathbf{k}^{m,n} \cdot \mathbf{q}^{m,n} = 0, \tag{2.21}$$

$$|\mathbf{k}^{m,n}| = k_m, \tag{2.22}$$

where $r_i^{m,n}$ is a random number, independently selected from a three dimensional Normal distribution with zero mean ($\mu_r = 0$) and rms value of one ($\sigma_r = 1$).

In the following, we made some considerations about the statistical implications of the DSRFG method with the aim to expose the concepts behind the modifications that are to be introduced later. The mean square value of a random function $f(t)$ is defined as (Bendat and Piersol, 1967):

$$f_{\text{rms}}^2(t) = \lim_{T\to\infty}\frac{1}{T}\int_0^T f^2(t)\ dt \tag{2.23}$$

and regarding equation (2.13), we have in each direction $i = 1, 2, 3$:

$$u_{\text{rms},i}^2(\boldsymbol{x},t) = \lim_{T\to\infty}\frac{1}{T}\int_0^T \Big\{ \sum_{m=1}^{M}\sum_{n=1}^{N}[p_i^{m,n}\cos(\tilde{k}_j^{m,n}\tilde{x}_j + \omega_{m,n}t) + \\ q_i^{m,n}\sin(\tilde{k}_j^{m,n}\tilde{x}_j + \omega_{m,n}t)]\Big\}^2 dt. \tag{2.24}$$

Defining,

$$\begin{aligned}
\alpha_{m,n} &= p_i^{m,n}\cos(\tilde{k}_j^{m,n}\tilde{x}_j + \omega_{m,n}t) \\
\varphi_{m,n} &= q_i^{m,n}\sin(\tilde{k}_j^{m,n}\tilde{x}_j + \omega_{m,n}t),
\end{aligned} \tag{2.25}$$

and noting that

$$
\begin{aligned}
\Big[\sum_{m=1}^{M} \sum_{n=1}^{N} (\alpha_{m,n} + \varphi_{m,n}) \Big]^2 &= \Big(\sum_{m=1}^{M} \sum_{n=1}^{N} \alpha_{m,n} + \sum_{m=1}^{M} \sum_{n=1}^{N} \varphi_{m,n} \Big)^2 \\
&= \Big(\sum_{m=1}^{M} \sum_{n=1}^{N} \alpha_{m,n} \Big)^2 + 2 \sum_{m=1}^{M} \sum_{n=1}^{N} \sum_{r=1}^{M} \sum_{s=1}^{N} \alpha_{m,n} \varphi_{r,s} + \\
&\quad + \Big(\sum_{m=1}^{M} \sum_{n=1}^{N} \varphi_{m,n} \Big)^2,
\end{aligned} \tag{2.26}
$$

equation (2.24) can be written as

$$
\begin{aligned}
\lim_{T \to \infty} \frac{1}{T} \int_0^T \Big[\sum_{m=1}^{M} \sum_{n=1}^{N} (\alpha_{m,n} + \varphi_{m,n}) \Big]^2 dt &= \lim_{T \to \infty} \frac{1}{T} \int_0^T \Big(\sum_{m=1}^{M} \sum_{n=1}^{N} \alpha_{m,n} \Big)^2 dt + \\
&\quad + \lim_{T \to \infty} \frac{1}{T} \int_0^T \Big(\sum_{m=1}^{M} \sum_{n=1}^{N} \varphi_{m,n} \Big)^2 dt,
\end{aligned} \tag{2.27}
$$

where the following integration result was used:

$$
\begin{aligned}
\lim_{T \to \infty} \frac{1}{T} &\int_0^T \alpha_{m,n} \varphi_{r,s} \, dt \\
&= p_i^{m,n} q_i^{r,s} \lim_{T \to \infty} \frac{1}{T} \int_0^T \cos(\tilde{k}_j^{m,n} \tilde{x}_j + \omega_{m,n} t) \, \sin(\tilde{k}_j^{r,s} \tilde{x}_j + \omega_{r,s} t) \, dt \\
&= p_i^{m,n} q_i^{r,s} \lim_{T \to \infty} \frac{1}{2T(\omega_{r,s} + \omega_{m,n})} \bigg\{ -\cos\big[(\tilde{k}_j^{r,s} + \tilde{k}_j^{m,n}) \tilde{x}_j + (\omega_{r,s} + \omega_{m,n}) t \big] - \\
&\quad - \cos\big[(\tilde{k}_j^{r,s} - \tilde{k}_j^{m,n}) \tilde{x}_j + (\omega_{r,s} - \omega_{m,n}) t \big] \bigg\}_0^T = 0.
\end{aligned}
$$
$$ \tag{2.28} $$

Furthermore, equation (2.27) can be rewritten as

$$\lim_{T\to\infty} \frac{1}{T} \int_0^T \Big[\sum_{m=1}^M \sum_{n=1}^N (\alpha_{m,n} + \varphi_{m,n}) \Big]^2 dt$$

$$= \lim_{T\to\infty} \frac{1}{T} \int_0^T \Big(\sum_{m=1}^M \sum_{n=1}^N \alpha_{m,n}^2 + \sum_{\substack{m=1 \ n=1 \ r=1 \ s=1 \\ m\neq r, n\neq s}}^M \sum_{}^N \sum_{}^M \sum_{}^N \alpha_{m,n}\alpha_{r,s} \Big) dt +$$

$$+ \lim_{T\to\infty} \frac{1}{T} \int_0^T \Big(\sum_{m=1}^M \sum_{n=1}^N \varphi_{m,n}^2 + \sum_{\substack{m=1 \ n=1 \ r=1 \ s=1 \\ m\neq r, n\neq s}}^M \sum_{}^N \sum_{}^M \sum_{}^N \varphi_{m,n}\varphi_{r,s} \Big) dt \qquad (2.29)$$

$$= \lim_{T\to\infty} \frac{1}{T} \sum_{m=1}^M \sum_{n=1}^N \int_0^T \alpha_{m,n}^2 dt + \lim_{T\to\infty} \frac{1}{T} \sum_{m=1}^M \sum_{n=1}^N \int_0^T \varphi_{m,n}^2 dt,$$

where the terms

$$\lim_{T\to\infty} \frac{1}{T} \int_0^T \sum_{\substack{m=1 \ n=1 \ r=1 \ s=1 \\ m\neq r, n\neq s}}^M \sum_{}^N \sum_{}^M \sum_{}^N \alpha_{m,n}\alpha_{r,s} \; dt,$$

$$\lim_{T\to\infty} \frac{1}{T} \int_0^T \sum_{\substack{m=1 \ n=1 \ r=1 \ s=1 \\ m\neq r, n\neq s}}^M \sum_{}^N \sum_{}^M \sum_{}^N \varphi_{m,n}\varphi_{r,s} \; dt, \qquad (2.30)$$

vanish as $T \to \infty$. Then, using the result of equation (2.29) and by virtue of equations (2.24) and (2.25):

$$u_{\text{rms},i}^2(\boldsymbol{x}, t) = \lim_{T\to\infty} \frac{1}{T} \int_0^T \Big[\sum_{m=1}^M \sum_{n=1}^N (\alpha_{m,n} + \varphi_{m,n}) \Big]^2 dt$$

$$= \lim_{T\to\infty} \frac{1}{T} \sum_{m=1}^M \sum_{n=1}^N [p_i^{m,n}]^2 \int_0^T [\cos(\tilde{k}_j^{m,n}\tilde{x}_j + \omega_{m,n}t)]^2 dt +$$

$$+ \lim_{T\to\infty} \frac{1}{T} \sum_{m=1}^M \sum_{n=1}^N [q_i^{m,n}]^2 \int_0^T [\sin(\tilde{k}_j^{m,n}\tilde{x}_j + \omega_{m,n}t)]^2 dt \qquad (2.31)$$

$$= \frac{1}{2} \sum_{m=1}^M \sum_{n=1}^N [p_i^{m,n}]^2 + \frac{1}{2} \sum_{m=1}^M \sum_{n=1}^N [q_i^{m,n}]^2.$$

Now, by summing both sides of the equation (2.31) for $i = 1, 2, 3$:

$$\sum_{i=1}^{3} u_{\text{rms},i}^2(\boldsymbol{x}, t) = \frac{1}{2} \sum_{m=1}^{M} \sum_{n=1}^{N} \sum_{i=1}^{3} [p_i^{m,n}]^2 + \frac{1}{2} \sum_{m=1}^{M} \sum_{n=1}^{N} \sum_{i=1}^{3} [q_i^{m,n}]^2, \qquad (2.32)$$

or in a more compact form (using the Einstein summation convention):

$$\begin{aligned}
\overline{u_i u_i} &= \frac{1}{2} \sum_{m=1}^{M} \sum_{n=1}^{N} p_i^{m,n} p_i^{m,n} + \frac{1}{2} \sum_{m=1}^{M} \sum_{n=1}^{N} q_i^{m,n} q_i^{m,n} \\
&= 2 \int_0^{\infty} E(k) dk \ \approx \ 2 \sum_{m=1}^{M} E(k_m) \Delta k_m,
\end{aligned} \qquad (2.33)$$

where the result of equation (2.8) was used. Now, according to the definition of $p_i^{m,n}$ and $q_i^{m,n}$, if they are replaced by the equations (2.18) and (2.19) in equation (2.33), it can be seen that

$$\begin{aligned}
\overline{u_i u_i} &= \frac{1}{2} \sum_{m=1}^{M} \sum_{n=1}^{N} \sum_{i=1}^{3} \Big[\frac{4}{N} E_i(k_m) \frac{(r_i^{m,n})^2}{1 + (r_i^{m,n})^2} + \frac{4}{N} E_i(k_m) \frac{1}{1 + (r_i^{m,n})^2} \Big] \\
&= \frac{2}{N} \sum_{m=1}^{M} \sum_{n=1}^{N} E(k_m) = 2 \sum_{m=1}^{M} E(k_m),
\end{aligned} \qquad (2.34)$$

which leads to an expression with different units. Furthermore, as $E(k_m)$ is a positive quantity for any k_m value, the resultant kinetic energy has a strong dependence on the number of points M considered to discretize the target spectrum.

2.3.1 Time and spatial correlation

The time autocorrelation function gives information about how correlated is the signal at two different times in a same point of the space and its connection to the time

spectra was pointed out in section §2.2.3. Following equations (2.13) and (2.23) the autocorrelation function can be computed as

$$
\begin{aligned}
\overline{u_i(\boldsymbol{x},t)u_i(\boldsymbol{x},t+\tau)} &= \lim_{T\to\infty} \frac{1}{T}\int_0^T u_i(\boldsymbol{x},t)u_i(\boldsymbol{x},t+\tau)dt \\
&= \lim_{T\to\infty} \frac{1}{T}\int_0^T \sum_{m=1}^M \sum_{n=1}^N \Big[p_i^{m,n}\cos(\tilde{k}_j^{m,n}\tilde{x}_j + \omega_{m,n}t) + \\
&\quad + q_i^{m,n}\sin(\tilde{k}_j^{m,n}\tilde{x}_j + \omega_{m,n}t)\Big] \sum_{m=1}^M \sum_{n=1}^N \Big[p_i^{m,n}\cos(\tilde{k}_j^{m,n}\tilde{x}_j + \\
&\quad + \omega_{m,n}(t+\tau)) + q_i^{m,n}\sin(\tilde{k}_j^{m,n}\tilde{x}_j + \omega_{m,n}(t+\tau))\Big] dt,
\end{aligned}
\tag{2.35}
$$

then, after some mathematical manipulation using equations (2.18) and (2.19),

$$
\begin{aligned}
\overline{u_i(\boldsymbol{x},t)u_i(\boldsymbol{x},t+\tau)} &= \sum_{m=1}^M \sum_{n=1}^N \Big[(p_i^{m,n})^2 \frac{\cos(\tau\omega_{m,n})}{2} + p_i^{m,n}q_i^{m,n}\frac{\sin(\tau\omega_{m,n})}{2} \\
&\quad - p_i^{m,n}q_i^{m,n}\frac{\sin(\tau\omega_{m,n})}{2} + (q_i^{m,n})^2\frac{\cos(\tau\omega_{m,n})}{2}\Big] \\
&= \sum_{m=1}^M \sum_{n=1}^N \frac{2}{N}E_i(k_m)\cos(\tau\omega_{m,n}).
\end{aligned}
\tag{2.36}
$$

Note that, if $\tau = 0$ then equation (2.36) gives back the equation (2.31). Likewise, an expression for the spatial correlation can be obtained in an analogous way:

$$
\begin{aligned}
\overline{u_i(\boldsymbol{x},t)u_i(\boldsymbol{x'},t)} &= \sum_{m=1}^M \sum_{n=1}^N (p_i^{m,n})^2 \frac{\cos[\tilde{k}_j^{m,n}(\tilde{x}'_j - \tilde{x}_j)]}{2} + (q_i^{m,n})^2 \frac{\cos[\tilde{k}_j^{m,n}(\tilde{x}'_j - \tilde{x}_j)]}{2} \\
&= \sum_{m=1}^M \sum_{n=1}^N \frac{2}{N}E_i(k_m)\cos\left[\tilde{k}_j^{m,n}\frac{(x'_j - x_j)}{L_s}\right]
\end{aligned}
\tag{2.37}
$$

Again, equations (2.36) and (2.37) do not present the same units that equation (2.33).

Furthermore, it can be seen that while in equation (2.37) a *scaling length parameter* L_s (that provides a way to obtain the required spatial correlation in the generated flow field) exists, there is not an analogous parameter in equation (2.36).

2.3.2 Proposed methodology

In the light of the analysis above, there are proposed some modifications to the equations of the DSRFG method. Firstly, the Fourier series in equation (2.13) will be written as:

$$
\begin{aligned}
u_i(\boldsymbol{x}, t) = \sum_{m=1}^{M} \sum_{n=1}^{N} \Big[& p_i^{m,n} \cos\left(\tilde{k}_j^{m,n} \tilde{x}_j + \omega_{m,n} \frac{t}{\tau_0}\right) \\
& + q_i^{m,n} \sin\left(\tilde{k}_j^{m,n} \tilde{x}_j + \omega_{m,n} \frac{t}{\tau_0}\right) \Big].
\end{aligned} \tag{2.38}
$$

The inclusion of a parameter that modifies the time t is based on the work of Smirnov et al. (2001) and Batten et al. (2004) although with a different physical meaning: here, τ_0 is not the turbulence time scale but a dimensionless parameter introduced in equation (2.38) to allow some "control" over the time correlation of the generated velocity series.

As it was previously shown by equation (2.33), the turbulent flow energy is related to the three dimensional energy spectrum $E(k_m)$ and the factors $p_i^{m,n}$ and $q_i^{m,n}$. As stated by Huang et al. (2010), these factors align the energy spectrum according to the anisotropy conditions of the turbulence, providing a synthesized velocity series that must satisfy the mean square values on each spatial direction. Starting from these considerations and noticing that from equation (2.34) the resultant kinetic energy has a strong dependence on the number of points M considered to discretize the target spectrum, it is required an alternative analysis to ensure that the synthetic turbulence intensity can represents adequately the flow to be simulated. In this thesis it is performed a simple "decoupling" procedure over equation (2.33), using the following relationship:

$$
\sum_{i=1}^{3} u_{\mathrm{rms},i}^2 = 2 \sum_{m=1}^{M} E(k_m) \Delta k_m = 2 \sum_{m=1}^{M} \sum_{i=1}^{3} c_i E_i(k_m) \Delta k_m. \tag{2.39}
$$

This equation implies that the three-dimensional energy spectrum $E(k)$ is a weighted sum of modified one-dimensional energy spectra aligned with the three principal directions. Some discussion about the consequences of this representation will be given in Section §2.4.

In equation (2.39) c_i is a function value that depends on the form of the spectrum in order to satisfy the condition

$$u_{\text{rms},i}^2 = 2c_i \int_0^\infty E_i(k) \ dk, \tag{2.40}$$

i.e., in each direction the variance of the simulated velocity series must satisfy the equation (2.40). Then,

$$\sum_{i=1}^3 u_{\text{rms},i}^2 = 2 \sum_{i=1}^3 \int_0^\infty c_i E_i(k) \ dk = 2 \int_0^\infty E(k) \ dk. \tag{2.41}$$

Thereby, for each direction i it is obtained a modified version of the equations (2.18) and (2.19):

$$p_i^{m,n} = \text{sign}(r_i^{m,n}) \sqrt{\frac{4c_i}{N} E_i(k_m) \Delta k_m \frac{(r_i^{m,n})^2}{1 + (r_i^{m,n})^2}}, \tag{2.42}$$

$$q_i^{m,n} = \text{sign}(r_i^{m,n}) \sqrt{\frac{4c_i}{N} E_i(k_m) \Delta k_m \frac{1}{1 + (r_i^{m,n})^2}}. \tag{2.43}$$

Furthermore, equation (2.36) is written as

$$\overline{u_i(\boldsymbol{x},t)u_i(\boldsymbol{x},t+\tau)} = \frac{2c_i}{N} \sum_{m=1}^M \sum_{n=1}^N E_i(k_m) \Delta k_m \cos\left(\frac{\tau}{\tau_0}\omega_{m,n}\right), \tag{2.44}$$

while equation (2.37) changes to

$$\overline{u_i(\boldsymbol{x},t)u_i(\boldsymbol{x'},t)} = \frac{2c_i}{N} \sum_{m=1}^{M} \sum_{n=1}^{N} E_i(k_m)\Delta k_m \cos\left[\tilde{k}_j^{m,n}\frac{(x'_j - x_j)}{L_s}\right]. \tag{2.45}$$

As in the DSRFG method, the spatial scaling parameter L_s is computed as

$$L_s = \theta_1 \ \sqrt{L_u^2 + L_v^2 + L_w^2}, \tag{2.46}$$

where θ_1 varies between 1 and 2, while the dimensionless time-correlation parameter τ_0 is a scalar quantity which is further analyzed in the next section. Since this new methodology is based on the DSRFG approach, it is called *modified discretizing and synthesizing random flow generation* (MDSRFG).

2.4   Validation of the procedure

The first test performed is the simulation of an inhomogeneous anisotropic turbulent flow field. This example was proposed by Huang et al. (2010). The spectra of the three principal velocity components are described by the von Kármán models:

$$S_u(f) = \frac{4(I_u U_{\text{avg}})^2(L_u/U_{\text{avg}})}{[1 + 70.8(fL_u/U_{\text{avg}})^2]^{5/6}}, \tag{2.47}$$

$$S_v(f) = \frac{4(I_v U_{\text{avg}})^2(L_v/U_{\text{avg}})[1 + 188.4 \ (2fL_v/U_{\text{avg}})^2]}{[1 + 70.8 \ (2fL_v/U_{\text{avg}})^2]^{11/6}}, \tag{2.48}$$

$$S_w(f) = \frac{4(I_w U_{\text{avg}})^2(L_w/U_{\text{avg}})[1 + 188.4 \ (2fL_w/U_{\text{avg}})^2]}{[1 + 70.8 \ (2fL_w/U_{\text{avg}})^2]^{11/6}}. \tag{2.49}$$

The turbulence intensity values are $I_u = 8\%$, $I_v = 16\%$ and $I_w = 24\%$, while the turbulence integral length scales are $L_u = 0.6$ m, $L_v = 0.3$ m and $L_w = 0.1$ m. Firstly, the c_i values in equations (2.42) and (2.43) must be obtained using the relationship (2.40), that is

$$u_{\text{rms},1}^2 = (I_u U_{\text{avg}})^2 = 2c_1 \int_0^\infty S_u(k) dk$$

$$\approx 2c_1 \ 0.2377 \ \beta\Big(\frac{1}{3}, \frac{1}{2}\Big) I_u^2 U_{\text{avg}} \ \Rightarrow \ c_1 = \frac{U_{\text{avg}}}{2}, \tag{2.50}$$

where $\beta(,)$ is the Beta function (Abramowitz and I., 1970). In the same way, c_2 and c_3 are

$$u_{\text{rms},2}^2 = (I_v U_{\text{avg}})^2 = 2c_2 \int_0^\infty S_v(k) dk$$

$$\approx 2c_2 \left[0.1189 \ \beta\Big(\frac{1}{2}, \frac{4}{3}\Big) + 0.3163 \ \beta\Big(\frac{1}{3}, \frac{3}{2}\Big)\right] I_v^2 U_{\text{avg}} \tag{2.51}$$

$$\Rightarrow \ c_2 = c_3 \approx \frac{U_{\text{avg}}}{2}.$$
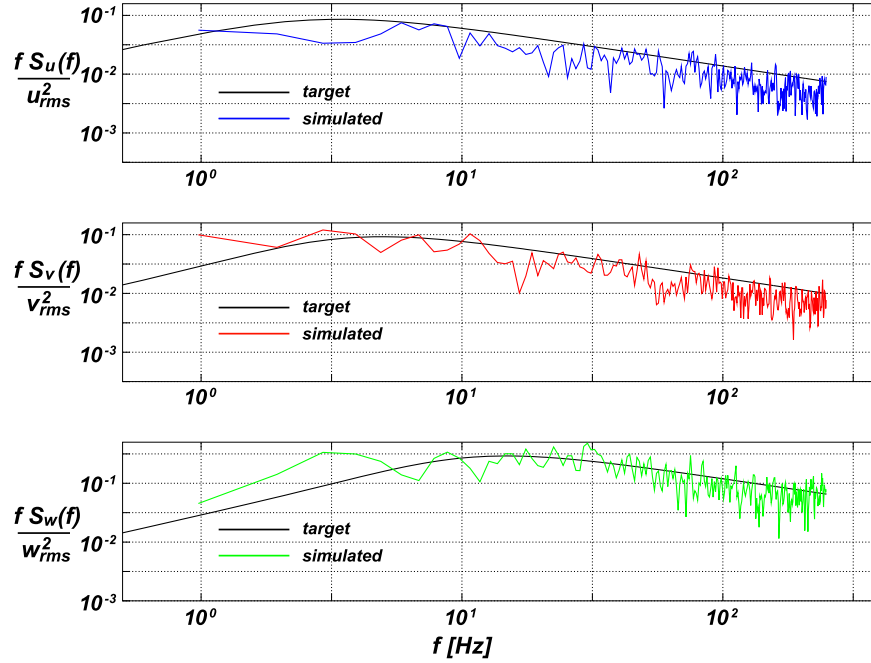
Figure 2.2: Spectra of the velocity series simulated by the MDSRFG vs target spectra.

As can be observed in figure (2.2), the spectra of the simulated series fit well with the target spectra in the three principal directions; indicating that the anisotropy of the spectra is well represented by the proposed method. The rms value of each simulated

29

fluctuating velocity component (obtained from a sample of 10 velocity simulations) is also compared to the corresponding target values. As shown in table (2.1), the rms values of the fluctuating velocities simulated by the MDSRFG approach are in better agreement with the target values than those obtained using the *scaling and orthogonal transformation* or the *aligning and remapping* techniques (Huang et al., 2010).

	σ_u	σ_v	σ_w
Scaling and transformation	0.9968	2.44	2.9956
Aligning and remapping	0.95	1.9987	3.08
MDSRFG approach	1.0527	2.1850	3.1123
target	1.12	2.24	3.36

Table 2.1: rms values (m/s) of the simulated velocities by different techniques.

When modeling the spatial correlation between same fluctuating velocity components in two different points i and j, a spatial correlation matrix needs to be computed. This target function is built for the u-component, for instance, from the spectra and coherence functions between nodes i and j as

$$\boldsymbol{S}_{\boldsymbol{c}i,j} = \sum_{m=1}^{M} \sqrt{Su^i(f_m)Su^j(f_m)}\ \gamma_u^y(f_m), \tag{2.52}$$

where

$$\gamma_u^y(f_m) = \exp\Big(\frac{-C_u^y|y_i - y_j|f_m}{U_{\mathrm{avg}}}\Big), \tag{2.53}$$

is the coherence function of the u fluctuating velocity component in the $y-$direction and C_u^y is the decay coefficient (usually taken in the range 10-12). In figures (2.3) to (2.5) the spatial correlation for the u, v and w-components of the velocity fluctuations obtained by the expression (2.45) is compared to the correlations computed using equation (2.52) for different values of L_s.
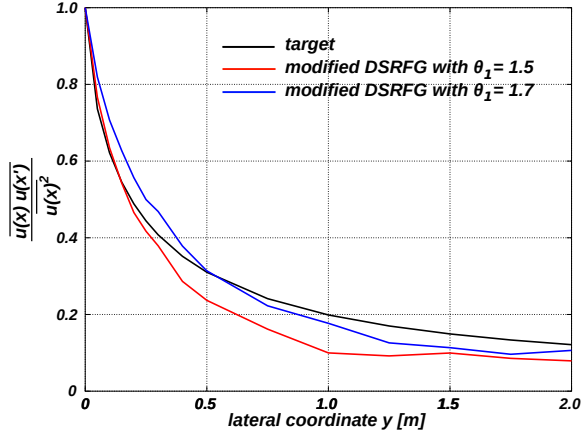
Figure 2.3: Non-dimensional spatial correlation of the u fluctuating velocity component.
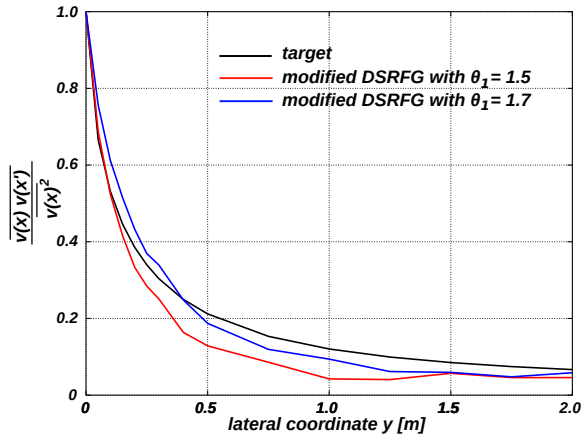
Figure 2.4: Non-dimensional spatial correlation of the v fluctuating velocity component.

Time correlation is also computed for each velocity component, e.g. for the u-component:

$$R(m \ \delta\tau) = \frac{1}{M - m} \sum_{j=0}^{M-m} u(j \ \delta\tau) \ u[(j + m) \ \delta\tau], \qquad (2.54)$$

here m is an integer such that $\tau_m = m \ \delta\tau$, with $0 \le m < M$, $\delta\tau$ is the time step size and M is the length of the vector τ_m. Samples of temporal correlations from the MDSRFG and the DSRFG methods are shown in figures (2.6) to (2.8) for each velocity

31
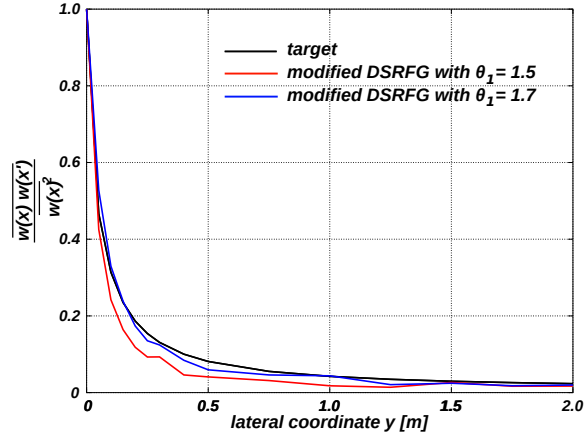
Figure 2.5: Non-dimensional spatial correlation of the w fluctuating velocity component.

component. Also, they are compared to the autocorrelation function of a random stationary process:

$$R_i(\tau) = e^{-|\tau|/T_i}, \tag{2.55}$$

with time scales T_i $(i = u, v, w)$ computed as

$$T_i = \int_0^\infty R_i(\tau)d\tau \equiv \sum_{j=0}^{M_0} R_i(j \ \delta\tau) \ \delta\tau, \tag{2.56}$$

where $M_0 < M$. Low frequency fluctuations cause oscillations on the time correlation around the zero value as the time lag tends to infinite. Consequently, if equation (2.56) is approximated without an adequate upper limit of the sum, it will fail to estimate the scale (Thacker et al., 2010). In this thesis the time scale is computed by setting M_0 to the first τ-axis crossing value, see figures (2.6) to (2.8).
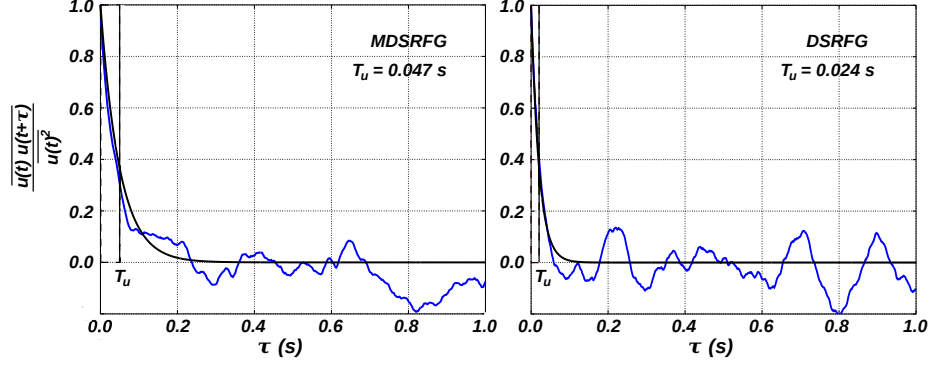
Figure 2.6: u velocity component non-dimensional time correlation. MDSRFG (*left*) and DSRFG method (*right*).
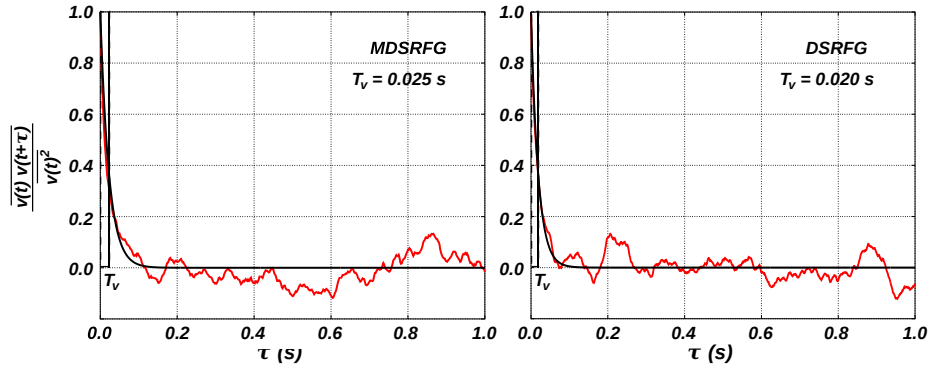
Figure 2.7: v velocity component non-dimensional time correlation. MDSRFG (*left*) and DSRFG method (*right*).
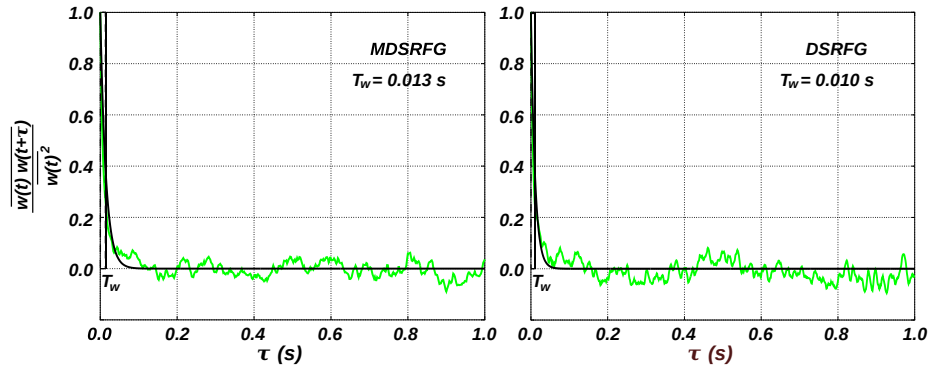
Figure 2.8: w velocity component non-dimensional time correlation. MDSRFG (*left*) and DSRFG method (*right*).

In order to analyze the influence of the time correlation parameter τ_0 on the time scales in the MDSRFG method, a parametric study is performed and the results are shown in figure (2.9) for each fluctuating velocity component. In the original test of Huang et al. (2010) no time scale value was provided, whereby in this work it is estimated from Taylor's hypothesis: $T_i = L_i/U_{\text{avg}}$ $(i = u, v, w)$. These values are compared with those obtained by the MDSRFG and DSRFG methods, see table (2.2).

	T_u	T_v	T_w
DSRFG approach	0.034 ± 0.028	0.022 ± 0.009	0.010 ± 0.002
MDSRFG approach	0.043 ± 0.021	0.023 ± 0.014	0.011 ± 0.002
target	0.043	0.021	0.007

Table 2.2: Time scale statistics comparison (s).
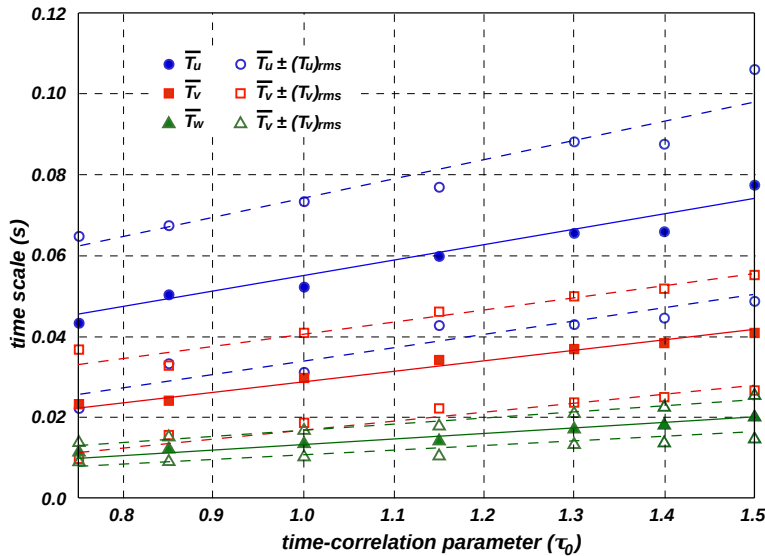
Figure 2.9: Time scale statistics of the fluctuating velocity components as a function of τ_0 obtained by the MDSRFG method.

The results in figure (2.9) and table (2.2) correspond to the mean and standard deviation values of the time scale over a sample of 70 velocity series. The sample size is chosen as statistically representative of the velocity record. It is important to highlight here the possibility to slightly modify the time scale with different τ_0 values in the MDSRFG method whereas the DSRFG method is limitated to the three values shown in table (2.2) for this particular case. Note that although the target time scales, estimated by the Taylor's hypothesis, are in accordance with those obtained by the

DSRFG method, the application of the MDSRFG approach leads to a wider range of possible values by changing τ_0, see figure (2.9).

The anisotropic turbulence conditions at the inlet plane can be obtained by performing a previous RANS simulation or by experimental measurements. The two input parameters, L_s and τ_0, must be selected in order to reproduce the statistical properties of the flow under consideration. In this sense, the parameter θ_1 in equation (2.46) varies between 1 and 2 (Huang et al., 2010) and τ_0 between 0.75 and 1.5, this later range of values being derived from the parametric analysis shown in figure (2.9). Within this range one can select the time scale values that better aproximate the target ones without compromising other physical features (i.e., without loosing the adjustment of the velocity spectra, spatial correlation and rms values of the turbulent flow being simulated).

To validate the relationship proposed by equation (2.39) the influence of the frequency interval size Δf over the rms values of the time series is analyzed. What it is expected is that the synthetic turbulence generation provides the correct rms values as $\Delta f \to 0$, that is, as the discretization of the spectrum becomes finer the energy content in each frequency should be included in the time series generation. Table (2.3) shows the results of this analysis, where it can be seen that the method proposed in this work seems to converge to the target values as Δf becomes smaller while in the case of the DSRFG method the values do not converge at all.

Δf	σ_u		σ_v		σ_w	
	DSRFG	MDSRFG	DSRFG	MDSRFG	DSRFG	MDSRFG
10	0.49	0.76	1.27	1.84	2.05	2.95
5	0.83	0.87	1.93	2.07	2.94	3.01
2	1.47	0.98	3.15	2.11	4.69	3.03
1	2.17	1.04	4.47	2.11	6.75	3.11
target	1.12		2.24		3.36	

Table 2.3: Comparison of the standard deviation values of the synthesized velocity components by the two methodologies.

As it is clearly depicted by equation (2.38), the computational cost is identical to that of the DSRFG method. Thus, for each node at the inlet section the cost at each time step is $O(MN)$; where M is the number of points in which the target spectrum is discretized and N the number of samples for each wave number k_m. Furthermore, the

computation of the fluctuating velocity components in equation (2.38) is independent of the LES process, i.e., the turbulence synthesis for some number of time steps (or the entire simulation process) can be done prior to the LES computations.

As a final observation, it must be noted that the proposed approach, as any synthesized turbulence generation method, must be used as a turbulence initializer, i.e., a perturbation generator that "triggers" the transition to a fully developed turbulence state by LES (Davidson, 2007). In this regard, it must be said that independently of the selected L_s value, the resolved scales are in concordance with the mesh (filter) size which is inherent to the LES conception.

2.5 Application of the modified DSRFG method in LES

It is well known that the generation of developed turbulence by LES at high Reynolds number flows is computationally expensive and time consuming. In order to avoid this drawbacks, the MDSRFG method can be used to setting up the turbulent inflow conditions in LES computations. In the following sections, two examples of application of the MDSRFG method are shown. For the sake of simplicity in the comparison between the DSRFG and MDSRFG approaches, both parameters θ_1 and τ_0 are set to 1.

2.5.1 Flow through a conical diffuser

This test case consists of a swirling boundary layer developing in a conical diffuser and was experimentally studied by Clausen et al. (1993). The conical diffuser is placed 100 mm downstream of a rotating swirl generator of diameter $D = 260$ mm and discharges into the atmosphere at $x = 510$ mm, see figure (2.10).

The device in charge of the swirl generation is a honeycomb positioned 500 mm before the beginning of the expansion which rotates with a part of the pipe of 400 mm long after it, while all other parts are locked. In the diffuser expansion, the boundary layer separation is prevented by the swirl which is strong enough to avoid recirculation in the core flow. The Reynolds number of the experimental test was $2.08 \cdot 10^6$ based
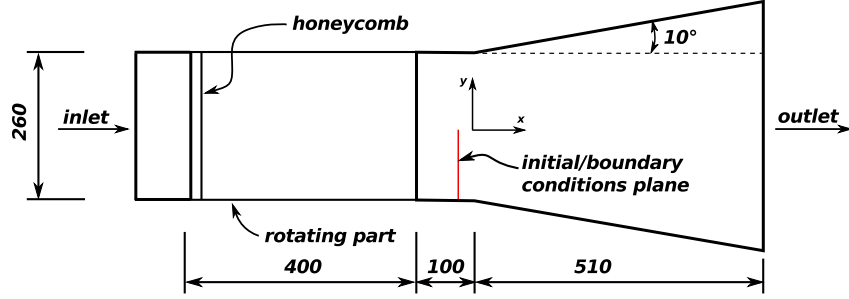
Figure 2.10: Diffuser test case. All dimensions are in mm.

on the diameter of the inlet section D, the mean axial velocity $U_x = 11.6$ m/s and the kinematic viscosity $\nu = 1.45 \cdot 10^{-6}$ m^2/s.

The computational domain adopted is shown in figure (2.11). A large dump is added in order to avoid recirculations in the diffuser outflow region. A structured mesh has been used for the computational simulation of the swirling flow which consists of $743,925$ hexahedral elements and $760,568$ nodes.
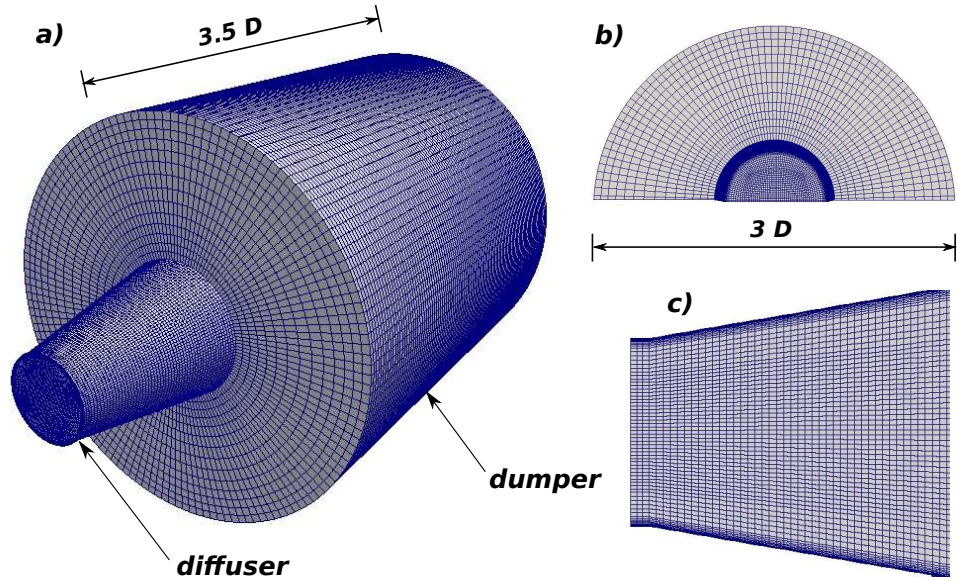
Figure 2.11: Diffuser test case. All dimensions are in mm.

Synthesized turbulence is imposed in all nodes at plane $x = -25$ mm considering the von Kármán spectra, equations (2.47-2.49) and figure (2.12). At the dumper outlet boundary we impose $p = p_{\text{ref}}$, being $p_{\text{ref}} = 101,325$ Pa the reference pressure. In figure (2.13) the comparison between the computational simulation for both, DSRFG

and MDSRFG methods, and the ERCOFTAC measurement data (http://cfd.mace.manchester.ac.uk/ercoftac/) is shown. Clearly, the mean velocity (streamwise and orthoradial) and the kinetic energy boundary conditions for the MDSRFG method match the experimental data at the inlet. A frequency step $\Delta f = 10 \text{ s}^{-1}$ is enough for the MDSRFG method to provide a suitable turbulent kinetic energy while this is not the case for the DSRFG approach, as it can be seen in figure (2.13).
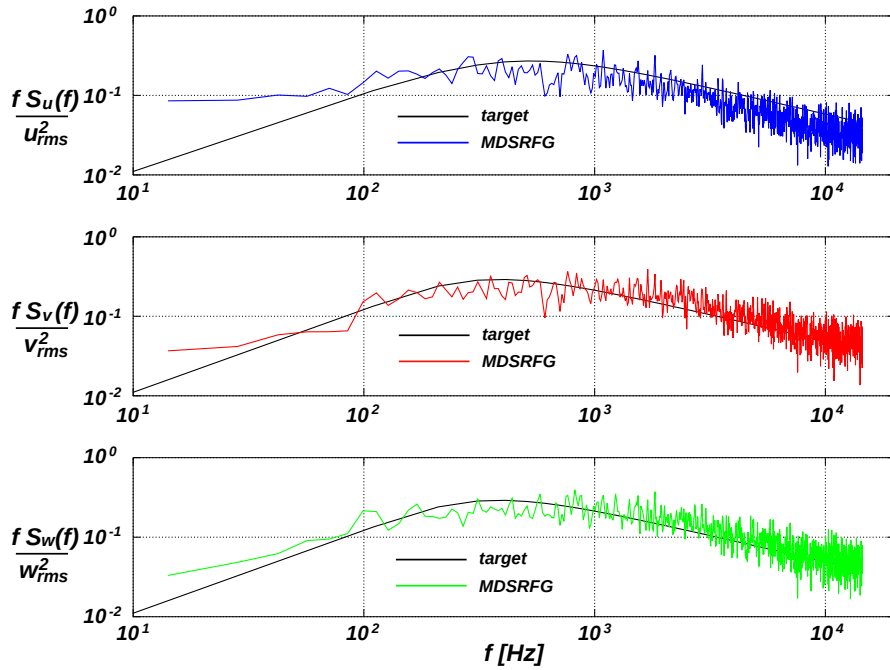
Figure 2.12: Comparison of the spectra simulated by the MDSRFG with the target spectra.

Vortex structures. Pictures of unsteady vortex structures were obtained from computational simulations by means of isosurfaces of the second invariant of the velocity gradient tensor. This is the so called Q-criterion, which can be written for an incompressible flow as (Hunt et al., 1988):

$$Q = \frac{1}{2}(\Omega_{ij}\Omega_{ij} - S_{ij}S_{ij}), \tag{2.57}$$

where S_{ij} is the rate-of-strain tensor and Ω_{ij} is the rate-of-rotation tensor which being
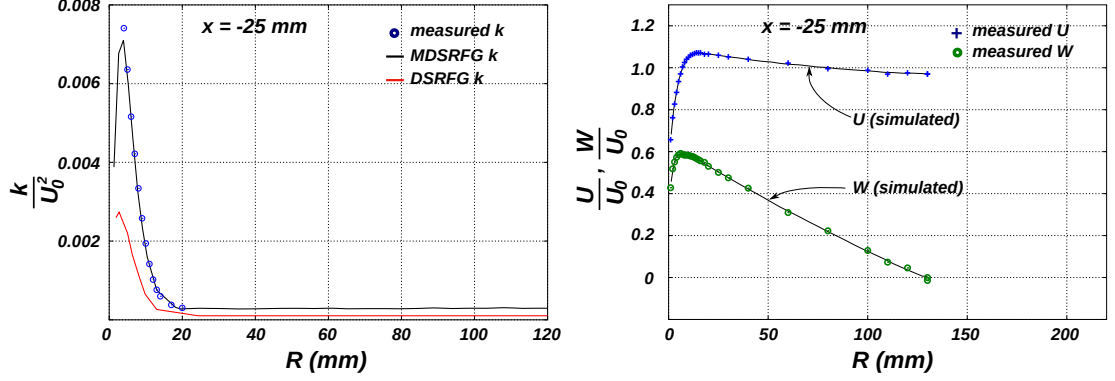
Figure 2.13: Turbulent kinetic energy (*left*), mean streamwise and orthoradial velocity profile (*right*) obtained by the computational simulation and experimental data Clausen et al. (1993).

the symmetric and antisymmetric parts of the velocity gradient tensor $A_{ij} = \partial u_i / \partial x_j$ respectively, i.e.,

$$S_{ij} = (A_{ij} + A_{ji})/2 \qquad \text{and} \qquad \Omega_{ij} = (A_{ij} - A_{ji})/2. \tag{2.58}$$

The physical interpretation of equation (A.14) is that the second invariant Q is a balance between the strain rate S_{ij} and the rotation rate Ω_{ij} which implies that positive Q isosurfaces exhibits zones where the amount of rotation exceeds the strain. Furthermore, Q can be expressed in a different form:

$$
\begin{aligned}
Q &= \frac{1}{4}\big[\sigma^2 - 2(S_{ij}S_{ij})\big] \\
&= -\frac{1}{2}\frac{\partial u_i}{\partial x_j}\frac{\partial u_j}{\partial x_i} = -\frac{1}{2\rho}\boldsymbol{\nabla}^2 p
\end{aligned}
\tag{2.59}
$$

where the connection between Q and the vorticity modulus (or enstrophy $\sigma^2 = \sigma_1^2 + \sigma_2^2 + \sigma_3^2$) arises. Here, $\sigma_i, i = 1, 2, 3$ are the vorticity components in the three spatial directions and $\boldsymbol{\nabla}^2 p$ is the Laplacian of the pressure. From this equation it is possible to prove that the Q-criterion ($Q > 0$) is a necessary condition for the existence of thin, convex low pressure-tubes (Dubief and Delcayre, 2000), e.g. see the Appendix A of this thesis for a detailed discussion about this subject. Vortex structures identified with $Q = 4000$ s^{-2} are shown in figure (2.14). It can be noted that the instantaneous characteristic vortex structures of this model are well captured.
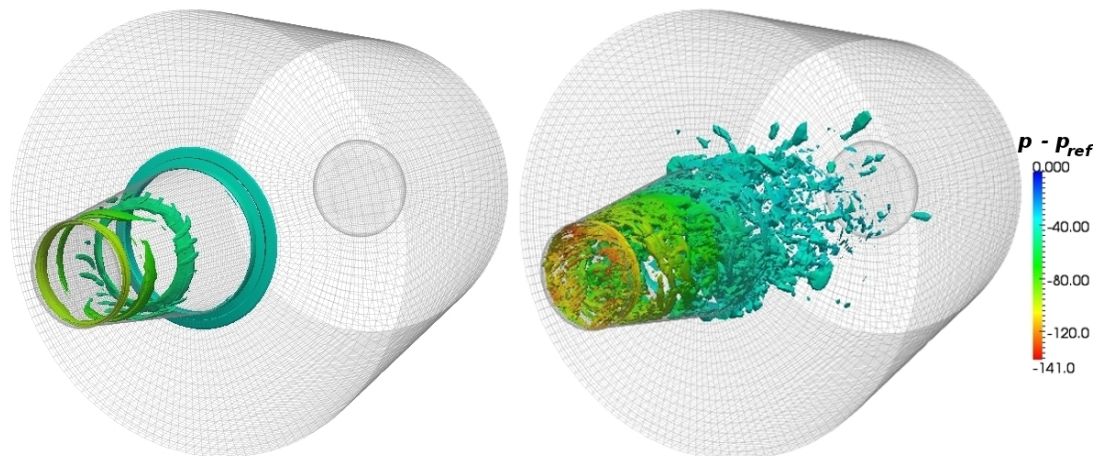
Figure 2.14: Vortex flow structures ($Q = 4000 \text{ s}^{-2}$) colored by pressure (N/m^2). Computational simulation with no synthesis (*left*) and with the MDSRFG method (*right*).

2.5.2 Ahmed body

The second test is a computational simulation of the flow around the Ahmed's body. In this Chapter, the generation of transient inlet flow conditions is described and its consequences on the model (transient behaviour of forces and pressures) are discussed. A more detailed explanation about this computational simulation along with a fluid-structure interaction study are provided in Chapter (3).

The Ahmed body is a conceptual model of a generic car, proposed in the experimental work of Ahmed et al. (1984). Though this model is composed of three simple geometry parts: a fore body, a mid section and a rear end; the flow around it still retains some characteristics of the flow around real road vehicles. Figure (2.15) shows the geometry of the model for a slant angle of 35°. All units are in millimeters.
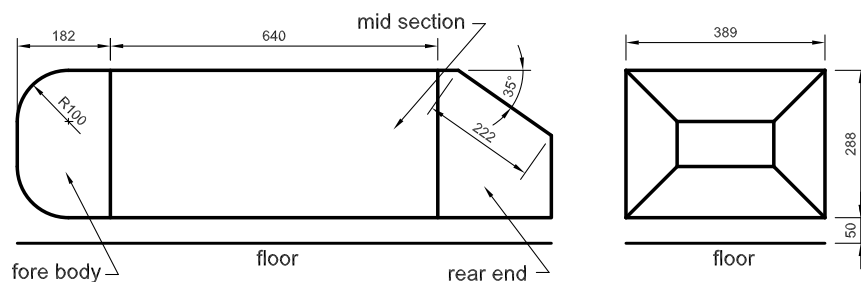
Figure 2.15: Ahmed model.

z [cm]	u_1^+	I_u	σ_u
2.5	0.74	0.096	1.677
7.0	0.83	0.070	1.372
17.0	0.92	0.045	0.978
22.5	0.95	0.027	0.606
30.0	0.98	0.011	0.255
40.0	0.982	0.008	0.186
48.0	0.985	0.007	0.163
57.5	0.986	0.0065	0.151
62.5	0.987	0.007	0.163
70.0	0.988	0.008	0.187
75.0	0.988	0.009	0.210
88.0	0.990	0.010	0.234
102.5	0.995	0.011	0.258
119.0	1.000	0.012	0.283

Table 2.4: Parameters for the inflow boundary condition at the wind tunnel test section (Wittwer and Möller, 2000).

Wind velocity and turbulence statistical parameters of the incident flow at the test section are shown in table (2.4). Other parameters, like turbulence intensities $I_v = 0.02$, $I_w = 0.03$ and integral length scales $L_u = 0.3$, $L_v = 0.1$ and $L_w = 0.05$ were also adopted. The Reynolds number for the experimental test is roughly $1.70 \cdot 10^6$ based on the length of the vehicle model $L = 1.044$ m, the mean velocity magnitude 23.6 m/s, the kinematic viscosity $\nu = 1.45 \cdot 10^{-6}$ m^2/s and a constant density $\rho = 1.225$ kg/m^3. In order to adress the accuracy of the DSRFG and MDSRFG methods, a small frequency interval, $\Delta f = 0.5$ s^{-1}, was used in both approaches.

The computational domain is a rectangular box with a cross section of 2.40 m width (x-direction) and a height of 1.80 m (z-direction) representing a wind tunnel section, see figure (2.16). The body was located at $2L$ downstream (y-direction) the inlet section and at $3L$ upstream the outlet boundary to allow full development of the flow downstream to the model, totaling an extension of $6L$. No-slip boundary condition is prescribed at ground, roof and tunnel walls, while null pressure is imposed at the outlet wall. With these conditions the blockage ratio is about of 2.6%.

The grid was refined close to the body surface in order to account for viscous effects at the walls and to adequately capture the changes in flow variables within the boundary layer region. Five rows of wedge type elements, shown in detail in figure (2.16), were generated from the surface of the vehicle model. The first wedge-layer has a thickness
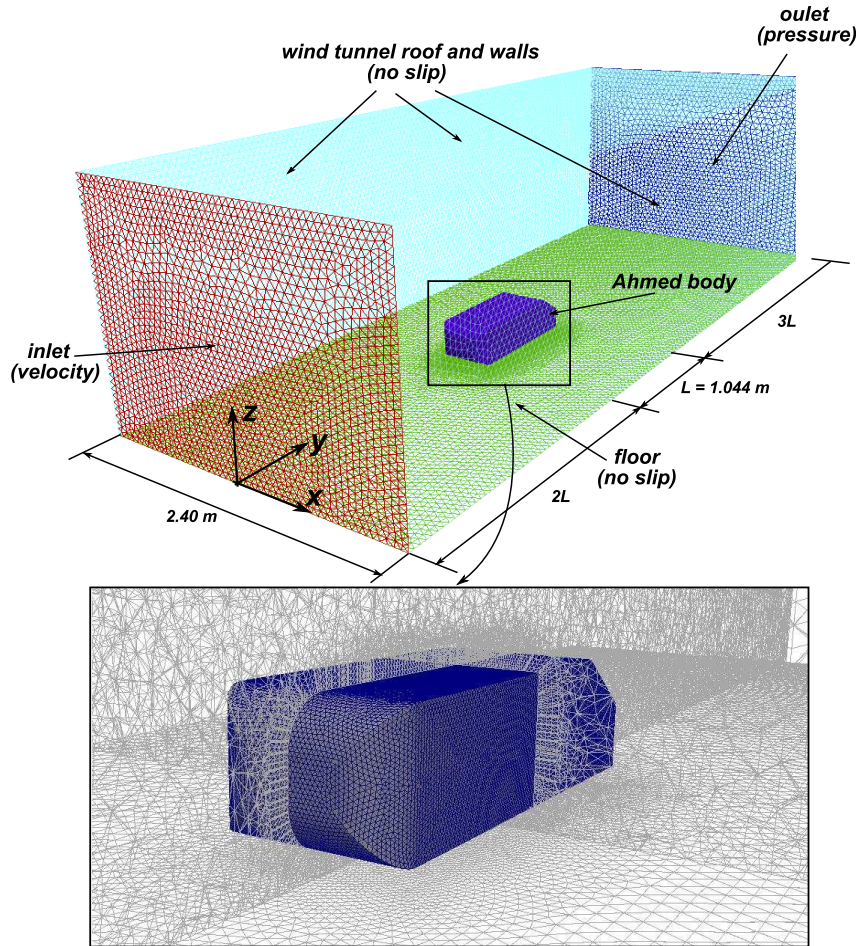
Figure 2.16: Computational domain and detail of the mesh.

$h_m = 4.79 \cdot 10^{-3}$ $L = 5$ mm. A classical logarithmic law for velocity was imposed at the body surface (see e.g. the work of Rodi (1997)).

Figure (2.17) shows, in the right side, the time history of the simulated fluctuating velocity components by the MDSRFG method in a central point of the inlet section and the instantaneous fluctuation contours on the left side. The velocities maintain the spatial anisotropy among the three directions, as can be observed from the statistical values. Furthermore, the rms values of the simulated velocity series are compared in table (2.5). Clearly, for the small value of Δf considered, the MDSRFG values almost perfectly agrees with those of the target while in the case of the DSRFG method the rms values exceeds the target ones.
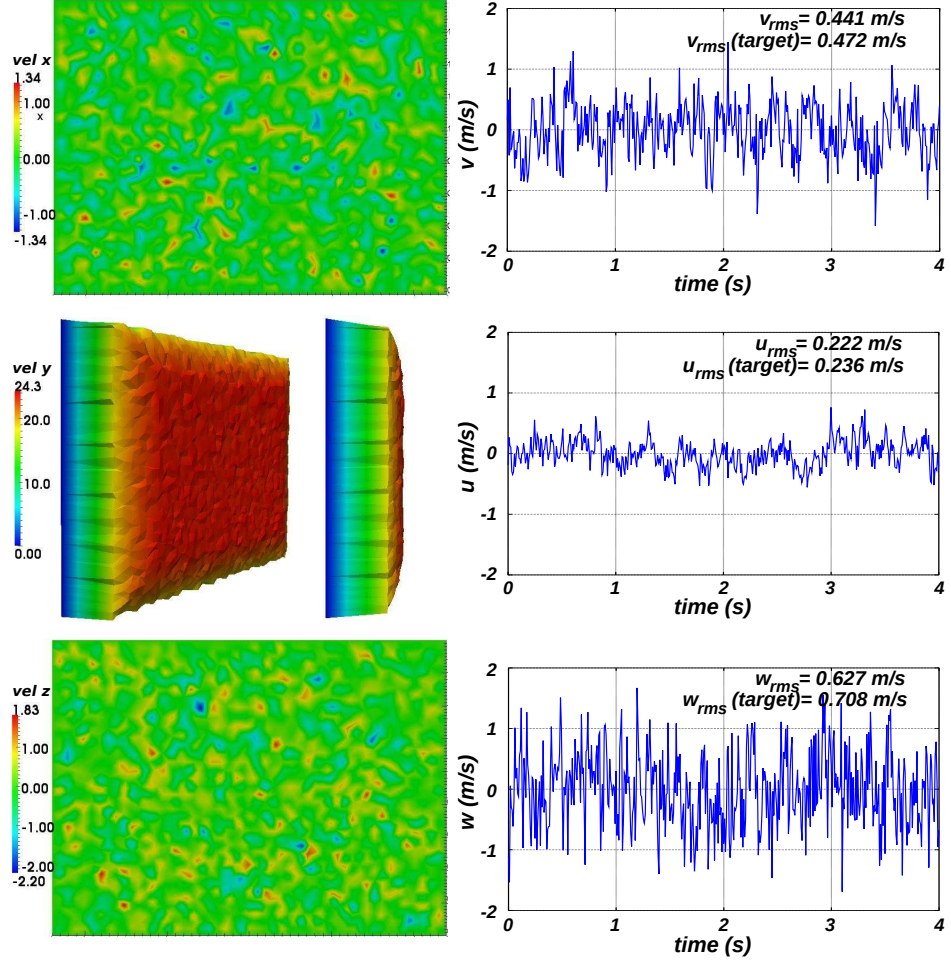
Figure 2.17: Inlet fluctuating velocities simulated by the MDSRFG method.

	σ_u	σ_v	σ_w
DSRFG	0.4432	0.9043	1.2228
MDSRFG	0.2219	0.4411	0.6272
target	0.236	0.472	0.708

Table 2.5: rms values (m/s) of the velocity series simulated with $\Delta f = 0.5$ s^{-1}.

2.5.2.1   Forces acting on the body

To characterize the transient behavior of the forces acting on the model, an analysis in the frequency domain is performed. In figure (2.18) the spectra of the forces in the z, x and y directions are shown. It can be seen that for the x and y-directions the energy content of the fluctuating forces obtained with the application of the DSRFG and

MDSRFG methods are in agreement. The lift-force spectrum shows different results for reduced frequency values higher than unity.
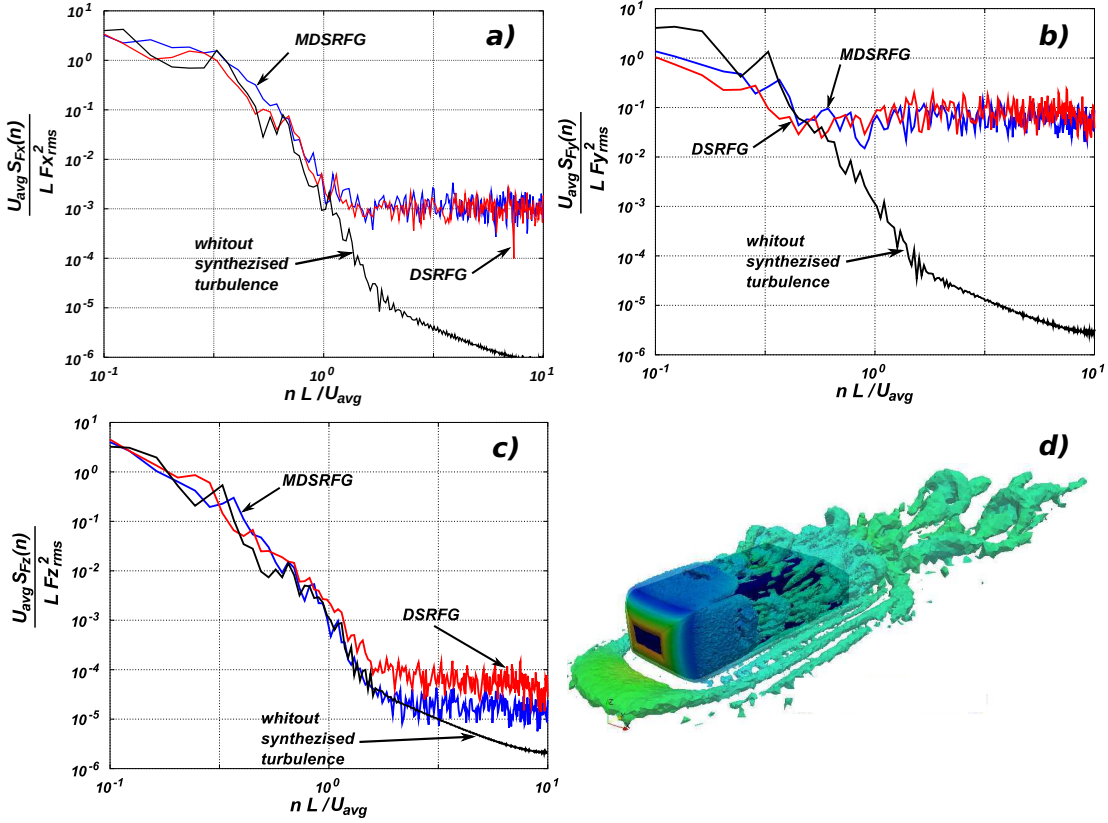
Figure 2.18: Computational simulation with inlet synthesized turbulence (MDSRFG and DSRFG) and without inlet synthesized turbulence. *a)* Side force spectrum (x-component force). *b)* Drag force spectrum (y-component force). *c)* Lift force spectrum (z-component force). *d)* $Q = 800$ s^{-2} isosurface colored by pressure.

Also in figure (2.18) instantaneous vortex structures identified with $Q = 800$ s^{-2} are shown. It can be noted that these structures are in correlation with those reported by Uruba (2010).

2.5.2.2 Unsteady velocity

The velocity unsteadiness produced by the application of the DSRFG method is relatively higher than the one obtained with the MDSRFG method as a consequence of the higher kinetic energy provided by the former approach. This is observed in the wake

along the plane of symmetry, figure (2.19), and in the rms values of pressure coefficient on the model back-light, see figure (2.20).
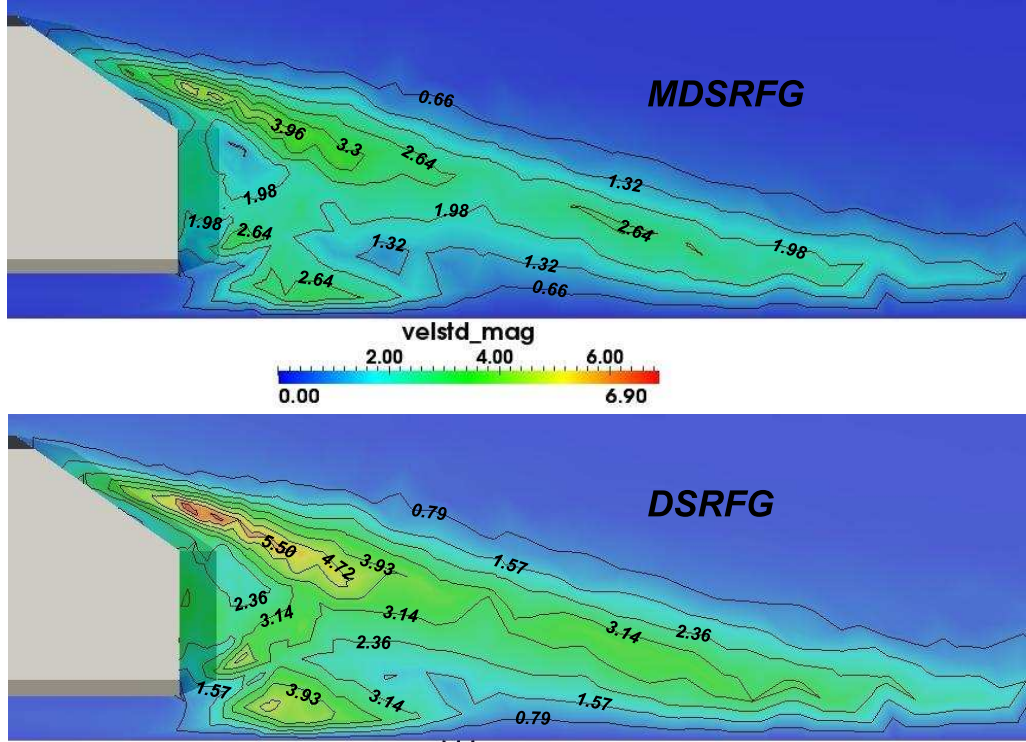
Figure 2.19: Standard deviation velocity magnitude. **top**: MDSRFG,   **bottom**: MD-SRFG.

The pressure coefficient unsteadiness is computed as

$$\sigma_{C_p} = \frac{\sigma_p}{\frac{1}{2} \ \rho \ U_{\text{avg}}^2} \tag{2.60}$$

and although different levels of unsteadiness induced by both synthesized turbulence methods are evident, the distribution of the pressure coefficient unsteadiness on the back-light of the model presents in both cases high similarities, such as the wide region of low fluctuating values in most parts of the vertical base and in the central region of the slant.

Regions of high unsteadiness values on the sides of the back-light surface (near the edge of intersection of the slant and vertical base) were detected in both cases. These
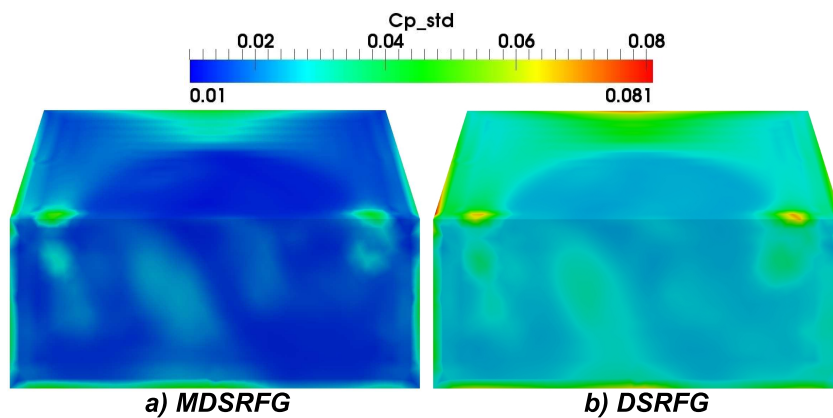
Figure 2.20: Standard deviation of the pressure coefficient on the model back-light.
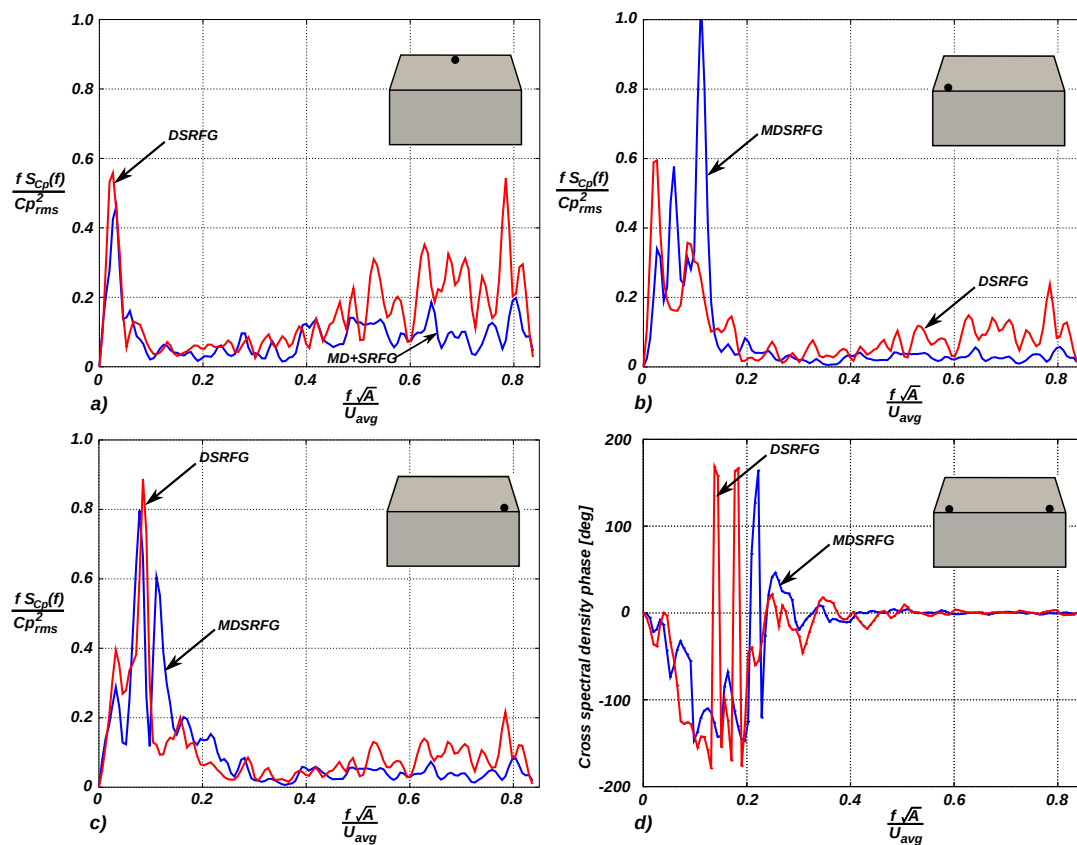
Figure 2.21: a, b, c) Spectral density of pressure coefficients in different points on the slant plane. d) Cross spectral density phase between two points on the back-light of the model.

spots are consistent with the observed vortex generating regions in figure (2.18.d).

Another region of high unsteadiness activity was found near the top edge of the back-light slant surface in coincidence with the flow separation zone.

Furthermore, a frequency domain study of the pressure behavior was performed. Figure (2.21) shows the non-dimensional auto-spectral density measured in points located on the regions previously highlighted, by the simulations with the DSRFG and MDSRFG methods. In can be seen that in the spots analyzed, higher energies are detected in the range of high Strouhal numbers in the simulation with DSRFG. For the low Strouhal numbers the energies are quite similar (except for the case in figure (2.21b) where the energy content in the simulation with MDSRFG is higher) denoting that both methods maintain the mean characteristics unaffected. Also, this low-Strouhal number region ($f\sqrt{A}/U_{\mathrm{avg}} < 0.2$, based on the square root of model frontal area) possesses the higher energy content which can be associated with the presence of shedding phenomena.

In figure (2.21) the phase correlation between the points in the regions of vortices production is shown. It can be seen that the phase estimate for Strouhal numbers lower than 0.2 presents a phase shift of about $100°$ and more, indicating a nearly alternate shedding.

2.6   Conclusions

In this Chapter, a general method for the generation of inflow synthesized turbulence has been introduced and evaluated. The method is based on a previous turbulence generator known as the discretizing and synthesizing random flow generation (DSRFG) method (Huang et al., 2010). The proposed approach preserves the main characteristics and advantages of the DSRFG method: it is highly parallelizable, different spectral models can be used and it can represent either isotropic and anisotropic turbulence. In addition, the key point of the modified DSRFG (MDSRFG) method is that it preserves the statistical quantities that could be prescribed at the inlet of the domain as the number of samples M (number of points in the spectrum) increases, through the computation of the factors $p_i^{m,n}$ and $q_i^{m,n}$ by equations (2.42) and (2.43). This characteristic ensures that the imposed turbulence intensity on the fluctuating velocity series represents adequately the kinetic energy of the turbulent flow under study.

2. SYNTHESIZED TURBULENCE FLOW

Following previous methodologies (Smirnov et al., 2001; Batten et al., 2004), a dimensionless time scale parameter, τ_0, has been included in the formulation of the proposed approach in order to "control" the time correlation of the generated velocity series. In this way, the MDSRFG method can modify the time scale by varying τ_0 as it has been demonstrated in Section §2.4.

Some numerical tests show that the proposed approach is very well-suited for three-dimensional computations using the LES approach. For the swirling turbulent flow inside a diffuser the inlet conditions obtained matches almost exactly the experimental measurements. Regarding to the simulation of the flow over the Ahmed body, it has been shown that results obtained, i.e., forces, level of unsteadiness in the wake and the back-light of the model, are very sensitive to the upstream inflow conditions and therefore this issue must be correctly addressed by any synthesized turbulence method.

Chapter 3

Fluid-structure interaction

Multidisciplinary and multiphysics coupled problems represent nowadays a paradigm when studying/analyzing even more complex phenomena that appear in nature and in new technologies. There exists a great number of problems where different physical processes (or models) converge, interacting in a strong or weak manner (e.g., acoustics/noise disturbances in flexible structures, magneto-hydrodynamics devices, microelectro-mechanical devices, thermo-mechanical problems like continuous casting process, fluid-structure interaction like wing flutter problem or flow-induced pipe vibrations).

The numerical simulation of these kind of problems often requires to deal with strong distortions of the continuum under consideration and at the same time allowing for a clear definition of free surfaces and fluid-fluid, solid-solid, or fluid-structure interfaces (Donea et al., 2004). An essential subject in these problems is the choice of a suitable kinematical description of the continuum given that this description determines the relationship between the deforming continuum and the mesh of finite elements. Two classical descriptions of motion are typically used in continuum mechanics analyses: the Lagrangian description and the Eulerian description. The technique known as the arbitrary Lagrangian-Eulerian (ALE) description attempts to combine the advantages of the above descriptions while minimizing their respective drawbacks. In the ALE based finite elements formulation the mesh is chosen as a reference domain in order to describe the kinematics of the continuum. The pure Lagrangian and pure Eulerian formulation are particular cases of the ALE approach.

For simple structural problems (like hinged rigid rods with one or two vibrational d.o.f.'s) it is possible to combine into a single (simple) formulation the fluid and the structural governing equations (Dowell et al., 1995). In those cases, a fully explicit or fully implicit treatment of the coupled fluid/structure equations is attainable. Nevertheless, for complex/large scale structural problems, the simultaneous solution of the fluid and structure equations using a 'monolithic' scheme may be mathematically unmanageable or its implementation can be a laborious task. Furthermore, the monolithic coupled formulation would change significantly if different fluid and/or structure models were considered.

An efficient alternative is to solve each sub-problem in a partitioned procedure where time and space discretization methods could be different. Such a scheme simplifies explicit/implicit integration and it is in favor of the use of different codes specialized on each sub-area. There exist several procedures for coupling fluid and structure solvers: the coupling conditions and the moving interface can treated in a fully explicit or implicit or in a mixed explicit/implicit manner. This approach allows a smooth transition between "loose" and "strong" coupling, while a large system of nonlinear equations has to be solved by using (iterative) solvers for the subsystems. Usually, this is done with Block-Jacobi, Block-Gauss-Seidel or related relaxation methods. A detailed description of the 'state of the art' in the computational fluid/structure interaction area can be found in the works of Piperno and Farhat (2001); Felippa et al. (2001); Park and Felippa (2000); Dettmer and Peric (2006) and the references therein.

In this thesis, a partitioned algorithm implemented in the PETSc-FEM code is used. A brief description of this algorithm is made in this chapter along with the definition of the Arbitrary Lagragian-Eulerian formulation.

3.1 ALE formulation for moving meshes

The ALE approach provides a method for the solution of the equations describing fluid flow through a moving mesh. As was stated before, it is a hybrid description, between Lagrangian and Eulerian schemes. In the Lagrangian scheme each individual node of the computational mesh follows the associated material particle during motion. That is, the computational grid follows the continuum in its motion, being the grid nodes

permanently linked to the same material points. An application $\boldsymbol{\varphi}$ is defined to relate the material coordinates, $\mathbf{X}$, to the spatial coordinates, $\boldsymbol{x}$:

$$\boldsymbol{\varphi} : (\mathbf{X}, t) \rightarrow \boldsymbol{\varphi}(\mathbf{X}, t) = (\boldsymbol{x}, t) \tag{3.1}$$

which simply links $\mathbf{X}$ and $\boldsymbol{x}$ in time by the law of motion, namely

$$\boldsymbol{x} = \boldsymbol{x}(\mathbf{X}, t) \tag{3.2}$$

As can be seen, the spatial coordinates $\boldsymbol{x}$ depend on the material particle $\mathbf{X}$ and the time t, while the physical time is measured by the same variable t in the material and spatial domains. This means that for every fixed instant t, the application $\boldsymbol{\varphi}$ defines a configuration in the spatial domain. Its gradient has the form

$$\frac{\partial \boldsymbol{\varphi}}{\partial (\mathbf{X}, t)} = \begin{pmatrix} \frac{\partial \boldsymbol{x}}{\partial \mathbf{X}} & \boldsymbol{u} \\ \mathbf{0}^T & 1 \end{pmatrix} \tag{3.3}$$

where $\mathbf{0}^T$ is a null row vector and $\boldsymbol{u}$ the material velocity:

$$\boldsymbol{u}(\mathbf{X}, t) = \left. \frac{\partial \boldsymbol{x}}{\partial t} \right|_{\mathbf{X}} \tag{3.4}$$

with $\Big|_{\mathbf{X}}$ meaning "holding $\mathbf{X}$ fixed". Clearly, the Jacobian of the transformation, J, must verify

$$J = \det(\partial \boldsymbol{x} / \partial \mathbf{X}) > 0 \tag{3.5}$$

in order to impose a one-to-one correspondence and to avoid change of orientation in the reference axes, at each point $\mathbf{X}$ and instant $t > t_0$. This description allows an easy tracking of free surfaces and interfaces between different materials and are mainly used in structural dynamics. Nevertheless, it can not follow large distortions of the computational domain without intensive remeshing operations.

3. FLUID-STRUCTURE INTERACTION

On the other hand, in the Eulerian scheme the computational mesh is fixed and the fluid moves with respect to the grid, enabling the simulation of large displacements owing to the fluid motion. The physical quantities associated with the fluid particles are evaluated while they are passing through a fixed region of space at every instant of time. The material velocity $\boldsymbol{u}$ at a given mesh node is the velocity of the material point coincident with this particular node at the corresponding time t. In consequence, $\boldsymbol{u}$ is expressed with respect to the fixed mesh without any reference to the initial configuration of the continuum and the material coordinates $\mathbf{X}$:

$$\boldsymbol{u} = \boldsymbol{u}(\boldsymbol{x}, t). \tag{3.6}$$

This formulation is essential for the simulation of turbulent flows but is unable to deal easily with the tracking of free surfaces and interfaces between different materials or different media (e.g., fluid-fluid and fluid-solid interfaces). The ALE approach has been developed in order to avoid the different shortcomings of the above descriptions. In this scheme, the nodes of the computational mesh can move with a velocity independent of the velocity of the material particles. Because of this freedom in moving the nodes of the mesh, the ALE description can handle greater distortions of the continuum than would be possible by a Lagrangian description and with more resolution than that provided by an Eulerian scheme. This is done by the introduction of the referential coordinates $\boldsymbol{\chi}$ to identify the grid points. In figure (3.1) the material ($R_{\mathbf{X}}$), the spatial ($R_{\boldsymbol{x}}$) and the referential ($R_{\boldsymbol{\chi}}$) domains are shown jointly with the one-to-one transformations relating the configurations (Donea and Huerta, 2003). The referential domain $R_{\boldsymbol{\chi}}$ is mapped into the material and spatial domains by $\boldsymbol{\Psi}$ and $\boldsymbol{\Phi}$, respectively.

The function $\boldsymbol{\Phi}$ maps the referential domain into the spatial domain:

$$\boldsymbol{\Phi} : (\boldsymbol{\chi}, t) \rightarrow \boldsymbol{\Phi}(\boldsymbol{\chi}, t) = (\boldsymbol{x}, t) \tag{3.7}$$

being its gradient:

$$\frac{\partial \boldsymbol{\Phi}}{\partial(\boldsymbol{\chi}, t)} = \begin{pmatrix} \frac{\partial \boldsymbol{x}}{\partial \boldsymbol{\chi}} & \hat{\boldsymbol{u}} \\ \boldsymbol{0}^T & 1 \end{pmatrix} \tag{3.8}$$
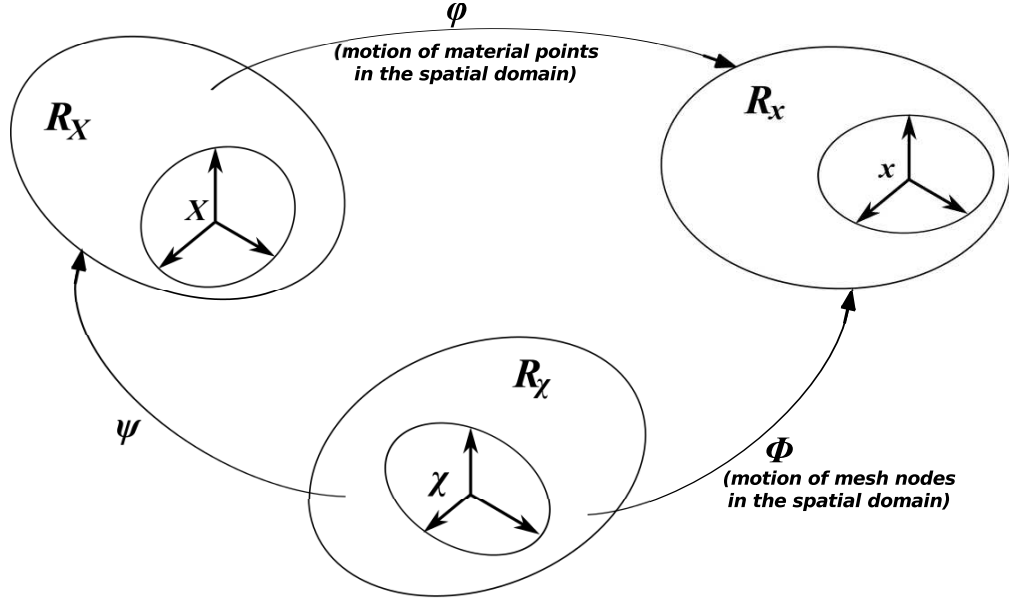
Figure 3.1: The three different domains and one-to-one mappings (Donea and Huerta, 2003).

where $\hat{\boldsymbol{u}}$ is the mesh velocity,

$$\hat{\boldsymbol{u}} = \frac{\partial \boldsymbol{x}}{\partial t}\bigg|_{\boldsymbol{\chi}}. \tag{3.9}$$

Regarding $\boldsymbol{\Psi}$, as the particle motion may be expressed as $\boldsymbol{\varphi}(\mathbf{X}, t) = \boldsymbol{\Phi}\big[\boldsymbol{\Psi}^{-1}(\mathbf{X}, t), t\big]$, it is more straightforward to represent directly its inverse $\boldsymbol{\Psi}^{-1}$,

$$\boldsymbol{\Psi}^{-1} : (\mathbf{X}, t) \rightarrow \boldsymbol{\Psi}^{-1}(\mathbf{X}, t) = (\boldsymbol{\chi}, t) \tag{3.10}$$

and its gradient takes the form:

$$\frac{\partial \boldsymbol{\Psi}^{-1}}{\partial (\mathbf{X}, t)} = \begin{pmatrix} \frac{\partial \boldsymbol{\chi}}{\partial \mathbf{X}} & \boldsymbol{w} \\ \mathbf{0}^T & 1 \end{pmatrix} \tag{3.11}$$

where $\boldsymbol{w}$ is a velocity defined as

$$w = \frac{\partial \chi}{\partial t}\bigg|_{\mathbf{X}} \tag{3.12}$$

and represents the particle velocity in the referential domain, since it measures the time variation of the referential coordinate χ holding the material particle $\mathbf{X}$ fixed. The velocities $\boldsymbol{u}$, $\hat{\boldsymbol{u}}$ and $\boldsymbol{w}$ are related in the following manner:

$$\frac{\partial \boldsymbol{\varphi}}{\partial(\mathbf{X}, t)}(\mathbf{X}, t) = \frac{\partial \boldsymbol{\Phi}}{\partial(\boldsymbol{\chi}, t)}\left(\boldsymbol{\Psi}^{-1}(\mathbf{X}, t)\right) \frac{\partial \boldsymbol{\Psi}^{-1}}{\partial(\mathbf{X}, t)}(\mathbf{X}, t)$$
$$= \frac{\partial \boldsymbol{\Phi}}{\partial(\boldsymbol{\chi}, t)}(\boldsymbol{\chi}, t) \frac{\partial \boldsymbol{\Psi}^{-1}}{\partial(\mathbf{X}, t)}(\mathbf{X}, t)$$

or, by replacing each corresponding term with the equations (3.3), (3.8) and (3.11),

$$\begin{pmatrix} \frac{\partial \boldsymbol{x}}{\partial \mathbf{X}} & \boldsymbol{u} \\ \mathbf{0}^T & 1 \end{pmatrix} = \begin{pmatrix} \frac{\partial \boldsymbol{x}}{\partial \boldsymbol{\chi}} & \hat{\boldsymbol{u}} \\ \mathbf{0}^T & 1 \end{pmatrix} \begin{pmatrix} \frac{\partial \boldsymbol{\chi}}{\partial \mathbf{X}} & \boldsymbol{w} \\ \mathbf{0}^T & 1 \end{pmatrix}$$
$$\Rightarrow \boldsymbol{u} = \hat{\boldsymbol{u}} + \frac{\partial \boldsymbol{x}}{\partial \boldsymbol{\chi}}\boldsymbol{w}, \tag{3.13}$$

which may be rewritten as

$$\mathbf{c} = \frac{\partial \boldsymbol{x}}{\partial \boldsymbol{\chi}}\boldsymbol{w}, \tag{3.14}$$

where $\mathbf{c} = \boldsymbol{u} - \hat{\boldsymbol{u}}$ is the relative velocity between the material particle and the mesh.

3.1.1 ALE form of the Navier-Stokes equations

With the ALE framework in mind, it is now necessary to obtain the conservation equations for mass and momentum. For the sake of convenience of presentation, the incompressible Navier-Stokes equations in the Eulerian configuration presented in chapter 1 are rewritten here:

$$\rho\left(\frac{\partial \boldsymbol{u}}{\partial t}\bigg|_{\boldsymbol{x}} + \boldsymbol{u} \cdot \nabla \boldsymbol{u}\right) - \nabla \cdot \boldsymbol{\sigma} - \rho\mathbf{g} = \mathbf{0} \tag{3.15}$$

$$\nabla \cdot \boldsymbol{u} = 0 \tag{3.16}$$

To express the ALE form of the Navier-Stokes equations, one just need to replace the material velocity $\boldsymbol{u}$ with the convective velocity $\mathbf{c}$ in the convective terms:

$$\rho\left(\frac{\partial \boldsymbol{u}}{\partial t}\bigg|_{\boldsymbol{\chi}} + \mathbf{c} \cdot \nabla \boldsymbol{u}\right) - \nabla \cdot \boldsymbol{\sigma} - \rho\mathbf{g} = \mathbf{0} \tag{3.17}$$

$$\nabla \cdot \boldsymbol{u} = 0 \tag{3.18}$$

and the initial and boundary conditions now are:

$$
\begin{aligned}
\boldsymbol{u} &= \boldsymbol{u}_D & &\text{on } \Gamma_D \\
\mathbf{n} \cdot \boldsymbol{\sigma} &= \mathbf{t} & &\text{on } \Gamma_N, \\
\boldsymbol{u}(t=0) &= \boldsymbol{u}_0 & &\forall \boldsymbol{x} \in \Omega_0 \\
p(t=0) &= p_0 & &\forall \boldsymbol{x} \in \Omega_0 \\
\boldsymbol{u} &= \hat{\boldsymbol{u}} & &\text{on } \Gamma_w
\end{aligned}
\tag{3.19}
$$

where the last condition is directly related with the ALE description, representing in this case the assumption that the fluid adheres to the structure (no-slip condition). Here, Γ_w is the boundary of the structure embedded in the fluid (interface of the fluid and solid domains).

3.2 Partitioned simulation of fluid-structure interaction

The coupling of the fluid and structural response can be achieved numerically in different ways, but in all cases the conditions of displacement compatibility and traction

equilibrium along the structure-fluid interfaces must be satisfied (Bathe and Zhang, 2004):

Displacement compatibility:

$$\mathbf{d}_f = \mathbf{d}_s \quad \text{on } \Gamma_w \tag{3.20}$$

Stress equilibrium:

$$\mathbf{f}_f = \mathbf{f}_s \quad \text{on } \Gamma_w \tag{3.21}$$

where $\mathbf{d}_f$ and $\mathbf{d}_s$ are the displacements, $\mathbf{f}_f$ and $\mathbf{f}_s$ are the tractions of the fluid and the structure, respectively. A general description of these interface compatibility conditions considering different meshes for the fluid and structural domains is depicted in figure (3.2).
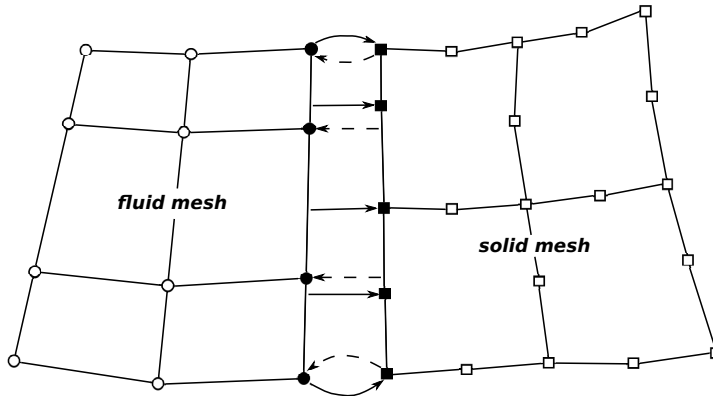
Figure 3.2: Mappings of displacements and tractions on fluid-structure interfaces. The solid arrows indicate traction mapping while the dashed ones indicate displacement mapping (Bathe and Zhang, 2004).

A straightforward way to satisfy the discrete version of equations (3.20) and (3.21) is to solve the fluid and the structure problems at the same time in a unique solver, approach usually known as *monolithic*. A monolithic method is typically *strongly coupled*, meaning that the equations (3.20) and (3.21) are satisfied after time discretization. Nevertheless, a monolithic scheme often requires a huge computational effort and is software-wise unmanageable (Farhat et al., 1998). Alternatively, these equations can

be solved by a *partitioned* (sometimes called *staggered* or *segregated*) procedure, where the solution of the coupled problem is advanced over the fluid, structure and dynamic mesh components separately. Then, three codes are needed: `CMD` (Computational Mesh Dynamics) which computes the mesh dynamics, `CSD` (Computational Structure Dynamics) which computes the structure dynamics and `CFD` (Computational Fluid Dynamics) which computes the fluid dynamics. By applying such procedure it is possible to use optimal discretization and solution methods inherent to each discipline while preserving code modularity. Among the partitioned schemes it is possible to differentiate between *weakly* and *strongly* coupled ones. A scheme is called *weakly* (or *loosely* or *explicit*) coupled if equations (3.20) and (3.21) are not completely satisfied at each time step (fluid and solid velocities do not exactly match at the interface). However, if accuracy and/or numerical stability require it, predictor/corrector iterations can be added in order to fulfill exactly the equations (3.20) and (3.21) in which case the partitioned procedure becomes a strongly coupled solution algorithm (Storti et al., 2009).

To illustrate the applicability of partitioned schemes in the study of body aerodynamics problems, in the following section the flutter of a suspension bridge is simulated. A weakly coupling algorithm is implemented and tested in a commercial CFD code.

3.2.1 Numerical test: bridge aerodynamics

Among the different topologies of bridges, *suspension* bridges span the greatest distances. Due to their flexibility, lightness and very low structural damping, these structures are very sensitive to wind actions. Therefore, a key factor in its design process is a dynamic phenomenon known as flutter, which is induced by the fluid-structure coupling. The flutter occurs when the damping induced by the fluid to the structure makes the structure damping negative (Badia and Codina, 2007).

The objective of this numerical test is to implement and evaluate a coupling algorithm between a fluid solver and a structural solver in order to perform a partitioned simulation of the fluid-structure interaction of the wind acting on the Great Belt East bridge (Denmark). As fluid solver the Fluent software (Fluent Inc.) was used.

The Great Belt East bridge is one of the largest suspension bridges in the world. It has a section of $W = 31$ m width and $B = 4.4$ m tall, and a main span of 1624 m, figure (3.3). As it is usually done in wind tunnel tests, the 3D brigde model was

Figure 3.3: Great Belt East suspension brigde.

reduced to a 2D problem. In figure (3.4) a sketch of the spring stiffnesses applied to the elastic center (EC) along with the flexural and torsional displacements is shown. The 2D cross-section was considered to be a rigid body.
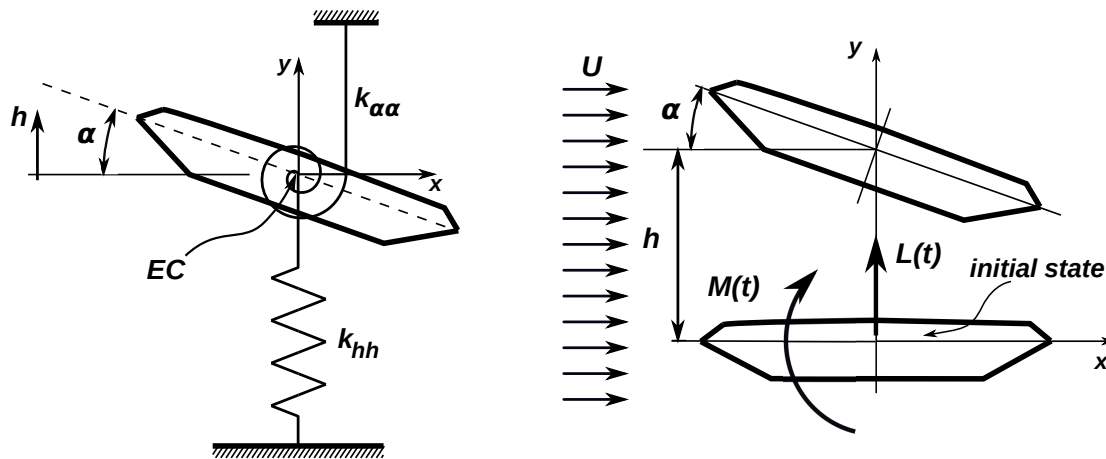
Figure 3.4: Elastic support of the bridge section on translational and rotational springs (*left*). The bridge section in initial and deformed position (*left*).

The bridge section movement with small vibration amplitudes is described by the following linearized system of ordinary differential equations (Svácek et al., 2007):

Mass per unit length, m (kg/m)	2.27×10^3
Vertical static moment on elastic center per unit length, S_a (kg m/m)	1.61×10^4
Mass moment of inertia on elastic center per unit length, I_α (kg m^2/m)	2.47×10^6
Vertical spring stiffness, k_h (N/m^2)	8.78×10^3
Torsional spring stiffness, k_α (N m/m^2)	7.21×10^6
Vertical logarithmic damping, d_h (%)	1
Torsional logarithmic damping, d_α (%)	0.6

Table 3.1: Great Belt East bridge properties (Badia and Codina, 2007).

$$m\ddot{h} + k_h h + S_\alpha \ddot{\alpha} + d_h \dot{h} = -L(t)$$
$$S_\alpha \ddot{h} + I_\alpha \ddot{\alpha} + k_\alpha \alpha + d_\alpha \dot{\alpha} = M(t) \tag{3.22}$$

where $L(t)$ and $M(t)$ denote the aerodynamical lift force and torsional moment, respectively, m is the mass of the bridge section, S_α and I_α are the static and inertia moments around the elastic center EC, k_h and k_α denotes the bending and torsional stiffness. Furthermore, α represents the rotational displacement around the elastic center EC and h is the vertical displacement of the elastic center EC.

The system (3.22) is equipped with the initial conditions $h(0) = \alpha(0) = \dot{h}(0) = \dot{\alpha}(0) = 0$. In order to transform this system into a first-order ODE system, it is written in matrix format,

$$\begin{bmatrix} m & S_\alpha \\ S_\alpha & I_\alpha \end{bmatrix} \begin{pmatrix} \ddot{h} \\ \ddot{\alpha} \end{pmatrix} + \begin{bmatrix} d_h & 0 \\ 0 & d_\alpha \end{bmatrix} \begin{pmatrix} \dot{h} \\ \dot{\alpha} \end{pmatrix} + \begin{bmatrix} k_h & 0 \\ 0 & k_\alpha \end{bmatrix} \begin{pmatrix} h \\ \alpha \end{pmatrix} = \begin{pmatrix} -L \\ M \end{pmatrix}$$

that is,

$$\boldsymbol{M}\ddot{\boldsymbol{u}} + \boldsymbol{D}\dot{\boldsymbol{u}} + \boldsymbol{K}\boldsymbol{u} = \boldsymbol{f} \quad \Rightarrow \quad \ddot{\boldsymbol{u}} = \boldsymbol{M}^{-1} \left[\boldsymbol{f} - \boldsymbol{D}\dot{\boldsymbol{u}} - \boldsymbol{K}\boldsymbol{u} \right]$$

By making $\boldsymbol{s} = \dot{\boldsymbol{u}}$, a new system of equations is obtained:

$$\dot{s} = M^{-1} \left[f - D\dot{u} - Ku \right]$$
$$s = \dot{u}$$

and then

$$\dot{s}_1 = \frac{1}{mI_\alpha - S_\alpha^2} \left[-I_\alpha \left(L + d_h s_1 + k_h h \right) - S_\alpha \left(M - d_\alpha s_2 - k_\alpha \alpha \right) \right]$$
$$\dot{s}_2 = \frac{1}{mI_\alpha - S_\alpha^2} \left[S_\alpha \left(L + d_h s_1 + k_h h \right) - m \left(M - d_\alpha s_2 - k_\alpha \alpha \right) \right]$$
$$s_1 = \dot{h}$$
$$s_2 = \dot{\alpha}$$

(3.23)

This system can be solved numerically by, for example, the fourth-order Runge-Kutta method:

$$\Delta h_1 = \dot{h} \ \Delta t$$
$$\Delta \alpha_1 = \dot{\alpha} \ \Delta t$$
$$\Delta \dot{h}_1 = F_1(h, \alpha, \dot{h}, \dot{\alpha}, t) \ \Delta t$$
$$\Delta \dot{\alpha}_1 = F_2(h, \alpha, \dot{h}, \dot{\alpha}, t) \ \Delta t$$

$$\Delta h_2 = (\dot{h} + \tfrac{1}{2}\Delta \dot{h}_1) \ \Delta t$$
$$\Delta \alpha_2 = (\dot{\alpha} + \tfrac{1}{2}\Delta \dot{\alpha}_1) \ \Delta t$$
$$\Delta \dot{h}_2 = F_1(h + \tfrac{1}{2}\Delta h_1, \alpha + \tfrac{1}{2}\Delta \alpha_1,$$
$$\dot{h} + \tfrac{1}{2}\Delta \dot{h}_1, \dot{\alpha} + \tfrac{1}{2}\Delta \dot{\alpha}_1, t + \tfrac{1}{2}\Delta t) \ \Delta t$$
$$\Delta \dot{\alpha}_2 = F_2(h + \tfrac{1}{2}\Delta h_1, \alpha + \tfrac{1}{2}\Delta \alpha_1,$$
$$\dot{h} + \tfrac{1}{2}\Delta \dot{h}_1, \dot{\alpha} + \tfrac{1}{2}\Delta \dot{\alpha}_1, t + \tfrac{1}{2}\Delta t) \ \Delta t$$

$$\Delta h_3 = (\dot{h} + \tfrac{1}{2}\Delta \dot{h}_2) \ \Delta t$$
$$\Delta \alpha_3 = (\dot{\alpha} + \tfrac{1}{2}\Delta \dot{\alpha}_2) \ \Delta t$$
$$\Delta \dot{h}_3 = F_1(h + \tfrac{1}{2}\Delta h_2, \alpha + \tfrac{1}{2}\Delta \alpha_2, \dot{h} + \tfrac{1}{2}\Delta \dot{h}_2, \dot{\alpha} + \tfrac{1}{2}\Delta \dot{\alpha}_2, t + \tfrac{1}{2}\Delta t) \ \Delta t$$
$$\Delta \dot{\alpha}_3 = F_2(h + \tfrac{1}{2}\Delta h_2, \alpha + \tfrac{1}{2}\Delta \alpha_2, \dot{h} + \tfrac{1}{2}\Delta \dot{h}_2, \dot{\alpha} + \tfrac{1}{2}\Delta \dot{\alpha}_2, t + \tfrac{1}{2}\Delta t) \ \Delta t$$
$$\Delta h_4 = (\dot{h} + \Delta \dot{h}_3) \ \Delta t$$
$$\Delta \alpha_4 = (\dot{\alpha} + \Delta \dot{\alpha}_3) \ \Delta t$$
$$\Delta \dot{h}_4 = F_1(h + \Delta h_3, \alpha + \Delta \alpha_3, \dot{h} + \Delta \dot{h}_3, \dot{\alpha} + \Delta \dot{\alpha}_3, t + \Delta t) \ \Delta t$$
$$\Delta \dot{\alpha}_4 = F_2(h + \Delta h_3, \alpha + \Delta \alpha_3, \dot{h} + \Delta \dot{h}_3, \dot{\alpha} + \Delta \dot{\alpha}_3, t + \Delta t) \ \Delta t$$

thus, in each time step it is possible to compute the displacements and velocities of the

next time step by the following equations:

$$
\begin{aligned}
h_{i+1} &= h_i + \frac{1}{6}(\Delta h_1 + 2\Delta h_2 + 2\Delta h_3 + \Delta h_4) \\
\alpha_{i+1} &= \alpha_i + \frac{1}{6}(\Delta \alpha_1 + 2\Delta \alpha_2 + 2\Delta \alpha_3 + \Delta \alpha_4) \\
\dot{h}_{i+1} &= \dot{h}_i + \frac{1}{6}(\Delta \dot{h}_1 + 2\Delta \dot{h}_2 + 2\Delta \dot{h}_3 + \Delta \dot{h}_4) \\
\dot{\alpha}_{i+1} &= \dot{\alpha}_i + \frac{1}{6}(\Delta \dot{\alpha}_1 + 2\Delta \dot{\alpha}_2 + 2\Delta \dot{\alpha}_3 + \Delta \dot{\alpha}_4)
\end{aligned}
\tag{3.24}
$$

Once the configuration of the structure is updated, the drag force, D, the lift force, L, and the torsional moment are computed again.

Weakly coupled FSI simulation with Fluent. This test case was solved numerically using as fluid solver the commercial CFD package Fluent 6.3.26 (Fluent Inc.). In order to connect the CFD and CSD codes (here the CSD code is simply composed by equations (3.23)-(3.24) as it is considered a rigid solid body) a coupling algorithm must be introduced.

Basically, the weakly coupling used here consists of the following tasks:

1) The Fluent solver computes the flow problem in time step t_i.

2) With the resulting stress distribution on the fluid-structure interface, the coupling algorithm computes the forces that has to be applied to the structure.

3) The displacement of the structure is calculated using equations (3.23)-(3.24).

4) The new position of the fluid-structure interface for time step t_{i+1} is obtained.

Fluent can deal with flows where the shape of the domain changes with time due to motion on the domain boundaries by using the *dynamic mesh* model (Fluent Inc., 2010). The coupling algorithm perform steps *2)* and *3)* setting the motion of the solid boundaries as an user-defined function (UDF). Then Fluent updates the computational mesh automatically at each time step based on the new positions of the boundaries.

3. FLUID-STRUCTURE INTERACTION

The computational mesh was divided in three differente regions, figure (3.5): a static region, where no mesh deformation was allowed; a dynamic region, where the mesh deforms according to some prescribed method; and a mobile region, where the mesh follows the displacement of the structure as a rigid body, i.e., without deforming its cells. The *spring-based smoothing* method was used to update the mesh in the dynamic region. In a mesh with triangular elements, this method adjust the interior node locations based on known displacements at the boundary nodes without changing the mesh connectivity.
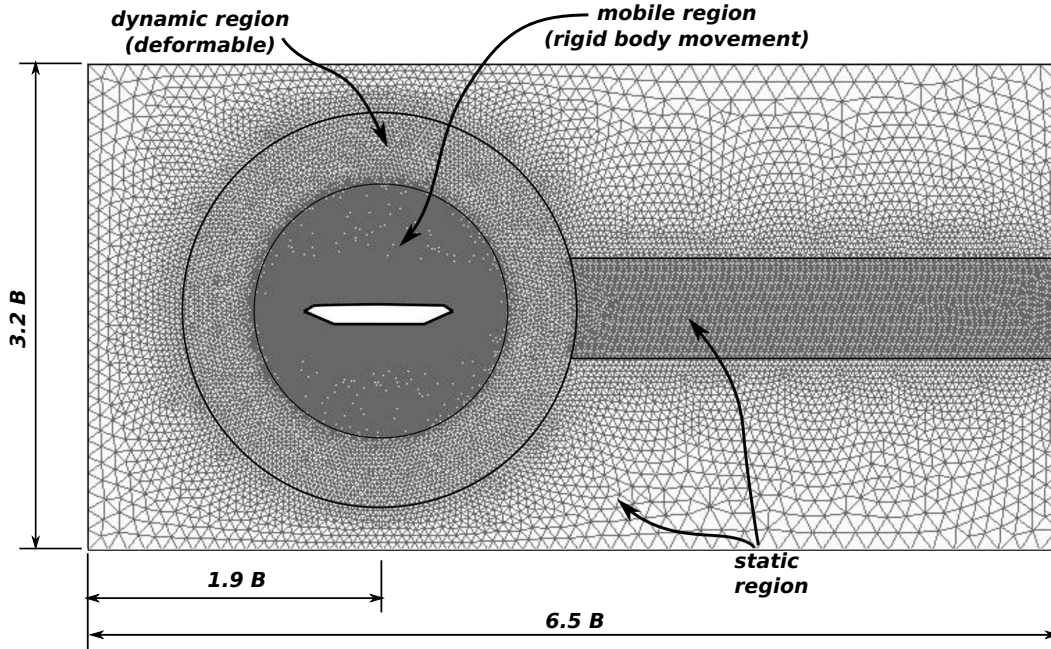
Figure 3.5: Computational mesh used. The distribution of the different mesh regions allows to reduce the computational burden.

Results. Following the work of Frandsen (2004) an unsteady laminar flow was assumed and no railings were included on the bridge deck model. Constant longitudinal velocity $(u_x, v_y = 0)$ was set at the inflow of the fluid domain and zero outlet pressure. Slip boundary condition $(v_y = 0)$ was prescribed at the upper and lower domain boundaries while no-slip condition $(u_x = v_y = 0$ or, equivalently, $u_x = u_x^s; v_y = v_y^s$ when the bridge moves, where the superscript s indicates "structure").

The velocity was incremented in several steps in order to identify that flutter onset velocity. The time history of the aerodynamic lift coefficient,

$$C_L = \frac{F_L}{\frac{1}{2}U^2 B} \qquad (3.25)$$

is shown in figure (3.6). In equation (3.25) F_L represents the aerodynamic lift force and U the inlet velocity.
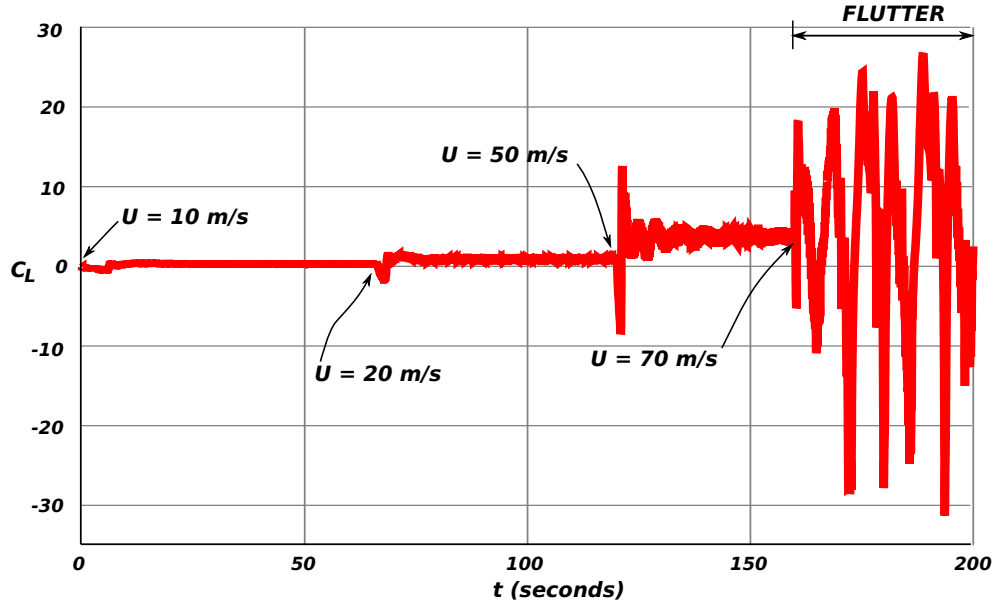
Figure 3.6: Time history of the lift coefficient.

The flutter region was clearly detected for an inlet velocity $U = 70$ m/s, which agrees with the range of values reported by several authors, see table (3.2). In figure (3.7), two snapshots of the bridge section are shown, at a time when the flutter limit of 70 m/s is reached. Despite the laminar flow assumption, it can be seen how the flow is detached from the surface of the structure to eventually generate the vortex shedding phenomenon.

Source	Flutter limit (m/s)
FEM (Frandsen, 2004)	70
FEM (Selvam et al., 2002)	69
FEM (Braun and Awruch, 2003)	69
Wind tunnel tests (from Frandsen (2004))	67-75

Table 3.2: Flutter limit predictions from different methods.
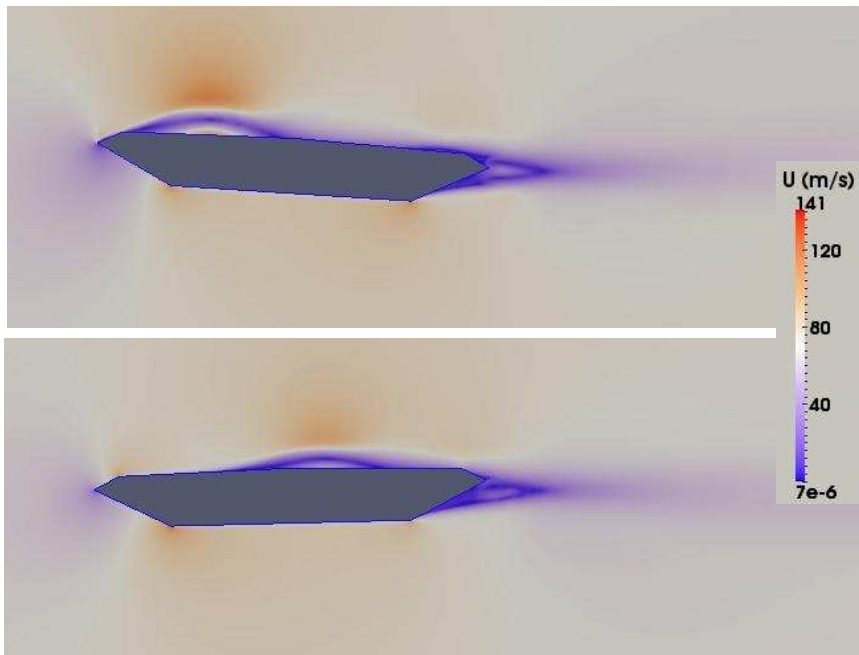
Figure 3.7: Flow and structure configuration in two snapshots of the simulation.

3.2.2 Strongly coupled partitioned algorithm in PETSc-FEM

It was demonstrated in the previous section that the coupling algorithm used for the FSI simulation has provided good results. Consequently, this algorithm is used (after some adaptation) for the FSI analysis in the next chapter. However, as in the rest of this thesis the computational code used is the PETSc-FEM code, a brief description of the FSI implementation in this code is required.

In PETSc-FEM the temporal algorithm that performs the coupling between the structure and the fluid codes is a fixed point iteration scheme over the variables of both fluid and structure systems. Inside of the time step loop the algorithm is equipped with an inner loop called *'stage'*, so if the *'stage loop'* converges, then a *'strongly coupled'*

algorithm is obtained. Hereafter, this algorithm is called *'staggered algorithm'*. The basic scheme is similar to the one described previously and proceeds as follows:

i) Transferring the motion of the wet boundary of the solid to the fluid problem.

ii) Updating the position of the fluid boundary and the bulk fluid mesh accordingly.

iii) Advancing the fluid system and compute new pressures.

iv) Converting the new fluid pressure (and stress field) into a structural load.

v) Advancing the structural system under the flow loads.

For simplicity, the basic algorithm can be thought as if there were no *'concurrence'* among the codes, i.e. at a given time only one of them is running. This can be controlled using *'semaphores'* and this is done using Message Passing Interface (MPI) *'synchronization messages'*. This staggered procedure, which can be treated as a weakly coupled solution algorithm, can also be equipped with an outer loop in order to assure the convergence of the interaction process. The algorithm can be stated as in Algorithm 1. At time t_n, $\mathbf{w}^n$ is the fluid state vector $(\rho, \mathbf{v}, p)$, $\mathbf{u}^n$ is the displacement vector (structure state vector), $\dot{\mathbf{u}}^n$ the structure velocities and $\mathbf{X}^n$ the fluid mesh node positions. In this case, both fluid and structure partitions are integrated with the trapezoidal algorithm (with trapezoidal parameter $0 < \alpha_{\text{trap}} \leq 1$) but another integration scheme could be used, such as linear multisteps methods, depending on the particular application (Mavriplis and Yang, 2005). The number of time steps in the simulation is indicated by n_{step}, n_{stage} is the number of stages in the coupling scheme and n_{nwt} is the number of Newton loops in the non-linear problem.

In each time step the fluid is first advanced using the previously computed structure state $\mathbf{u}^n$ and the current estimated value $\mathbf{u}_p^{n+1}$. In this way, a new estimation for the fluid state $\mathbf{w}^{n+1}$ is computed. Next the structure is updated using the forces of the fluid from states $\mathbf{w}^n$ and $\mathbf{w}^{n+1}$. The estimated state $\mathbf{u}_p^{n+1}$ is predicted using a second or higher order approximation:

$$\mathbf{u}_p^{(n+1)} = \mathbf{u}^n + \alpha_0 \Delta t \dot{\mathbf{u}}^n + \alpha_1 \Delta t (\dot{\mathbf{u}}^n - \dot{\mathbf{u}}^{n-1}). \tag{3.26}$$

3. FLUID-STRUCTURE INTERACTION

Algorithm 1 Strong FSI coupling via fixed point iteration

1: Initialize variables:
2: **for** $n = 0$ to n_{step} **do** {*Main time step loop*}
3:     $t^n = n\Delta t,$
4:     {*CFD CODE:*}
5:     *receive u^n from* STRUCTURE
6:     $\mathbf{X}^n = \text{CMD}(\mathbf{u}^n)$ {*run CMD code*}
7:     $\mathbf{u}^{(n+1)P} = \mathbf{u}^{(n+1,0)} = \text{predictor}(\mathbf{u}^n, \mathbf{u}^{n-1})$ {*compute predictor*}
8:     {*STRUCTURE CODE:*}
9:     *receive $\mathbf{w}^n$ from* FLUID {*fluid state*}
10:     **for** $i = 0$ to n_{stage} **do** {*stage loop*}
11:       {*CFD CODE:*}
12:       *receive $\mathbf{u}^{(n+1,i)}$ from* STRUCTURE
13:       $\mathbf{X}^{n+1,i+1} = \text{CMD}(\mathbf{u}^{n+1,i})$
14:       {*Compute surface normals and velocities*}
15:       **for** $k = 0$ to n_{nwt} **do** {*Fluid Newton loop*}
16:         $\mathbf{w}^{n+1,i+1} = \text{CFD}(\mathbf{w}^n, \mathbf{X}^{n+1,i+1}, \mathbf{X}^n)$
17:       **end for**
18:       *send $\mathbf{w}^{n+1,i+1}$ to* STRUCTURE
19:       {*FLUID CODE: after each stage iteration*}
20:       {*CSD CODE:*}
21:       *receive $\mathbf{w}^{n+1,i+1}$ from* FLUID;
22:       *compute structural loads $(\mathbf{w}^n, \mathbf{w}^{n+1,i+1})$*
23:       **for** $k = 0$ to n_{nwt} **do** {*Structure Newton loop*}
24:         $\mathbf{u}^{n+1,i+1} = \text{CSD}(\mathbf{w}^n, \mathbf{w}^{n+1,i+1})$
25:       **end for**
26:       *send $\mathbf{u}^{n+1,i+1}$ to* FLUID
27:       {*STRUCTURE CODE: after each stage iteration*}
28:     **end for**
29:     {*FLUID CODE: after each time step*}
30:     *send $\mathbf{u}^n$ to* FLUID;
31:     {*STRUCTURE CODE: after each time step*}
32:     *send $\mathbf{w}^n$ to* STRUCTURE
33: **end for**

---

were α_0 and α_1 are two real constants. The predictor (3.26) is trivial if $\alpha_0 = \alpha_1 = 0$, first-order time-accurate if $\alpha_0 = 1$ and second-order time-accurate if $\alpha_0 = 1$ and $\alpha_1 = 1/2$.

In the work of Piperno and Farhat (2001) there is an extended description about the use of the predictor (3.26) on FSI problems and the energy transfer between the fluid and the structure. It was proved that monolithic schemes and strongly-coupled staggered schemes conserve energy-transfer at the fluid-structure interface boundary, whereas weak-coupled algorithms introduce after a certain amount of time t an artificial energy $E = \mathcal{O}(\Delta t^p)$, where p is the order of the prediction.

Once the coordinates of the structure are known, the coordinates of the fluid mesh nodes are computed by a *'Computational Mesh Dynamics'* code, which is symbolized as:

$$\mathbf{X}^n = \text{CMD}(\mathbf{u}^n). \tag{3.27}$$

At the beginning of each fluid stage there is a computation of surface normals and velocities. This is necessary due to the time dependent slip boundary condition for the inviscid case, and also when using a non-slip boundary condition, where the fluid interface has the velocity of the moving solid wall, i.e., $\mathbf{v}|_\Gamma = \dot{\mathbf{u}}|_\Gamma$.

Chapter 4

Applications to road vehicle aerodynamics

Understanding ground vehicles aerodynamics allows us to optimize the operation of a wide spectrum of road vehicles, that ranges from road passenger transport (cars, buses, trains) to road comercial transport (trucks and trains). Road vehicle aerodynamics is a complex topic due to the interaction between the air flow and the ground.

Besides of fuel consumption, aerodynamics is directly related to vehicle stability: the flow-vehicle interaction impacts on the straight line stability (roadholding), dynamic passive steering and the response to crosswind. Furthermore, there are other issues where the aerodynamics plays an important role: the accumulation of droplets of rain water on windows and outside mirrors, the accumulation of dirt in headlights, wind noise, etc. In summary, aerodynamics has a significant impact on the design of a vehicle and requires a detailed analysis of the flow around it, including unsteady and turbulent flow phenomena (Hucho, 1998).

A road vehicle has also aerodynamic properties that are specific to this kind of vehicles. Due to its geometry, it can be considered a *bluff body*, which means that drag is mainly due to the pressure acting on it. Skin friction, caused by viscous shear forces on the surface of the vehicle, has only a small contribution to the drag. Flow separation occurs in the back of the body, creating large recirculation regions in the near wake, resulting in a lower pressure on the back surfaces, see figure (4.1). This

mechanism produce an increase in the difference between the pressure acting on the front and on the back of the vehicle. According to Wood (2004), approximately the 75 % of the total drag of a light ground vehicle is due to the pressure drag, while for heavy ground vehicles around the 90 % of the drag is pressure drag.
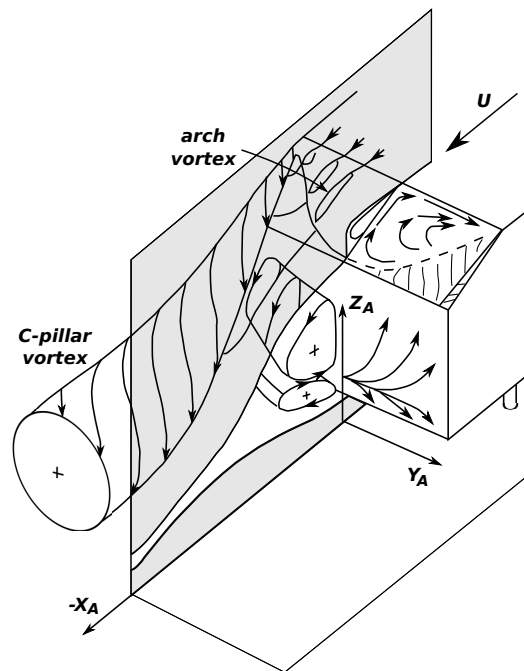
Figure 4.1: Vortex system behind a road vehicle (Ahmed et al., 1984).

The flow around three-dimensional bluff bodies is characterized by separated shear layers formed at the top, bottom and side edges of the body (Gürlek, 2008). The wake is often dominated by streamwise vortices (which may interact with each other) and its unsteady nature can affect the aerodynamic forces acting on the body. If the frequency of these forces equals or is close to the natural frequency of the body, it could cause vibrations which can seriously impact on the comfort of the driver. The complexity associated with time-varying flows causes that the vast part of the investigations has been limited to time-averaged behaviour.

Until a few years ago, complex aerodynamic studies on road vehicles were performed almost exclusively in wind tunnel facilities. Even today, they still are more frequently used than numerical studies. Nevertheless, CFD nowadays allows predicting unsteady aerodynamic effects due to the improvement of computational power and efficiency.

RANS approach was widely used in vehicle aerodynamics studies (Basara et al., 2001; Guilmineau, 2008), however, unlike the steady-state solution that can rely on RANS method, the application of CFD when solving unsteady aerodynamic problems required the use of the LES technique. For example, according to Guilmineau (2008), RANS simulations does not accurately predict the flow pattern around the Ahmed body for a slant angle of $25°$ while for an angle of $30°$ this approach worked well. This is because RANS simulations strongly depend on the implemented turbulence model and geometric characteristics of the problem. Meanwhile, using LES on this particular test case has demostrated that it can predict the location at which the flow separates from the model as well as the flow structure on the wake (Krajnovic and Davison, 2004).

As real vehicles have complex geometries, numerical simulations are often carried out over simplified (generic) forms of vehicles. Although many different types of simplified vehicle geometries were proposed, one of the most used is the so called Ahmed model (Ahmed et al., 1984). This model is considered a standard benchmark and several investigations have been evoked to implement numerical and experimental studies of the flow around this particular model (e.g. Krajnovic and Davison (2005), Hinterberger et al. (2004), Serre et al. (2011)).

Another aspect of the automotive aerodynamics that is rarely explored in the literature is the interaction between a dynamic road vehicle model and the airflow. Cheng et al. (2011) investigated the stability characteristics of road vehicles under pitching oscillation. By imposing sinusoidal-forced-pitching oscillation on a sedan-type model vehicle during the LES, the authors found that the front-pillar vortex is the main factor that imparts the unstable tendency in the vehicle's pitching behaviours. In line with this research, the same authors proposed a dimensionless coefficient that reflects the pitching stability of a vehicle in another paper (Cheng et al., 2012).

As it was pointed out by Krajnovic et al. (2011), forces and moments obtained in tests where dynamic flow conditions were used, have shown to be different from those found in steady flow conditions. A common approach is to evaluate the aerodynamic performance using static conditions, where the position of the model is changed discontinuously. This approach is known as "quasi-steady" and it is widely employed in experimental tests and numerical simulations.

In this Chapter several test cases regarding the simulation of wind flow passing through a vehicle are analyzed. Different scenarios are considered, i.e. different bound-

ary conditions and with static and dynamic models.

4.1 Ahmed body

As was mentioned in Chapter 2 of this thesis, the Ahmed body is a simplified road vehicle model defined by Ahmed et al. (1984), see figure (4.2). A more detailed description of the model can be found in the work of Franck (2004); Franck et al. (2009) and references therein.
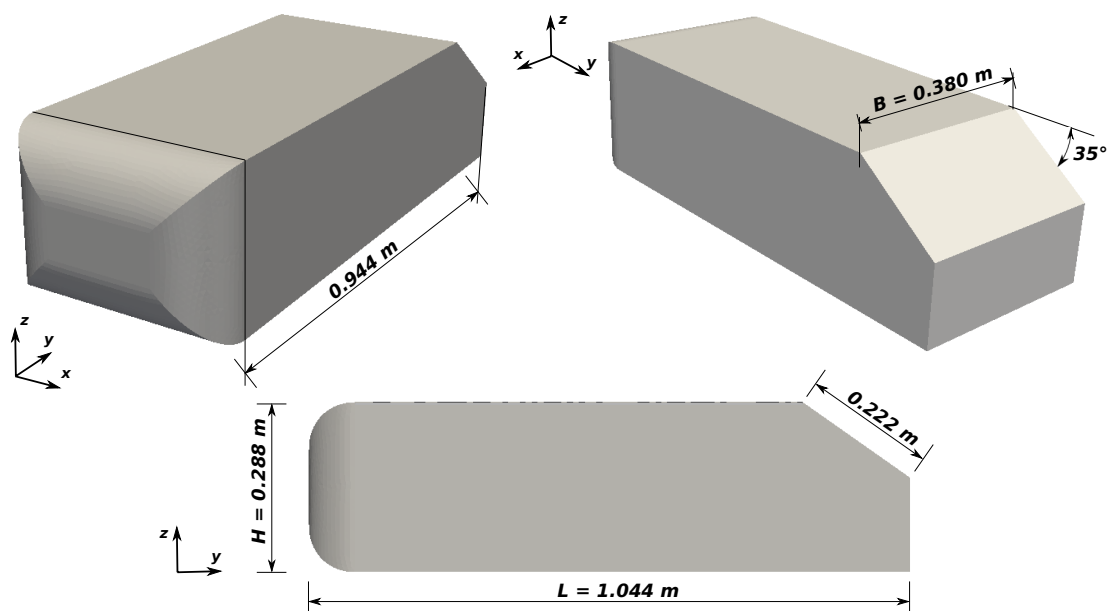
Figure 4.2: Main dimensions of the simpified model proposed by Ahmed et al. (1984).

In the test performed by Ahmed et al. (1984), the model was fixed on cylindrical stilts, 50 mm above a ground board, 3 m wide and 5 m long, in an open tunnel test section. A wind speed of 60 m/s was used, corresponding to a model length based Reynolds number of 4.29×10^6 and a turbulence intensity less than 0.5%. The authors found that the major contribution to the pressure drag comes from the slant and vertical base surface of rear end. However, several investigations were made with a smaller Reynolds number, a desired feature when LES is considered. Hinterberger et al. (2004) performed a LES of the flow over the Ahmed body with a Reynolds number of 2.88×10^6 leading to a bulk velocity of 40 m/s while Krajnovic and Davison (2004) used an even smaller velocity of approximately 10 m/s. Interestingly, in this later work

the authors have found that the level of the Reynolds number has small influence on the results in highly separated flows around cars provided that it is high enough.

4.1.1 Numerical method

An incompressible Newtonian viscous fluid model is adopted with kinematic viscosity $\mu = 1.45 \times 10^{-5}$ m^2/s and density $\rho = 1.225$ kg/m^3. The simulations were performed with the PETSc-FEM code using the Finite Element Method to solve the momentum and continuity equations for the velocity and pressure at each node and at each time step. The SUPG/PSPG discretization scheme of the incompressible Navier-Stokes equations are implemented.

The simulations were performed using two different Beowulf kind of clusters. The *"Aquiles"* cluster, with 80 nodes Pentium 4 CPU 3.00 GHz and a server Xeon E5335 2.00 GHz, interconnected via a Gigabit Ethernet network, and the *"Coyote"* cluster, with 7 nodes Xeon E5420 2.50 GHz (2 x 4 cores), 16 nodes Xeon W3690 3.47 GHz (1 x 6 cores) and a server Xeon E5335 2.00 GHz (2 x 4 cores).

4.1.2 Computational domain and inlet boundary conditions

As it was done in Chapter 2, the computational domain was adjusted to the main dimensions of the "Jacek Gorecki" boundary layer wind tunnel in order to provide data for a later comparison with an experimental test. The "Jacek Gorecki" is an open circuit wind tunnel located at the Northeast National University at Resistencia (Chaco), Argentina, which has a 2.4 m wide × 1.8 m high × 22.4 m long working section (Wittwer and Möller, 2000). As can be seen in figure (4.3), the computational domain has a width $W = 2.40$ m with a height $H = 1.80$ m and 6.264 m of length. The center of the coordinate system was placed at the inlet plane ($x = 0$ is the symmetry plane, $y = 0$ is the inlet plane, $z = 0$ is the ground plane). No advantage was taken of the symmetry of the problem in order to perceive any asymmetry in the solution.

The body was located at $2L$ downstream (y-direction) the inlet section and at $3L$ upstream the outlet boundary to allow full development of the flow downstream the model, totaling an extension of $6L$. Non-slip boundary condition was prescribed at
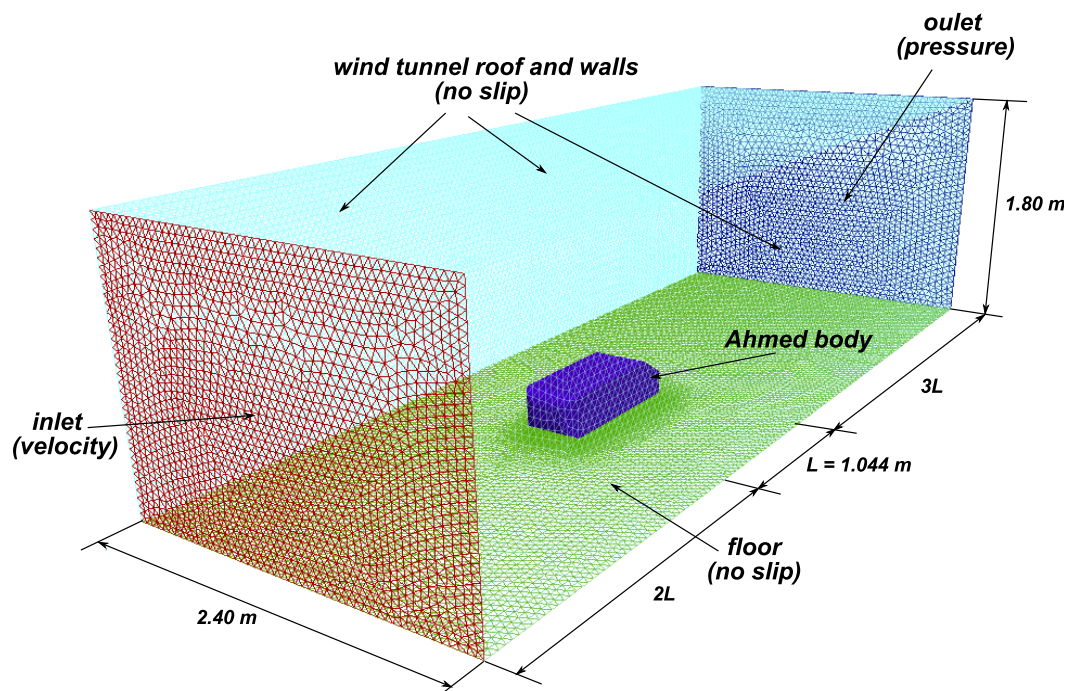
Figure 4.3: Computational domain of the Ahmed test case.

ground, roof and tunnel walls, while null pressure was imposed at the outlet wall. With these conditions the blockage ratio was about 2.6%.

The cross section of the domain used in this work is larger than the one used by Krajnovic and Davison (2004) which consisted in a channel of approximately 1.87 m × 1.40 m (width × height). Also, the boundary conditions on the lateral walls and ceiling are different. In their work, Krajnovic and Davison (2004) treated the lateral surfaces and ceiling as slip surfaces using symmetry conditions in order to reproduce the experimental test of Lienhart and Becker (2003) who performed their experiment in a channel with a 3/4 open test section (with floor but without lateral surfaces or ceiling). This 3/4 open section configuration enables the flow across these surfaces while in the numerical simulation of Krajnovic and Davison (2004) and in the present work that is no possible, leading to a different blockage ratio condition.

The boundary condition at the inlet of the domain calls for a fully developed flow with boundary layers on roof, walls and floor, as this is the case in the wind tunnel test section. To achieve this condition, mean velocity profiles and turbulence intensity values were adopted in agreement with the values reported by Wittwer and Möller

(2000). Here again, an observation must be made. The maximum velocity value at the center of the wind tunnel test section is about 27 m/s. This leads to a model length based Reynolds number of approximately 1.91×10^6 which is less than the values reported in all the above cited references except for the work of Krajnovic and Davison (2004). Nevertheless, even with a smaller velocity they found, at least for the geometry of this simplified road vehicle model, that the external vehicle flow at high Reynolds numbers becomes independent of it.

4.1.3   Mesh details

The grid used for this test case has $462, 580$ nodes, $2, 192, 778$ elements and $h = 0.001$ m, being h the mean thickness of the first element layer (measured from the model surface). The grid was refined close to the body surface in order to account for viscous effects at the wall and to adequately capture the changes in flow variables within the boundary layer region. An unstructured mesh consisting of tetrahedral and prismatic (wedges) finite elements was used for these tests and was divided in three different regions to account for the mesh movement, figure (4.4). A more detailed discussion about this domain division is made in Section §4.1.5.
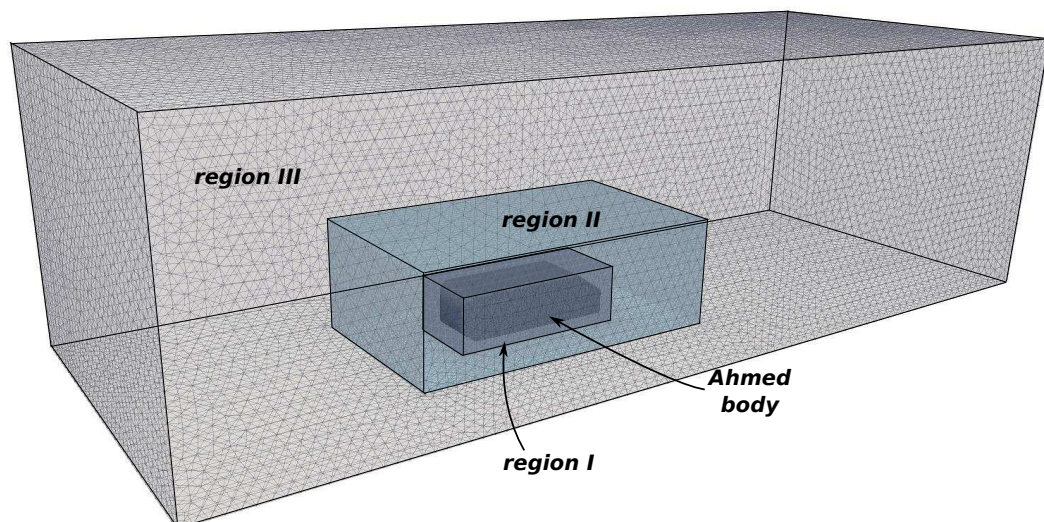
Figure 4.4: Different regions of the mesh.

4. APPLICATIONS TO ROAD VEHICLE AERODYNAMICS

Resolution. As the flow around a car is a wall-bounded one, its turbulence content is kept by the coherent motions in the boundary layer. To have some indication of the extent to which the flow can be resolved it is mandatory to consider several characteristic length scales associated with the problem (Tennekes and Lumley, 1972). Two length scales are commonly used, the Kolmogorov microscale and the Taylor microscale (Howard and Pourquie, 2002; Franck et al., 2009). The Kolmogorov microscale is associated with the smallest turbulent motions of the flow, computed by the following expression

$$\eta = A^{-1/4} Re_l^{-3/4} l \tag{4.1}$$

while the Taylor microscale is related with the length scale of the integral scale motions (length scales of the mean flow) and can be obtained by

$$\lambda = \sqrt{15} A^{-1/2} Re_l^{-1/2} l \tag{4.2}$$

where A is an $O(1)$ constant, l is the bulk integral scale and $Re_l = U_\infty L/\nu$ is the free stream Reynolds number, ν is the kinematic viscosity of the fluid and U_∞ the free stream velocity. Equations (4.1) and (4.2) are derived from empirical correlations.

In the present case, the following values are adopted: $A = 0.5$, $l \equiv L = 1.044$ m, $\nu = 1.45 \times 10^{-5}$ m^2/s. As it can be noted from the values listed in table (4.1), close to the body surface, the mesh spacing exceeds the Kolmogorov scale but it is smaller than the Taylor microscale, so it is expected that the large scale turbulent eddies down to the Taylor microscale size should be well represented by LES.

Re_l	η	λ	h
1.91×10^6	$2.31 \times 10^{-5}\ L$	$3.96 \times 10^{-3}\ L$	$9.6 \times 10^{-4}\ L$

Table 4.1: Grid resolution for the Ahmed test case.

4.1.4 Static model simulation

The time history of the aerodynamic forces and moments in all three directions, i.e., side (F_x), drag (F_y) and lift (F_z) forces (figure (4.5)) and pitch (M_x), roll (M_y) and

yaw (M_z) moments (figure (4.6)) were computed during the simulation by adding the viscous and pressure forces around the full three-dimensional model. The deviation (rms values) of the drag force was found to be around 1.3% of the mean value. The corresponding force coefficients were also computed as:

$$C_S = \frac{F_x}{\frac{1}{2}\rho U_\infty^2 A} \qquad C_D = \frac{F_y}{\frac{1}{2}\rho U_\infty^2 A} \qquad C_L = \frac{F_z}{\frac{1}{2}\rho U_\infty^2 A} \qquad (4.3)$$

being C_S, C_D and C_L the side, drag and lift force coefficientes, respectively, and A the frontal area. Mean and rms values of these coefficients are presented in table (4.2-(a)).

	(a)			(b)		
	C_S	C_D	C_L	C_S	C_D	C_L
mean	-0.006	0.297	0.151	-0.001	0.267	0.035
rms	0.008	0.013	0.017	0.010	0.013	0.022

Table 4.2: Ahmed static test: time-averaged side (C_S), drag (C_D) and lift (C_L) coefficients (mean and rms values). *(a)* no-slip condition in the tunnel floor, *(b)* sliding ground.

As can be noted, the mean drag force coefficient was found to be higher than the value $C_{D_{mean}} = 0.255$ obtained by Ahmed et al. (1984). Therefore, another simulation was performed under the same conditions except for the tunnel floor boundary condition, which was modified to simulate a moving ground by imposing the incoming mean velocity U_∞ as the velocity of the lower wall. This was done in order to validate the numerical model against the experimental study. The results of this later simulation are resumed in table (4.2-(b)). The mean drag force coefficient still exceeds the value reported by Ahmed et al. (1984) but with a difference less than 5%, highlighting the interference effect that the fixed floor boundary layer causes over the flow pattern and, as a consequence, over the aerodynamic forces.

4.1.5 Fluid-structure interaction study

Forced vibration. As a first step prior to the fully coupled fluid-structure interaction study, a test considering an imposed model movement was performed. The main idea behind this test was to verify the correct behaviour of the code in charge of the communication between the fluid problem and the structure problem. Two degrees of freedom were considered namely lateral movement and yawing, see figure (4.7). The
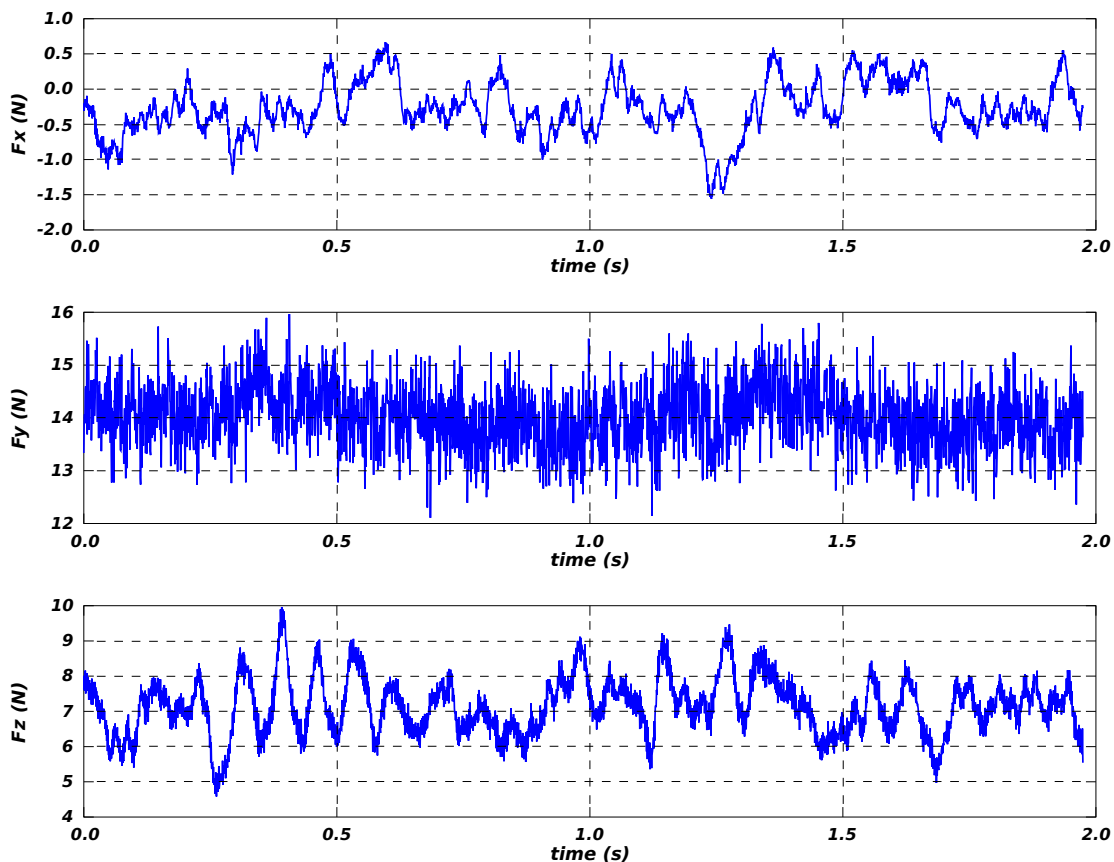
Figure 4.5: Time history of the aerodynamic forces.

geometric properties of the Ahmed body (assuming unitary constant density) are listed in table (4.3), where x_o, y_o and z_o are the distance of the local coordinate center from the front of the model and I_x, I_y and I_z are the moments of inertia about the local axes.

A forced-sinusoidal-yawing (M_z) and a forced-sinusoidal-lateral (F_x) oscillation were imposed on the vehicle model:

$$F_x = P_o \sin(\omega_F t)$$
$$M_z = M_o \sin(\omega_M t) \tag{4.4}$$

where ω_F and ω_F are the loading frequency of the lateral force and yawing moment, respectively. With these settings, the following system of ordinary differential equations
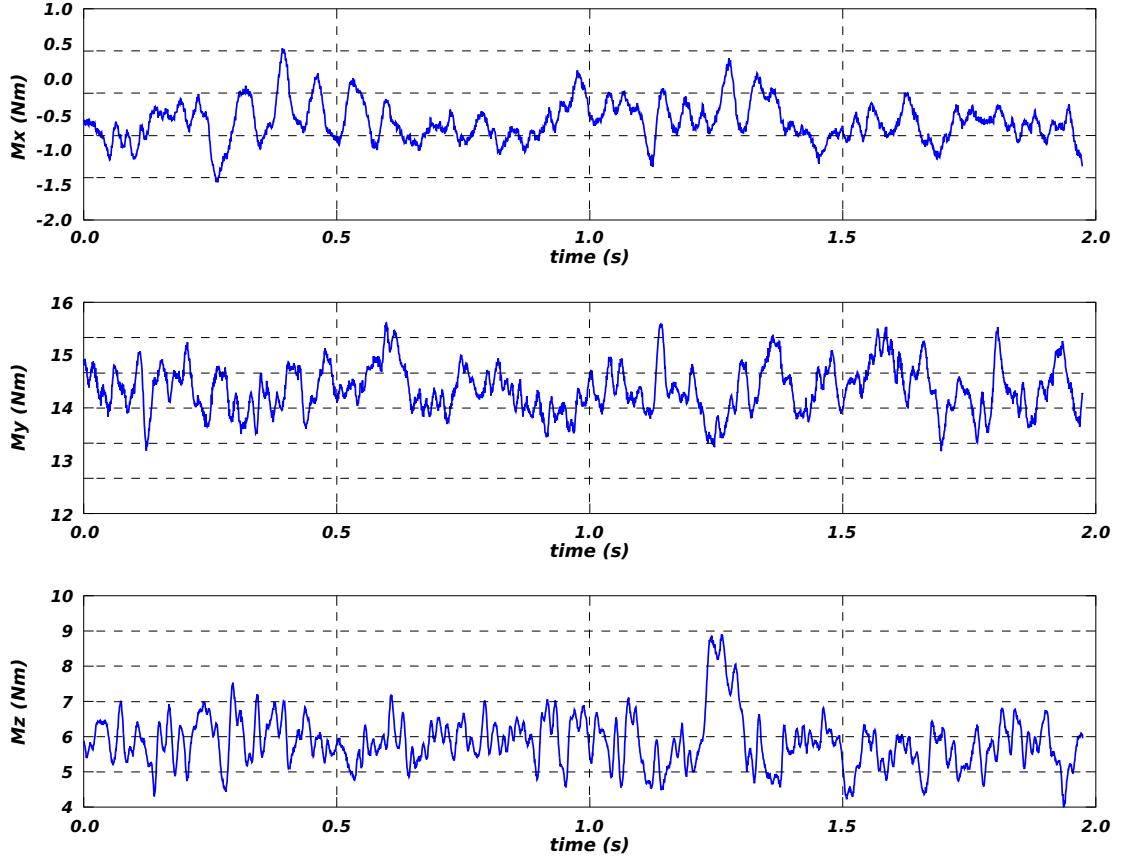
Figure 4.6: Time history of the aerodynamic moments.

is obtained:

$$m\ddot{x} + k_x x + d_x \dot{x} = -F_x(t)$$
$$I_\psi \ddot{\psi} + k_\psi \psi + d_\psi \dot{\psi} = M_z(t)$$

(4.5)

being $I_\psi \equiv I_z$, m the mass of the model (in case equal to its volume), k_x, k_ψ, the bending and torsional stiffnes, respectively, and d_x, d_ψ, the bending and torsional damping, respectively.

Assuming that the system (4.5) is underdamped, that is, $0 < \xi_x = d_x/d_x^c < 1$ and $0 < \xi_\psi = d_\psi/d_\psi^c < 1$, where $d_x^c = 2\sqrt{mk_x}$ and $d_\psi^c = 2\sqrt{I_\psi k_\psi}$ are the critical damping in x-direction and yawing, respectively, and with the initial conditions $x(0) = \psi(0) = 0$ and $\dot{x}(0) = \dot{\psi}(0) = 0$, then its solution is given by:

79
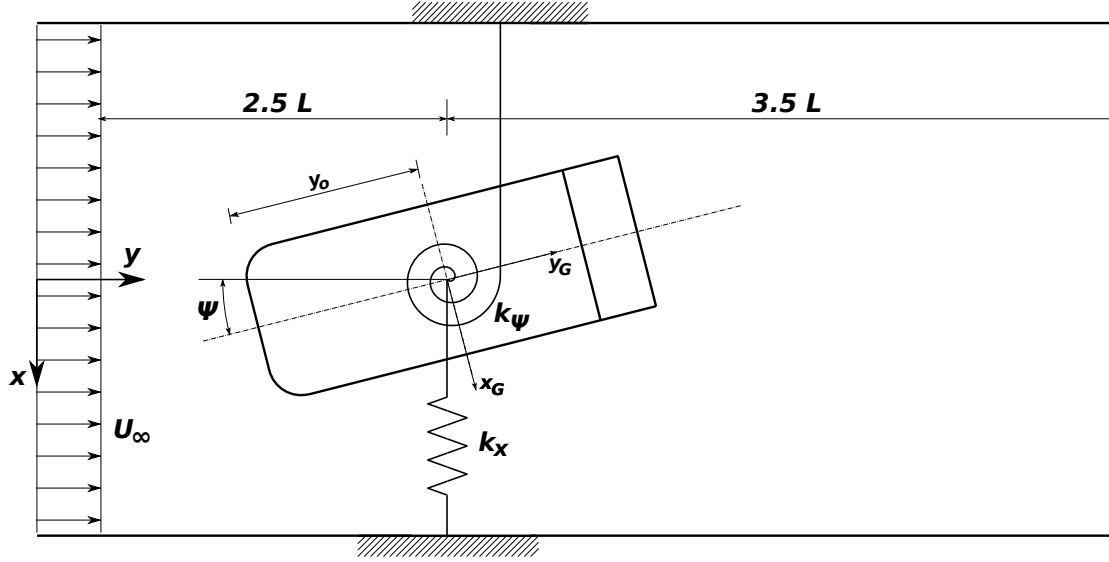
Figure 4.7: Mechanical configuration of the Ahmed body (top view).

Volume (m^3)	Centroid (m)			Inertia (kg m^2)		
	x_o	y_o	z_o	I_x	I_y	I_z
0.1099	0.00	0.52	0.14	0.0098	0.0021	0.0104

Table 4.3: Geometrical data for the Ahmed test case.

$$
\begin{aligned}
x(t) &= e^{-\xi_x \omega_x t} \left[A_1 \cos(\omega_D^x t) + B_1 \sin(\omega_D^x t) \right] + C_1 \cos(\omega_F t) + D_1 \sin(\omega_F t) \\
\psi(t) &= e^{-\xi_\psi \omega_\psi t} \left[A_2 \cos(\omega_D^\psi t) + B_2 \sin(\omega_D^\psi t) \right] + C_2 \cos(\omega_M t) + D_2 \sin(\omega_M t)
\end{aligned}
\tag{4.6}
$$

where

$$
\begin{aligned}
C_1 &= \frac{P_o}{k_x} \frac{-2\xi_x \frac{\omega_F}{\omega_x}}{\left[1 - \left(\frac{\omega_F}{\omega_x}\right)^2\right]^2 + \left[2\xi_x \left(\frac{\omega_F}{\omega_x}\right)^2\right]^2}
& C_2 &= \frac{M_o}{k_\psi} \frac{-2\xi_\psi \left(\frac{\omega_M}{\omega_\psi}\right)^2}{\left[1 - \left(\frac{\omega_M}{\omega_\psi}\right)^2\right]^2 + \left[2\xi_\psi \left(\frac{\omega_M}{\omega_\psi}\right)^2\right]^2} \\[2ex]
D_1 &= \frac{P_o}{k_x} \frac{1 - \left(\frac{\omega_F}{\omega_x}\right)^2}{\left[1 - \left(\frac{\omega_F}{\omega_x}\right)^2\right]^2 + \left[2\xi_x \left(\frac{\omega_F}{\omega_x}\right)^2\right]^2}
& D_2 &= \frac{M_o}{k_\psi} \frac{1 - \left(\frac{\omega_M}{\omega_\psi}\right)^2}{\left[1 - \left(\frac{\omega_M}{\omega_\psi}\right)^2\right]^2 + \left[2\xi_\psi \left(\frac{\omega_M}{\omega_\psi}\right)^2\right]^2}
\end{aligned}
\tag{4.7}
$$

and

$$A_1 = -C_1 \qquad\qquad A_2 = -C_2$$
$$B_1 = \frac{C_1\xi_x\omega_x - D_1\omega_D^x}{\omega_F} \qquad\qquad B_2 = \frac{C_2\xi_\psi\omega_\psi - D_2\omega_D^\psi}{\omega_M} \qquad (4.8)$$

where $\omega_x = \sqrt{k_x/m}$ and $\omega_\psi = \sqrt{k_\psi/I_\psi}$ are the natural frequency of the lateral and yawing oscillation, while $\omega_D^x = \omega_x\sqrt{1-\xi_x^2}$ and $\omega_D^\psi = \omega_\psi\sqrt{1-\xi_\psi^2}$ are the corresponding damped frequency in each degree of freedom. The structural properties used in this test are listed in table (4.4).

P_o (N)	M_o (Nm)	ω_F (rad/s)	ω_M (rad/s)	k_x (N/m)	k_ψ (Nm/rad)	d_x (Ns/m)	d_ψ (Nms/rad)
170	5	50	50	100	6	13.34	1.00

Table 4.4: Structural properties for the Ahmed forced oscillation test case.

The lateral displacement and yaw angle for different times in the simulation are shown in figure (4.8). For the sake of simplicity only 10 time frames are represented here. As it can be seen from figure (4.8), the algorithm in charge of passing the forces and moments to the structure works well for the case of forced oscillation. Also, in figure (4.9) are depicted the different positions of the Ahmed body in correspondence with these times along with isosurfaces of the second invariant of the velocity gradient tensor $Q = 2 \times 10^5$.

Importance of the meshing strategy. As was pointed out before, the computational domain was divided into several regions or "boxes" with different refinement ratio, i.e., the most inner region have the smallest element sizes, which increase in size towards region III, see figure (4.4). In this work, the Computational Mesh Dynamics (`CMD`) problem is solved by relocating the nodes of the mesh. This methodology was preferred to the re-meshing approach, which would introduce an additional computational cost.

The linear elasticity approach is used, where the `CMD` problem is modeled as an elastic medium governed by the linear elasticity equation. The equation governing the displacement of the internal nodes is written as (Stein et al., 2004)
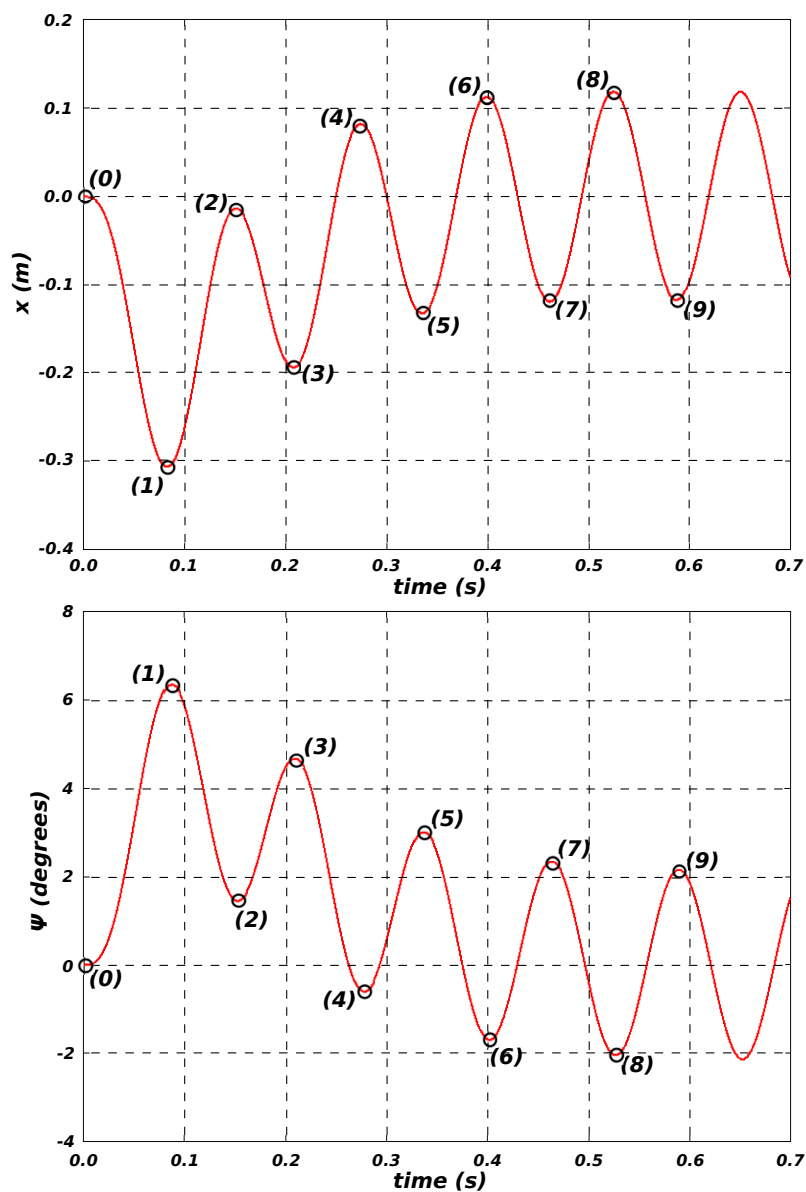
Figure 4.8: Time history of lateral displacement (top) and yaw angle (bottom). Numerical simulation (circles) and analytic solution (red line).

$$\nabla \cdot \overline{\boldsymbol{\sigma}} + \overline{\mathbf{f}} = \mathbf{0} \qquad \text{on } \overline{\Omega} \tag{4.9}$$

being $\overline{\boldsymbol{\sigma}} = \lambda \operatorname{tr}(\boldsymbol{\varepsilon}(\mathbf{y}))\mathbf{I} + 2\mu\boldsymbol{\varepsilon}(\mathbf{y})$ the Cauchy stress tensor, $\overline{\mathbf{f}}$ the external force; $\mathbf{y}$ is the displacement, $\operatorname{tr}()$ the trace operator, λ and μ are the Lamé constants, $\mathbf{I}$ is the identity

(0) t = 0.00 s:

(5) t = 0.34 s:

(1) t = 0.09 s:

(6) t = 0.40 s:

(2) t = 0.15 s:

(7) t = 0.47 s:

(3) t = 0.21 s:

(8) t = 0.53 s

(4) t = 0.28 s:

(9) t = 0.59 s
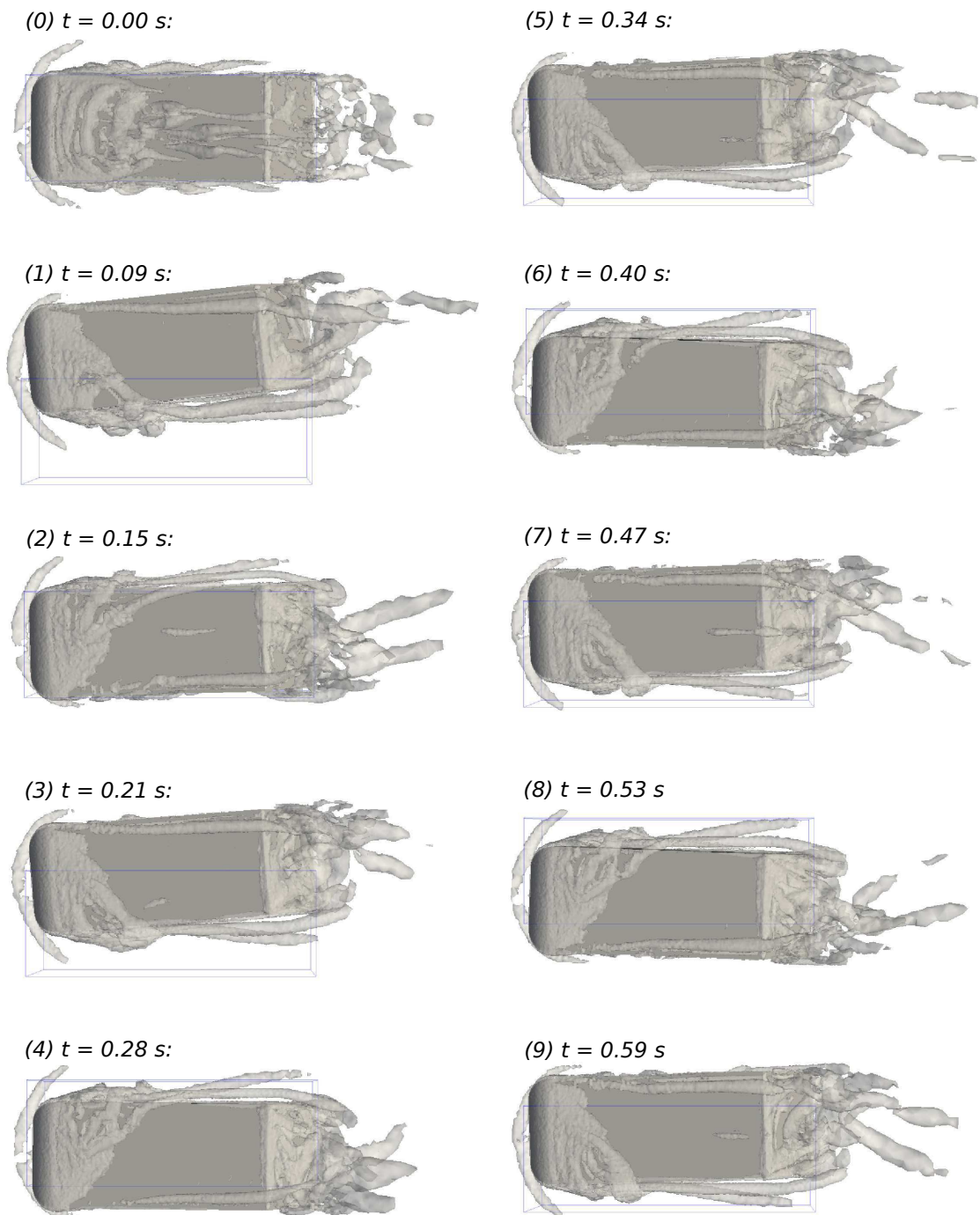
Figure 4.9: Ahmed forced vibration test. Different adopted geometric configuration in time (top view).

tensor and $\boldsymbol{\varepsilon}$ the strain tensor:

$$\varepsilon(\mathbf{y}) = \frac{1}{2}(\nabla\mathbf{y} + (\nabla\mathbf{y})^T) \qquad (4.10)$$

while the boundary conditions are imposed on the fluid-structure interface. By expressing the Lamé constants as a function of the Young's modulus and Poisson ratio, it is possible to avoid severe mesh distortions in critical regions (those elements near the body on region I, for example) with different combinations of parameters. All the tests in this chapter were performed with a ratio $E_I/E_{II} = 50$ and $E_{II}/E_{III} = 10$ between Young's modulus.

4.1.6   Full fluid-structure coupling

There are, to the best author's knowledge, no numerical or experimental FSI studies of simplified road vehicle models. All investigations so far were focused on the forced oscillation of simplified models (Krajnovic et al., 2011; Cheng et al., 2011, 2012; Gilliéron et al., 2003) but none with a full coupling between the fluid and the structure. Therefore, some numerical experiments were performed in order to analyze this phenomenon.

Two simulations with the following parameters were considered: $m = 0.5495$ kg, $I_\psi = 0.052$ kgm^2, $k_x = 100$ N/m, $k_\psi = 6$ Nm/rad, $\rho = 5$ kg/m^3 and were carried out with and without inlet synthesized turbulence. The particular parameters of each simulation are listed in table (4.5).

	Turbulence synthesis	d_x (Ns/m)	d_ψ (Nms/rad)
test I-a	no	13.343	1.005
test I-b	yes	13.343	1.005

Table 4.5: Structural properties for the Ahmed FSI test case.

In figures (4.10) and (4.11) the lateral and angular displacements of the Ahmed body are shown. For test I-a the minimum/maximum values are -0.05 m/0.23 m (lateral displacement) and $-15°/28°$ (yawing), while for test I-b are -0.16 m/0.23 (lateral displacement) and $-25°/8°$ (yawing). The influence of synthesized turbulence

is evidenced by the vortex structures visualized with Q isosurfaces. Clearly, test I-b presents mode developed structures than test I-a.

These results demonstrate that by using the numerical tools presented in this work it is possible to reproduce an experimental test in a wind tunnel. In particular, it is possible to assess experimental FSI studies by a computational model, reproducing all the mechanical and dynamical characteristics of a road vehicle model along with the turbulent flow that interacts with it.

Figure 4.10: Ahmed FSI test I-a. The red line indicates lateral displacement (top) and yaw angle (bottom). Also, the geometric configuration of the Ahmed body for five different time instants is shown (top view).
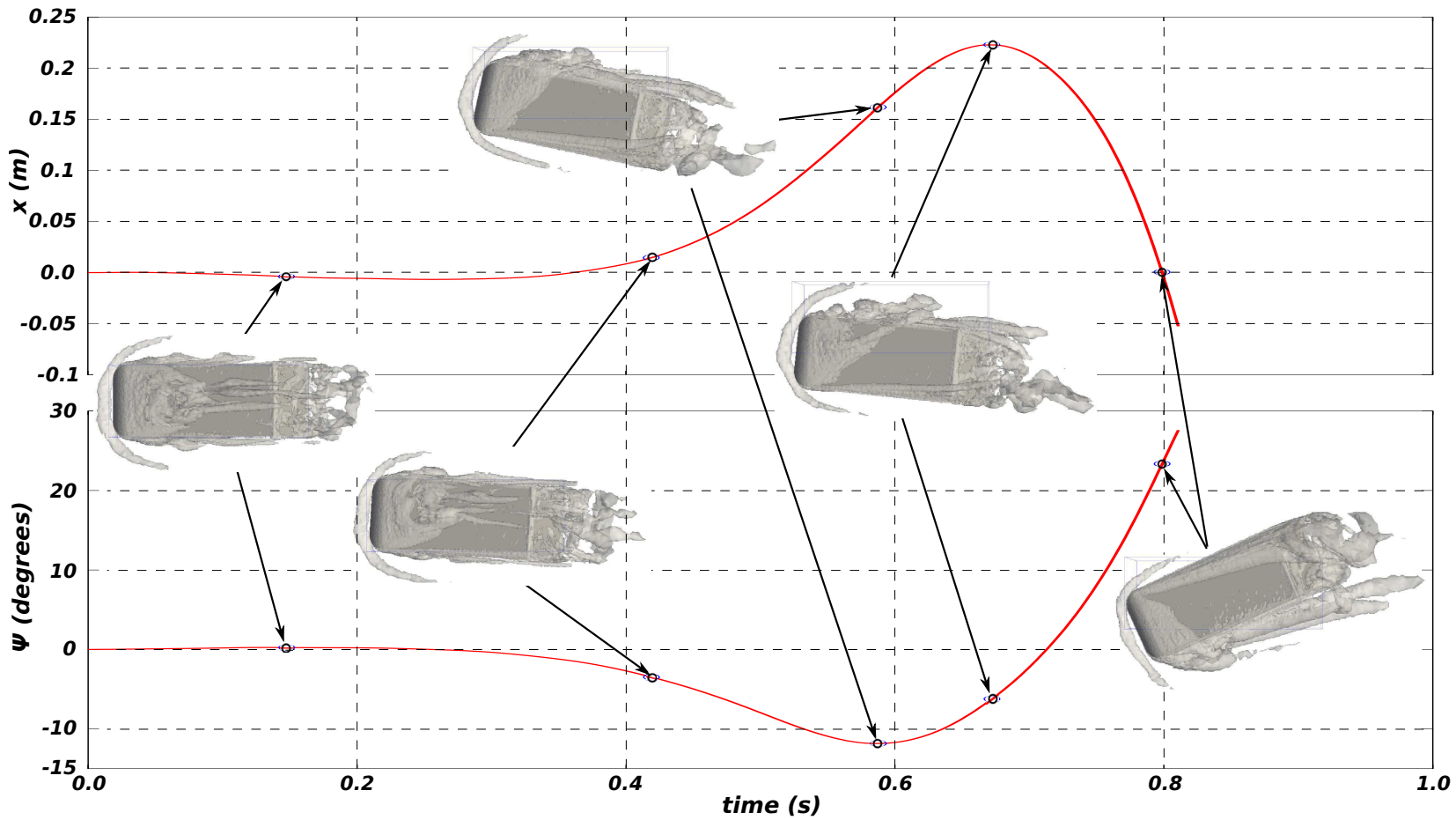
Figure 4.11: Ahmed FSI test I-b. The red line indicates lateral displacement (top) and yaw angle (bottom). Also, the geometric configuration of the Ahmed body for five different time instants is shown (top view).
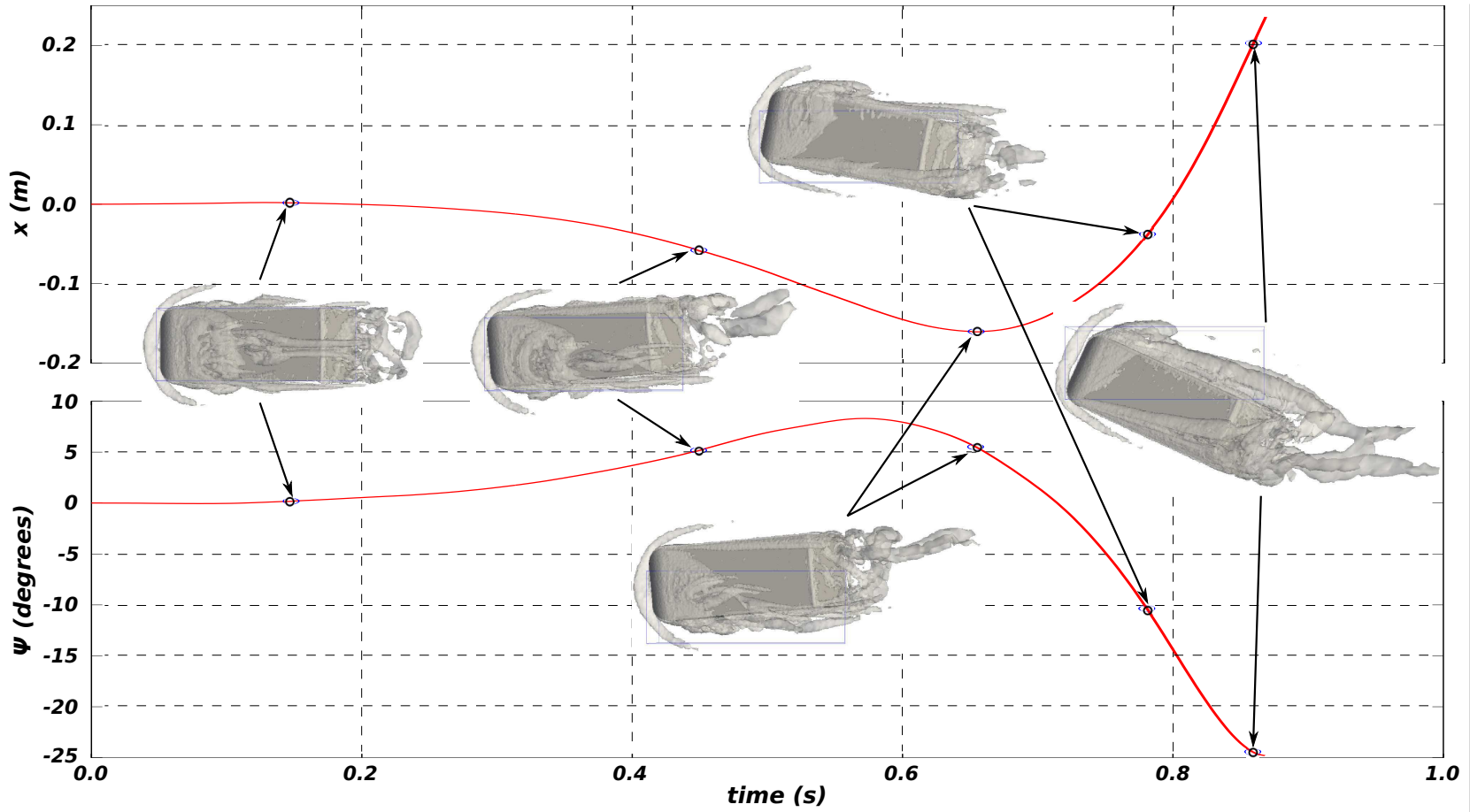
4. APPLICATIONS TO ROAD VEHICLE AERODYNAMICS

Chapter 5

Overview and Final Remarks

The interaction of a fluid with a structure is an important phenomenom that has to be considered in many engineering applications. Particularly, the interaction between a dynamic vehicle model and the airflow is an aspect of the automotive aerodynamics that is poorly investigated. In this thesis the study of the aerodynamic characteristics of a simplified road vehicle model under the action of a turbulent air flow was performed with the aim of simulating a wind tunnel test. As a main contribution of this work, a synthesized turbulence methodology called MDSRFG was proposed, tested and validated. The problem of generating synthesized turbulence at inflow boundaries of the simulation domain was addressed in the context of the LES method. To represent adequately certain statistical properties of a turbulent process, the proposed methodology is based on previous works (Huang et al., 2010; Smirnov et al., 2001). Time and space correlations were strictly introduced in the mathematical formulation of the synthetic turbulence generator. It was demonstrated that the proposed approach inherits the properties of the methods on which it is based while presents some particular advantages as well.

Furthermore, for the analysis of road vehicle aerodynamics, a simplified model known as the Ahmed body was studied under two different scenarios: considering the model as a rigid one and by assigning it dynamic properties. By comparing the numerical simulations with and without generated turbulence it has been shown that the inclusion of unsteady components of velocity leads to a more realistic representation of the physical phenomenon. The fluid-structure interaction model was tested and the

results demonstrated that the computational tools developed in this work enable us to reproduce and/or assist experimental studies.

5.1 Publications

During the work on this thesis the following articles have been published in refereed journals:

1) **Hugo G. Castro, Rodrigo R. Paz** "A time and space correlated turbulence synthesis method for Large Eddy Simulations". Journal of Computational Physics 235, pp. 742-763. ISSN: 0021-9991. (2013).

2) **Rodrigo R. Paz, Mario A. Storti, Lisandro D. Dalcin, Hugo G. Castro, Pablo A. Kler** "FastMat: A C++ library for multi-index array computations". Advances in Engineering Software 54, pp. 38-48. ISSN: 0965-9978 (2012).

3) **Rodrigo R. Paz, Mario A. Storti, Hugo G. Castro, Lisandro D. Dalcin** "Using Hybrid Parallel Programming Techniques for the Computation, Assembly and Solution Stages in Finite Element Codes". Latin American Applied Research 41, pp. 365-377. ISSN: 0327-0793 (2011).

In addition, the following book chapters has been written:

1) **Castro, H.G.; Adotti, M.I.; Paz, R.R.; De Bortoli, M.E.**; "Estudio de la interacción fluido-estructura en tableros de puentes", *La UTN en el NEA. Investigación y Desarrollo en la Facultad Regional Resistencia*, edUTecNe. ISBN: 978-987-27897-0-1 (2012).

2) **Luciano Garelli, Rodrigo R. Paz, Hugo G. Castro, Mario A. Storti, Lisandro D. Dalcin** "Fluid Structure Interaction and Galilean Invariance". *in Computational Fluid Dynamics: Theory, Analysis and Applications*, Alyssa D. Murphy (edts.), pp. 511-550. Nova Science Publishers. ISBN: 978-1-61209-276-8 (2011).

Also, the following works have been presented in conferences on different topics related with this thesis:

1) **Castro, H.G.; Paz, R.R.**; "A modified turbulence synthesis method for Large Eddy Simulations", 10th World Congress on Computational Mechanics, San Pablo, Brasil. (07/2012).

2) **Castro, H.G.; Burguener, H.; Paz, R.R.; De Bortoli, M.E.**; "Desarrollo de una interfaz gráfica para un código abierto de elementos finitos", II Jornadas de Investigación en Ingeniería del NEA y Países Limítrofes. ISBN: 978-950-42-0142-7. UTN Facultad Regional Resistencia, Chaco, Argentina (2012).

3) **Castro, H.G.; Paz, R.R.; Sonzogni, V.**; "Synthezised turbulence with time and space correlation for Large Eddy Simulations", XXX Congreso sobre Métodos Numéricos y sus Aplicaciones, Rosario, Sante Fe, Argentina (2011).

4) **Castro, H.G.; Paz, R.R.; Storti, M.; Sonzogni, V.; Marighetti, J.O.; De Bortoli, M.E.**; "Experimental and numerical study of the aerodynamic behaviour of a simplified road vehicle", Mecom - Cilamce 2010, Buenos Aires, Argentina (2010).

5) **Sonzogni, V.; Castro, H.G.; Paz, R. R.; Balbastro, G.; Storti, M.** "Uso de computación de alto desempeño en ingeniería", XXXIV Jornadas Sud-Americanas de Ingeniería Estructural, San Juan, Argentina (2010).

6) **Sonzogni, V.; Castro, H.; Paz, R.; Balbastro, G.; Storti, M.**; "Experiencias en el cálculo paralelo en el CIMEC", Primer Congreso sobre los métodos numéricos en la enseñanza, la ingeniería y las ciencias - EMNUS 2010, Agosto de 2010, UTN, Facultad Regional Haedo, Argentina.

7) **Castro, H.G.; Paz, R.R.; Storti, M.; Sonzogni, V.; Dalcin, L.**; "Hybrid Parallel Programming Technique on a Finite Element Code", II MACI, diciembre de 2009, Rosario, Santa Fe, Argentina.

8) **Castro, H.G.; Paz, R.R.; Storti, M.; Sonzogni, V.; Dalcin, L.**; "Parallel Implementation of a FEM Code by Using MPI/PETSc and OpenMP Hybrid Programming Techniques", XVII Congreso sobre Métodos Numéricos y sus Aplicaciones, noviembre de 2009, Tandil, Argentina.

9) **Storti, Mario A.; Castro, Hugo G.; Paz, Rodrigo R.; Dalcin, Lisandro D.**; "The FastMat2 Matrix Library. Description and Parallel Implementation". XVII Congreso sobre Métodos Numéricos y sus Aplicaciones, noviembre de 2009, Tandil, Argentina.

Appendix A

Appendix A

A.1 Visualization techniques

Once the results from CFD computations are obtained, the next step is to visualize the flow properties in order to understand the flow structure and individualize certain critical regions. Being the flow field three-dimensional, the velocity has three components in the Cartesian space:

$$
\boldsymbol{u} = \begin{bmatrix} dx/dt \\ dy/dt \\ dz/dt \end{bmatrix} = \begin{bmatrix} u \\ v \\ w \end{bmatrix}
\tag{A.1}
$$

The velocity field gradient, $\nabla \boldsymbol{u}$, allow us to describe more accurately the flow topology. This 3×3 tensor contains the information on how the velocity is changing in space,

$$
\nabla \boldsymbol{u} = A_{ij} = \frac{\partial u_i}{\partial x_j} = \begin{bmatrix} \frac{\partial u}{\partial x} & \frac{\partial u}{\partial y} & \frac{\partial u}{\partial z} \\ \frac{\partial v}{\partial x} & \frac{\partial v}{\partial y} & \frac{\partial v}{\partial z} \\ \frac{\partial w}{\partial x} & \frac{\partial w}{\partial y} & \frac{\partial w}{\partial z} \end{bmatrix}
\tag{A.2}
$$

A_{ij} has units of $time^{-1}$, therefore data deriving from it has the form of a rate.

A. APPENDIX A

An usual form to work with A_{ij} is to decompose it to its symmetric and antisymmetric parts:

$$\frac{\partial u_i}{\partial x_j} = \frac{1}{2}\left(\underbrace{\frac{\partial u_i}{\partial x_j} + \frac{\partial u_i}{\partial x_j}}_{= 2\frac{\partial u_i}{\partial x_j}} + \underbrace{\frac{\partial u_j}{\partial x_i} - \frac{\partial u_j}{\partial x_i}}_{= 0}\right) \tag{A.3}$$

$$= \frac{1}{2}\left(\frac{\partial u_i}{\partial x_j} + \frac{\partial u_j}{\partial x_i}\right) + \frac{1}{2}\left(\frac{\partial u_i}{\partial x_j} - \frac{\partial u_j}{\partial x_i}\right) = S_{ij} + \Omega_{ij}$$

$$\mathbf{S} = \frac{1}{2}(\nabla \boldsymbol{u} + \nabla \boldsymbol{u}^T)$$

$$\boldsymbol{\Omega} = \frac{1}{2}(\nabla \boldsymbol{u} - \nabla \boldsymbol{u}^T) = \frac{1}{2}\begin{bmatrix} 0 & -\omega_z & \omega_y \\ \omega_z & 0 & -\omega_x \\ -\omega_y & \omega_x & 0 \end{bmatrix} \tag{A.4}$$

where S_{ij} is a symmetric tensor called the strain-rate tensor and Ω_{ij} is an antisymmetric tensor called the vorticity tensor. Vorticity is often represented as a vector given that the vorticity tensor has six nonzero values from which only three are independent:

$$\omega_i = \epsilon_{ijk}\frac{\partial u_k}{\partial x_j} \tag{A.5}$$

and the trace of S_{ij} which equals the trace of $\nabla \mathbf{u}$ and represents the divergence of the field is:

$$\nabla \cdot \boldsymbol{u} = \frac{\partial u}{\partial x} + \frac{\partial v}{\partial y} + \frac{\partial w}{\partial z} = \delta_{ij}\frac{\partial u_i}{\partial x_j} \tag{A.6}$$

Critical point theory. Critical points or stationary points are points where the streamline slope is indeterminant and the velocity is zero relative to an observer. The properties of the streamline field or velocity field seen by an observer depends on the velocity of the observer.

Let us consider a non-rotating frame of reference attached to a given particle in the flow. The geometry of the instantaneous streamlines in the neighborhood of any

point in the flow, as seen by an observer moving with the local speed of the fluid, can be described according to the nature of the eigenvalues, and associated eigenvectors, of the velocity gradient tensor at that point (Chong et al., 1990). In such conditions, there will be a critical point located at the particle, and the velocity field u_i in the region immediately surrounding the particle and observer can be described (to a first order approximation) as

$$u_i = A_{ij}\ x_j \tag{A.7}$$

where u_i is the velocity at the position x_j relative to the particle and observer.

The eigenvalues of the velocity gradient tensor which satisfy $\det(A - \lambda I) = 0$ are the roots of the characteristic equation of A_{ij}:

$$\lambda^3 + P\lambda^2 + Q\lambda + R = 0 \tag{A.8}$$

being P, Q and R the tensor invariants,

$$\begin{aligned}
P &= -\text{trace}(\nabla\boldsymbol{u}) = -A_{ii} = -\delta_{ij}\frac{\partial u_i}{\partial x_j} \tag{A.9}\\
Q &= \frac{1}{2}\{[\text{trace}(\nabla\boldsymbol{u})]^2 - \text{trace}[(\nabla\boldsymbol{u})^2]\} = \frac{1}{2}(A_{ii}^2 - A_{ij}A_{ji})\\
&= \frac{1}{2}(P^2 - S_{ij}S_{ji} - \Omega_{ij}\Omega_{ji}) \tag{A.10}\\
R &= -\det(\nabla\boldsymbol{u}) = \frac{1}{3}(-P^3 + 3PQ - S_{ij}S_{jk}S_{ki} - 3\Omega_{ij}\Omega_{jk}S_{ki}) \tag{A.11}
\end{aligned}$$

where *det* indicates the determinant of the tensor. P, Q and R remain the same under arbitrary rotations and translations of the coordinate system. The first invariant P is zero for incompressible flow and hence equation (A.8) reduces to

$$\lambda^3 + Q\lambda + R = 0 \tag{A.12}$$

A. APPENDIX A

It can be shown that the curve that separates the region of real roots from the region were two roots are complex and one is real (in the $Q - R$ plane) is given by the zero value of the discriminant D of A_{ij}:

$$D = \frac{27}{4}R^2 + Q^3 \tag{A.13}$$

The invariants Q and R along with equation (A.13) summarizes the basic topological information of the flow. For example, points in the flow where $D > 0$ are called *foci* and for these points equation (A.12) admits two complex and one real root. For $D < 0$ the points are called *node-saddle-saddle* and all roots of equation (A.12) are real.

All componentes of A_{ij} can be computed for every node in the computational mesh and the invariants Q and R obtained by means of equations (A.9)-(A.11). These values can be used to describe the geometry of the streamline with respect to their position in the $Q - R$ plane.

A.1.1 The Q-criterion

Coherent vortices are regions which have a vorticity concentration strong enough to induce a local roll-up of the flow and keep a characteristic shape during a time T_c large enough with respect to the local turnover time (Lesieur, 2008). Isosurfaces of high vorticity modulus, or vorticity componentes, or low pressure are usually employed to capture these structures. Nevertheles, the so called Q criterion have demostrated to be a very efficient method to such a purpose.

Follow the equation (A.10), the second invariant Q for an incompressible flow can be written as

$$Q = \frac{1}{2}(\Omega_{ij}\Omega_{ij} - S_{ij}S_{ij}) \tag{A.14}$$

where consideration was made of the symmetric and antisymmetric characteristics of the tensors S_{ij} and Ω_{ij}. The first term on the *rhs* of equation (A.14) is proportional to the total *enstrophy* while the second is proportional to the *kinetic energy dissipation*

rate. Thus, isosurfaces with $Q > 0$ show regions where rotation rates are bigger than the strain ones, so they can develop coherent structures, enable us to detect vortex structures accurately.
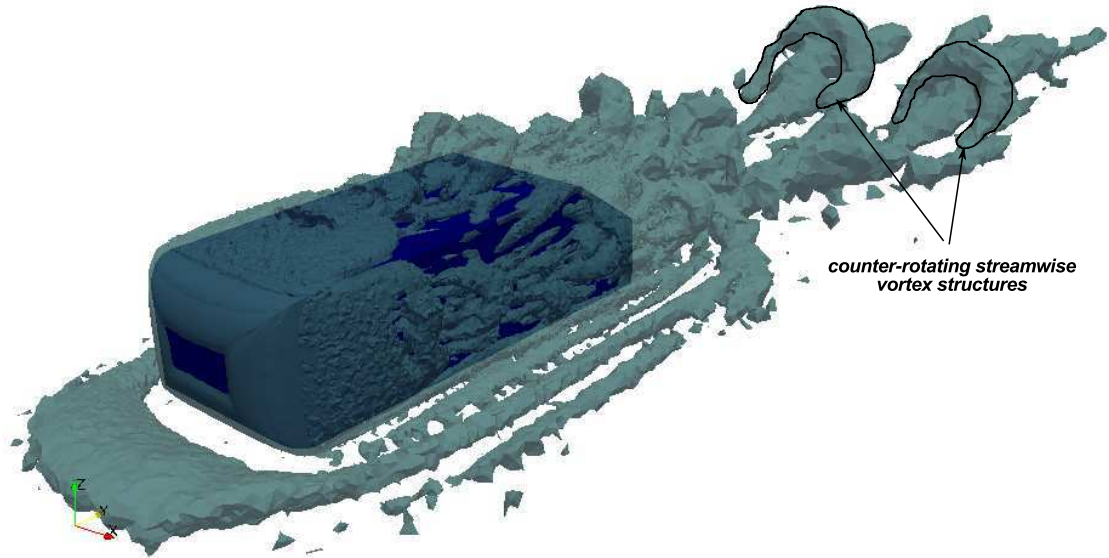
(a) Instantaneous isosurface of Q.
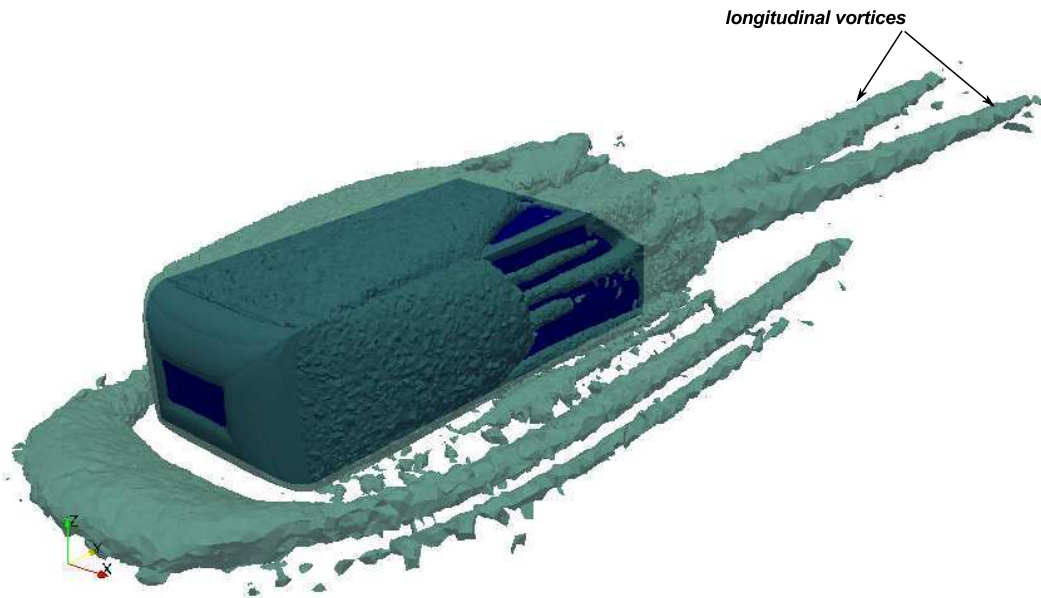
(b) Mean isosurface of Q

Figure A.1: Q criterion around the Ahmed body.

Figures (A.1(a)) and (A.1(b)) shows the vortex structure following the Q criterion

97

A. APPENDIX A

at the level $800\,\mathrm{sec}^{-2}$. Figure (A.1(a)) is a snapshot of the instantaneous vortex system while figure (A.1(b)) shows the time average isosurface of Q.

Appendix B

Resumen extendido en castellano

Generación de turbulencia de entrada para simulación de grandes escalas: aplicaciones a problemas de interacción fluido-estructura.

B.1   Introducción

La aerodinámica estudia el movimiento de un cuerpo sólido en un flujo de aire y la interacción de la superficie del mismo con el fluido que lo rodea, con diferentes velocidades relativas y direcciones. La aerodinámica de vehículos de carretera introduce otra fuente de complejidad debido a la existencia de la capa límite atmosférica (ABL, por *atmospheric boundary layer*). El viento en la ABL genera un entorno de flujo turbulento, que impacta sobre la velocidad media experimentada por el vehículo en su movimiento. Además, esta turbulencia junto con la estela provocada por el vehículo pueden afectar las fuerzas aerodinámicas transientes que actúan sobre el mismo. Si la frecuencia de estas fuerzas coincide con la frecuencia natural del cuerpo, pueden provocar ruido y vibraciones que pueden afectar seriamente el confort del conductor y ocupantes del vehículo. La complejidad asociada con flujos transientes ocasiona que gran parte de las investigaciones estén limitadas al comportamiento del vehículo bajo la acción del flujo medio.

La Dinámica de Fluidos Computacional (CFD, por *Computational Fluid Dynamics*) permite realizar estudios sobre la aerodinámica de vehículos de carretera mediante la simulación numérica de las ecuaciones de gobierno del sistema físico. La gran amplitud de escalas de longitud y tiempo presentes en los problemas anteriormente mencionados precisa de un alto grado de refinamiento en las mallas de elementos finitos (o de volúmenes finitos), lo cual se traduce en el requerimiento de grandes recursos computacionales. Nuevas tecnologías y computadoras cada vez más rápidas y potentes posibilitan hoy en día resolver numéricamente este tipo de problemas complejos.

En el estudio de la aerodinámica vehicular a menudo se asume que el vehículo es un cuerpo rígido, es decir, que su frecuencia natural es varias veces superior a la frecuencia de las ráfagas más energéticas presentes en el flujo. Sin embargo, esto no es así para el caso de los vehículos reales en carretera. Estos interactúan con el viento incidente, el cual cambia de intensidad y dirección de manera impredecible y además con los golpes e imperfecciones en la superficie del camino. La interacción entre el viento y el vehículo puede modelarse numéricamente como un problema de interacción fluido-estructura (FSI, por *fluid-structure interaction*) mientras que las imperfecciones del camino como una fuerza estocástica sobre el sistema.

En los problemas de FSI la dinámica del fluido y la estructura se influencian mutuamente: la estructura se deforma bajo el efecto de las fuerzas provocadas por el fluido y el fluido acompaña los desplazamientos de la estructura. Esta interacción no sólo implica que la velocidad del fluido iguala a la de la estructura en la interfase sino que el dominio cambia como consecuencia del movimiento de la estructura.

Incluso en la actualidad, con los grandes incrementos logrados en la potencia de cálculo de las computadoras, la simulación experimental es optada por sobre la numérica en el estudio de la aerodinámica vehicular e incluso en el análisis de problemas de FSI dada la confiabilidad adquirida por los túneles de viento.

El propósito de este trabajo de tesis es el de investigar la factibilidad del uso de un código computacional para reproducir las condiciones experimentales presentes en un túnel de viento. Este estudio está centrado no sólo en la aerodinámica de un cuerpo fijo sino que además en su interacción dinámica con el flujo de viento incidente.

El objetivo global es el de demostrar que los códigos computacionales desarrollados en este trabajo pueden utilizarse no para reemplazar los ensayos en túnel de viento

sino como herramientas complementarias. Esta observación está basada en el hecho de que un túnel de viento permite la *medición* y no la *estimación* de las fuerzas aerodinaámicas, siempre que la física del flujo sea correctamente representada. Además, el túnel de viento ha demostrado una notable correlación con los ensayos sobre prototipos en carretera y es una herramienta rápida, rentable y confiable (Cooper, 2004). Por otro lado, mediante la CFD es posible realizar las siguientes tareas:

- desarrollar un análisis detallado del problema, aislando cualquier aspecto de la geometría del cuerpo si es preciso,

- ampliar la comprensión de la física del problema, mediante la utilización de potentes herramientas de visualización,

- modificar las condiciones del ensayo de manera eficiente.

Todas estas características sugieren que, si es utilizada complementariamente con estudios experimentales, acelerarían el ciclo de desarrollo de vehículos de carretera.

B.2 Ecuaciones de Navier-Stokes para flujo incompresible

Un número de importantes fenómenos en la mecánica de fluidos son representados adecuadamente mediante las ecuaciones de Navier-Stokes. Estas ecuaciones describen el efecto dinámico de las fuerzas externamente aplicadas y las fuerzas internas de un fluido, el cual, a lo largo de este trabajo, será asumido como newtoniano.

Consideremos una región del flujo acotada $\Omega \in \mathbb{R}^{n_{sd}}$, donde n_{sd} es el número de dimensiones espaciales y un dominio en el tiempo $(0, t_+]$. El contorno $\Gamma = \partial\Omega$ se asume Lipschitz continuo (una superficie cerrada y lo suficientemente regular). Luego, la versión para flujo incompresible de estas ecuaciones es

$$\rho\left(\frac{\partial \boldsymbol{u}}{\partial t} + \boldsymbol{u} \cdot \nabla \boldsymbol{u}\right) - \nabla \cdot \boldsymbol{\sigma} - \rho \mathbf{g} = \mathbf{0} \qquad \text{en } \Omega \times (0, t_+] \tag{B.1}$$

$$\nabla \cdot \boldsymbol{u} = 0 \qquad \text{en } \Omega \times (0, t_+], \tag{B.2}$$

La ecuación (B.1) representa la conservación de cantidad de movimiento para fluidos newtonianos, con densidad ρ y viscosidad dinámica μ, bajo la acción de un campo gravitacional de aceleración $\mathbf{g}$. Además, $\boldsymbol{\sigma} = -p\mathbf{I} + \mu(\nabla\boldsymbol{u} + \nabla\boldsymbol{u}^T)$ es el tensor de tensiones debido a la presión p y las fuerzas viscosas mientras que $\mathbf{I}$ representa el tensor identidad. La ecuación (B.2) expresa la conservación de masa en fluidos incompresibles.

Las condiciones de contorno e iniciales son

$$
\begin{aligned}
\boldsymbol{u} &= \boldsymbol{u}_D & &\text{sobre } \Gamma_D \\
\mathbf{n} \cdot \boldsymbol{\sigma} &= \mathbf{h} & &\text{sobre } \Gamma_N \\
\boldsymbol{u}(t=0) &= \boldsymbol{u}_0 & &\forall \boldsymbol{x} \in \Omega_0 \\
p(t=0) &= p_0 & &\forall \boldsymbol{x} \in \Omega_0
\end{aligned}
\tag{B.3}
$$

donde Γ_D y Γ_N son los contornos Dirichlet y Neumann, respectivamente, tales que

$$
\begin{aligned}
\Gamma_D \cup \Gamma_N &= \Gamma \\
\Gamma_D \cap \Gamma_N &= \emptyset
\end{aligned}
\tag{B.4}
$$

B.3 Un método modificado para sintetizar turbulencia como condición de entrada

Huang et al. (2010) propusieron un método de síntesis de turbulencia denominado "generación de flujo aleatorio mediante discretización y síntesis" (DSRFG, por *discretizing and synthesizing random flow generation*) para la implementación de condiciones de turbulencia en el ingreso de dominios en LES. Este método demostró poseer varias ventajas sobre su predecesor, el método de generación de flujo aleatorio (RFG, por *random flow generation*) de Smirnov et al. (2001). No obstante, es posible demostrar que mediante un nuevo análisis de las ecuaciones DSRFG es posible realizar algunas mejoras al método. De acuerdo a esto, una breve descripción del método DSRFG es realizada en esta sección junto con la introducción de las modificaciones propuestas. Para una más detallada discusión acerca de los métodos RFG y DSRFG se recomienda al lector referirse a los artículos originales (Smirnov et al., 2001; Huang et al., 2010).

B.3 Un método modificado para sintetizar turbulencia como condición de entrada

Siguiendo el desarrollo del método DSRFG, un campo de flujo turbulento, homogéneo e isotrópico, $\boldsymbol{u}(\boldsymbol{x}, t)$, puede sintetizarse de la siguiente manera:

$$u_i(\boldsymbol{x}, t) = \sum_{m=1}^{M} \sum_{n=1}^{N} \left[p_i^{m,n} \cos(\tilde{k}_j^{m,n} \tilde{x}_j + \omega_{m,n} t) + q_i^{m,n} \sin(\tilde{k}_j^{m,n} \tilde{x}_j + \omega_{m,n} t) \right], \qquad (B.5)$$

donde

$$\mathbf{p}^{m,n} = \frac{\boldsymbol{\zeta} \times \mathbf{k}^{m,n}}{|\boldsymbol{\zeta} \times \mathbf{k}^{m,n}|} \sqrt{a \frac{4E(k_m)}{N}}, \qquad (B.6)$$

$$\mathbf{q}^{m,n} = \frac{\boldsymbol{\xi} \times \mathbf{k}^{m,n}}{|\boldsymbol{\xi} \times \mathbf{k}^{m,n}|} \sqrt{(1-a) \frac{4E(k_m)}{N}}, \qquad (B.7)$$

$$\tilde{\mathbf{x}} = \frac{\mathbf{x}}{L_s}, \qquad (B.8)$$

$$\tilde{\mathbf{k}}^{m,n} = \frac{\mathbf{k}^{m,n}}{k_0}, \qquad (B.9)$$

con $\omega_{m,n} \in N(0, 2\pi f_m)$, $f_m = k_m U_{\text{avg}}$, a es un número aleatorio uniformemente distribuido entre 0 y 1, $\boldsymbol{\zeta}$ y $\boldsymbol{\xi}$ son la forma vectorial de ζ_i^n y ξ_i^n, los cuales son números aleatorios seleccionados independientemente de $N(0,1)$. Aquí, $N(\mu, \sigma)$ representa una distribución Normal con media μ y desvío estándar σ. En las ecuaciones (B.8) y (B.9) L_s es un factor de escala relacionado con la escala de longitud de la turbulencia y k_0 es el número de onda más bajo del espectro discreto.

Los factores $p_i^{m,n}$ y $q_i^{m,n}$ definen la distribución del espectro de energía tridimensional $E(k_m)$ en cada uno de los ejes de coordenadas espaciales, los cuales a su vez son funciones del número de onda espacial $\mathbf{k}^{m,n}$ ($|\mathbf{k}^{m,n}| = k_m$) y de los vectores aleatorios normales $\boldsymbol{\zeta}$ y $\boldsymbol{\xi}$.

Cuando se trata con turbulencia homogénea e isotrópica, la distribución de $\mathbf{k}^{m,n}$ es isotrópica sobre la superficie de una esfera y en consecuencia la energía es uniformemente distribuida en el espacio. En tales condiciones es evidente que el mismo espectro será obtenido en las tres direcciones principales pero en el caso de turbulen-

cia heterogénea y anisotrópica la distribución de $\mathbf{k}^{m,n}$ debe cambiar de acuerdo a las condiciones de heterogeneidad y anisotropía.

Para lograr este comportamiento, $p_i^{m,n}$ y $q_i^{m,n}$ deben *alinearse* con el espectro de energía con respecto a una dirección principal y luego la distribución de $\mathbf{k}^{m,n}$ puede ser nuevamente *mapeada* sobre la superficie de la esfera. En resumen, el método es implementado utilizando la ecuación (B.5) y

$$p_i^{m,n} = \text{sign}(r_i^{m,n}) \sqrt{\frac{4}{N} E_i(k_m) \frac{(r_i^{m,n})^2}{1 + (r_i^{m,n})^2}}, \tag{B.10}$$

$$q_i^{m,n} = \text{sign}(r_i^{m,n}) \sqrt{\frac{4}{N} E_i(k_m) \frac{1}{1 + (r_i^{m,n})^2}}, \tag{B.11}$$

$$\mathbf{k}^{m,n} \cdot \mathbf{p}^{m,n} = 0, \tag{B.12}$$

$$\mathbf{k}^{m,n} \cdot \mathbf{q}^{m,n} = 0, \tag{B.13}$$

$$|\mathbf{k}^{m,n}| = k_m, \tag{B.14}$$

donde $r_i^{m,n}$ es un número aleatorio, independientemente seleccionado de una distribución Normal tridimensional con $\mu_r = 0$ y $\sigma_r = 1$.

En base a esta formulación, es posible demostrar que

$$
\begin{aligned}
\overline{u_i u_i} &= \frac{1}{2} \sum_{m=1}^{M} \sum_{n=1}^{N} p_i^{m,n} p_i^{m,n} + \frac{1}{2} \sum_{m=1}^{M} \sum_{n=1}^{N} q_i^{m,n} q_i^{m,n} \\
&= 2 \int_0^\infty E(k)dk \ \approx \ 2 \sum_{m=1}^{M} E(k_m) \Delta k_m,
\end{aligned}
\tag{B.15}
$$

o bien

$$
\begin{aligned}
\overline{u_i u_i} &= \frac{1}{2} \sum_{m=1}^{M} \sum_{n=1}^{N} \sum_{i=1}^{3} \Big[\frac{4}{N} E_i(k_m) \frac{(r_i^{m,n})^2}{1+(r_i^{m,n})^2} + \frac{4}{N} E_i(k_m) \frac{1}{1+(r_i^{m,n})^2} \Big] \\
&= \frac{2}{N} \sum_{m=1}^{M} \sum_{n=1}^{N} E(k_m) = 2 \sum_{m=1}^{M} E(k_m),
\end{aligned}
\tag{B.16}
$$

implicando que, dado que $E(k_m)$ es una cantidad positiva para todo k, la energía cinética de las velocidades fluctuantes generadas dependa fuertemente del número de puntos M considerados en la discretización del espectro modelo.

B.3.1   Metodología propuesta

En vista del análisis previo, proponemos algunas modificaciones a las ecuaciones del método DSRFG. Primeramente, la serie de Fourier en la ecuación (B.5) es escrita como:

$$
u_i(\boldsymbol{x}, t) = \sum_{m=1}^{M} \sum_{n=1}^{N} \Big[p_i^{m,n} \cos \Big(\tilde{k}_j^{m,n} \tilde{x}_j + \omega_{m,n} \frac{t}{\tau_0} \Big) + q_i^{m,n} \sin \Big(\tilde{k}_j^{m,n} \tilde{x}_j + \omega_{m,n} \frac{t}{\tau_0} \Big) \Big]. \tag{B.17}
$$

La inclusión de un parámetro que modifica el tiempo t está basado en el trabajo de Smirnov et al. (2001) y Batten et al. (2004) pero con diferente significado físico. Aquí, τ_0 no es la escala de tiempo de la turbulencia sino que es un parámetro adimensional introducido para permitir algún "control" sobre la correlación temporal de la serie de velocidad generada.

Tal como fuera demostrado mediante la ecuación (B.15), la energía del flujo turbulento está relacionada con el espectro de energía tridimensional $E(k_m)$ y los factores $p_i^{m,n}$ y $q_i^{m,n}$. Como indicaran Huang et al. (2010), estos factores alinean el espectro de energía de acuerdo a las condiciones de anisotropía de la turbulencia, propocionando series de velocidad sintetizadas que deben satisfacer los valores cuadrados medios en cada dirección espacial. En base a estas consideraciones y notando que según la ecuación (B.16), la energía cinética no es aproximada mediante una serie convergente, es necesario un análisis alternativo para asegurar que la intensidad de turbulencia sintética

pueda representar adecuadamente el flujo a simularse. En este trabajo se realiza un simple "desacople" de la ecuación (B.15) utilizando la siguiente relación:

$$\sum_{i=1}^{3} u_{\text{rms},i}^2 = 2 \sum_{m=1}^{M} E(k_m)\Delta k_m = 2 \sum_{m=1}^{M} \sum_{i=1}^{3} c_i E_i(k_m)\Delta k_m. \tag{B.18}$$

Esta ecuación implica que el espectro de energía tridimensional $E(k)$ es una suma ponderada de espectros de energía unidimensionales modificados, alineados con las tres direcciones principales.

En la ecuación (B.18), c_i es un valor que depende de la forma del espectro necesario para satisfacer la condición

$$u_{\text{rms},i}^2 = 2c_i \int_0^{\infty} E_i(k)dk, \tag{B.19}$$

es decir, en cada dirección, la variancia de las series de velocidad simuladas deben satisfacer la ecuación (B.19). Luego,

$$\sum_{i=1}^{3} u_{\text{rms},i}^2 = 2 \sum_{i=1}^{3} \int_0^{\infty} c_i E_i(k)\Delta k = 2 \int_0^{\infty} E(k)\Delta k. \tag{B.20}$$

De esta manera, para cada dirección i obtenemos la versión modificada de las ecuaciones (B.10) y (B.11):

$$p_i^{m,n} = \text{sign}(r_i^{m,n})\sqrt{\frac{4c_i}{N} E_i(k_m)\Delta k_m \frac{(r_i^{m,n})^2}{1+(r_i^{m,n})^2}}, \tag{B.21}$$

$$q_i^{m,n} = \text{sign}(r_i^{m,n})\sqrt{\frac{4c_i}{N} E_i(k_m)\Delta k_m \frac{1}{1+(r_i^{m,n})^2}}. \tag{B.22}$$

Con esta formulación, la correlación temporal puede escribirse como

$$\overline{u_i(\boldsymbol{x},t)u_i(\boldsymbol{x},t+\tau)} = \frac{2c_i}{N}\sum_{m=1}^{M}\sum_{n=1}^{N}E_i(k_m)\Delta k_m\cos\left(\frac{\tau}{\tau_0}\omega_{m,n}\right), \qquad (B.23)$$

mientras que la correlación espacial como

$$\overline{u_i(\boldsymbol{x},t)u_i(\boldsymbol{x'},t)} = \frac{2c_i}{N}\sum_{m=1}^{M}\sum_{n=1}^{N}E_i(k_m)\Delta k_m\cos\left[\tilde{k}_j^{m,n}\frac{(x'_j - x_j)}{L_s}\right]. \qquad (B.24)$$

Al igual que en el método DSRFG, el parámetro de escalado espacial L_s es calculado como

$$L_s = \theta_1\ \sqrt{L_u^2 + L_v^2 + L_w^2}, \qquad (B.25)$$

donde θ_1 varía entre 0 y 1, mientras que el parámetro adimensional de correlación temporal τ_0 es un escalar cuyo valor depende del problema analizado. Dado que esta nueva metodología está basada en el método DSRFG, se ha denominado *generación modificada de flujo aleatorio mediante discretización y síntesis* (MDSRFG, por *modified discretizing and synthesizing random flow generation*).

B.4   Forma ALE de las ecuaciones de Navier-Stokes

Con el marco de la formulación ALE presente, es necesario ahora introducir las ecuaciones de conservación de masa y cantidad de movimiento. Para facilitar la presentación, las ecuaciones de Navier-Stokes para flujo incompresible en la configuración Euleriana, ecuaciones (B.1) y (B.2), son nuevamente escritas aquí:

$$\rho\left(\frac{\partial \boldsymbol{u}}{\partial t}\bigg|_{\boldsymbol{x}} + \boldsymbol{u}\cdot\nabla\boldsymbol{u}\right) - \nabla\cdot\boldsymbol{\sigma} - \rho\mathbf{g} = \mathbf{0} \qquad (B.26)$$

$$\nabla\cdot\boldsymbol{u} = 0 \qquad (B.27)$$

Para expresar las ecuaciones de Navier-Stokes en la formulación ALE, sólo es necesario reemplazar la velocidad material $\boldsymbol{u}$ por la velocidad convectiva $\mathbf{c}$ en los términos convectivos:

$$\rho\left(\frac{\partial \boldsymbol{u}}{\partial t}\bigg|_{\boldsymbol{\chi}} + \mathbf{c} \cdot \nabla\boldsymbol{u}\right) - \nabla \cdot \boldsymbol{\sigma} - \rho\mathbf{g} = \mathbf{0} \tag{B.28}$$

$$\nabla \cdot \boldsymbol{u} = 0 \tag{B.29}$$

siendo ahora las condiciones iniciales y de contorno:

$$\begin{aligned}
\boldsymbol{u} &= \boldsymbol{u}_D & &\text{sobre } \Gamma_D \\
\mathbf{n} \cdot \boldsymbol{\sigma} &= \mathbf{t} & &\text{sobre } \Gamma_N, \\
\boldsymbol{u}(t=0) &= \boldsymbol{u}_0 & &\forall \boldsymbol{x} \in \Omega_0 \\
p(t=0) &= p_0 & &\forall \boldsymbol{x} \in \Omega_0 \\
\boldsymbol{u} &= \hat{\boldsymbol{u}} & &\text{sobre } \Gamma_w
\end{aligned} \tag{B.30}$$

donde la última condición está directamente relacionada con la descripción ALE, representando en este caso la suposición de que el fluido se "adhiere" a la estructura (condición de no deslizamiento). Aquí, Γ_w es el contorno de la estructura embebido en el fluido (interfase entre los dominios fluido/estructura).

B.4.1 Simulación particionada de la interacción fluido-estructura

El acoplamiento entre el fluido y la respuesta estructural puede lograrse de diferentes maneras, pero en todos los casos las condiciones de compatibilidad de desplazamientos y el equilibrio de tensiones sobre las interfases fluido/estructura deben satisfacerse (Bathe and Zhang, 2004):

Compatibilidad de desplazamiento:

$$\mathbf{d}_f = \mathbf{d}_s \quad \text{on } \Gamma_w \tag{B.31}$$

Equilibrio de tensiones:

$$\mathbf{f}_f = \mathbf{f}_s \qquad \text{on } \Gamma_w \tag{B.32}$$

donde $\mathbf{d}_f$ y $\mathbf{d}_s$ son los desplazamientos, $\mathbf{f}_f$ y $\mathbf{f}_s$ son las tensiones del fluido y de la estructura, respectivamente. Una descripción general de estas condiciones de compatibilidad, considerando distintas mallas para los dominios del fluido y de la estructura es ilustrada en la figura (B.1).
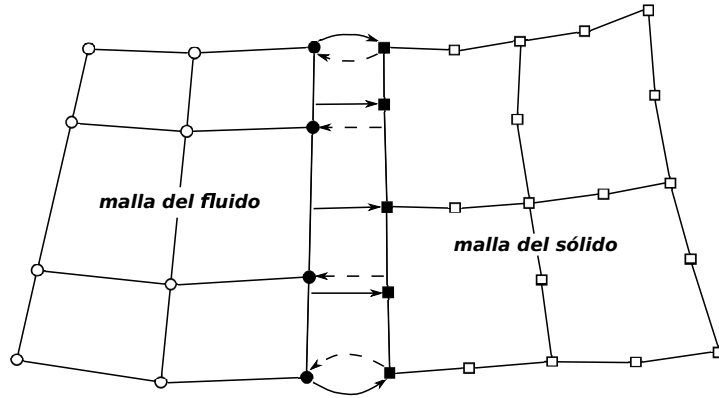

Figure B.1: Mapeos de los desplazamientos y tensiones sobre las interfaces fluido-estructura. Las flechas continuas indican el mapero de tensiones mientras que las flechas a rayas indican el mapeo de desplazamientos (Bathe and Zhang, 2004).

Una manera sencilla de satisfacer la versión discretizada de las ecuaciones (B.31) y (B.32) es resolver los problemas fluido y estructura en el mismo instante, en un único *"solver"*, metodología usualmente conocida como *monolítica*. Un método monolítico es típicamente *fuertemente acoplado*, significando que las ecuaciones (B.31) y (B.32) son satisfechas después de la discretización en el tiempo. Sin embargo, a menudo un esquema monolítico precisa un gran esfuerzo computacional además de ser de muy difícil control a nivel de software (Farhat et al., 1998). Alternativamente, estas ecuaciones pueden resolverse mediante un procedimiento *particionado* (a veces denominado *por etapas* o *segregado*), donde la solución del problema acoplado se avanza sobre los componentes del problema: fluido, estructura y malla dinámica, en forma separada. Luego, tres códigos son necesarios: CMD (por *Computational Mesh Dynamics*), que calcula la dinámica de la malla, CSD (por *Computational Structure Dynamics*) que calcula la dinámica de la estructura, y CFD (por *Computational Fluid Dynamics*) que calcula la dinámica del fluido. Al aplicar esta procedimiento es posible utilizar métodos optimiza-

dos para la discretización y resolución en cada disciplina en particular, preservando la modularidad del código. Entre los esquemas particionados es posible diferenciar entre *débilmente* y *fuertemente* acoplados. Un esquema se denomina *débilmente* (o *explícitamente*) acoplado si las ecuaciones (B.31) and (B.32) no son completamente satisfechas en cada paso de tiempo (las velocidades del fluido y el sólido no coinciden exactamente en la interfase). Sin embargo, si es necesaria mayor exactitud o estabilidad numérica, es posible adicionar iteraciones con predictor/corrector, en cuyo caso el procedimiento particionado se convierte en un algoritmo de resolución fuertemente acoplado (Storti et al., 2009).

B.5 Observaciones finales y conclusiones

La interacción de un fluido con una estructura es un fenómeno importante en muchas aplicaciones de la ingeniería. Particularmente, la interacción entre un modelo dinámico de un vehículo y el flujo de aire es un aspecto de la aerodinámica vehicular que es escasamente investigado. En esta tesis se han estudiado las características aerodinámicas de un modelo simplificado de vehículo de carretera bajo la acción de un flujo de aire turbulento, con el objetivo de simular un ensayo en túnel de viento. Como principal contribución de este trabajo, fue propuesta, probada y validada, una metodología para sintetizar turbulencia, denominada MDSRFG. La generaración de turbulencia sintetizada en el flujo de ingreso a dominios fue abordada en el contexto del método LES. Para representar adecuadamente ciertas propiedades estadísticas de un proceso turbulento, la metodología propuesta está basada en trabajos previos (Huang et al., 2010; Smirnov et al., 2001). Las correlaciones en tiempo y espacio fueron estrictamente introducidas en la formulación matemática del generador de turbulencia sintetizada. Se ha demostrado que el método propuesto hereda las propiedades de los métodos en los cuales se basa, presentando además algunas ventajas particulares.

Además, para el análisis de la aerodinámica de un vehículo de carretera, un modelo simplificado conocido como cuerpo de Ahmed fue estudiado en dos escenarios diferentes: considerando el modelo como rígido por un lado y caracterizándolo con propiedades dinámicas por otro. Comparando las simulaciones numéricas con y sin generación de turbulencia se ha demostrado que la inclusión de las componentes instantáneas de la velocidad conducen a una representación más realista del fenómeno físico. El modelo de interacción fluido-estructura fue probado y los resultados demostraron que

las herramientas computacionales desarrolladas en el marco de esta tesis permite la reproducción y/o la asistencia de estudios experimentales.

B.5.1 Publicaciones

Durante la elaboración de esta tesis, los siguientes artículos han sido publicados en revistas arbitradas:

1) **Hugo G. Castro, Rodrigo R. Paz** "A time and space correlated turbulence synthesis method for Large Eddy Simulations". Journal of Computational Physics 235, pp. 742-763. ISSN: 0021-9991. (2013).

2) **Rodrigo R. Paz, Mario A. Storti, Lisandro D. Dalcin, Hugo G. Castro, Pablo A. Kler** "FastMat: A C++ library for multi-index array computations". Advances in Engineering Software 54, pp. 38-48. ISSN: 0965-9978 (2012).

3) **Rodrigo R. Paz, Mario A. Storti, Hugo G. Castro, Lisandro D. Dalcin** "Using Hybrid Parallel Programming Techniques for the Computation, Assembly and Solution Stages in Finite Element Codes". Latin American Applied Research 41, pp. 365-377. ISSN: 0327-0793 (2011).

Adicionalmente, los siguientes capítulos de libro han sido escritos:

1) **Castro, H.G.; Adotti, M.I.; Paz, R.R.; De Bortoli, M.E.**; "Estudio de la interacción fluido-estructura en tableros de puentes", *La UTN en el NEA. Investigación y Desarrollo en la Facultad Regional Resistencia*, edUTecNe. ISBN: 978-987-27897-0-1 (2012).

2) **Luciano Garelli, Rodrigo R. Paz, Hugo G. Castro, Mario A. Storti, Lisandro D. Dalcin** "Fluid Structure Interaction and Galilean Invariance". *in Computational Fluid Dynamics: Theory, Analysis and Applications*, Alyssa D. Murphy (edts.), pp. 511-550. Nova Science Publishers. ISBN: 978-1-61209-276-8 (2011).

Además, los siguientes trabajos han sido presentados en congresos sobre diferentes tópicos relacionados con esta tesis:

B. RESUMEN EXTENDIDO EN CASTELLANO

1) **Castro, H.G.; Paz, R.R.**; "A modified turbulence synthesis method for Large Eddy Simulations", 10th World Congress on Computational Mechanics, San Pablo, Brasil. (07/2012).

2) **Castro, H.G.; Burguener, H.; Paz, R.R.; De Bortoli, M.E.**; "Desarrollo de una interfaz gráfica para un código abierto de elementos finitos", II Jornadas de Investigación en Ingeniería del NEA y Países Limítrofes. ISBN: 978-950-42-0142-7. UTN Facultad Regional Resistencia, Chaco, Argentina (2012).

3) **Castro, H.G.; Paz, R.R.; Sonzogni, V.**; "Synthezised turbulence with time and space correlation for Large Eddy Simulations", XXX Congreso sobre Métodos Numéricos y sus Aplicaciones, Rosario, Sante Fe, Argentina (2011).

4) **Castro, H.G.; Paz, R.R.; Storti, M.; Sonzogni, V.; Marighetti, J.O.; De Bortoli, M.E.**; "Experimental and numerical study of the aerodynamic behaviour of a simplified road vehicle", Mecom - Cilamce 2010, Buenos Aires, Argentina (2010).

5) **Sonzogni, V.; Castro, H.G.; Paz, R. R.; Balbastro, G.; Storti, M.** "Uso de computación de alto desempeño en ingeniería", XXXIV Jornadas Sud-Americanas de Ingeniería Estructural, San Juan, Argentina (2010).

6) **Sonzogni, V.; Castro, H.; Paz, R.; Balbastro, G.; Storti, M.**; "Experiencias en el cálculo paralelo en el CIMEC", Primer Congreso sobre los métodos numéricos en la enseñanza, la ingeniería y las ciencias - EMNUS 2010, Agosto de 2010, UTN, Facultad Regional Haedo, Argentina.

7) **Castro, H.G.; Paz, R.R.; Storti, M.; Sonzogni, V.; Dalcin, L.**; "Hybrid Parallel Programming Technique on a Finite Element Code", II MACI, diciembre de 2009, Rosario, Santa Fe, Argentina.

8) **Castro, H.G.; Paz, R.R.; Storti, M.; Sonzogni, V.; Dalcin, L.**; "Parallel Implementation of a FEM Code by Using MPI/PETSc and OpenMP Hybrid Programming Techniques", XVII Congreso sobre Métodos Numéricos y sus Aplicaciones, noviembre de 2009, Tandil, Argentina.

9) **Storti, Mario A.; Castro, Hugo G.; Paz, Rodrigo R.; Dalcin, Lisandro D.**; "The FastMat2 Matrix Library. Description and Parallel Implementation". XVII Congreso sobre Métodos Numéricos y sus Aplicaciones, noviembre de 2009, Tandil, Argentina.

References

Abramowitz M. and I. S. *Handbook of Mathematical Functions: with Formulas, Graphs, and Mathematical Tables*. Dover Publications, 1970. 29

Ahmed S.R., Ramm G., and Faltin G. Some salient features of the times-averaged ground vehicle wake. *Society of Automotive Eng., Inc*, 1:1–31, 1984. xi, 40, 70, 71, 72, 77

Baba-Ahmadi M. and Tabor G. Inlet conditions for les using mapping and feedback control. *Computer & Fluids*, 38:1299–1311, 2009. 11

Badia S. and Codina R. On some fluid-structure iterative algorithms using pressure segregation methods. Application to aeroelasticity. *International Journal for Numerical Methods in Engineering*, 72:46–71, 2007. xiii, 57, 59

Basara B., Przulj V., and Tibaut P. On the calculation of external aerodynamics industrial benchmarks. *SAE paper*, 2001-01-0701, 2001. 71

Batchelor G. *The Theory of Homogeneous Turbulence*. Cambridge University Press, 1982. 16

Bathe K.J. and Zhang H. Finite element developments for general fluid flows with structural interactions. *International Journal for Numerical Methods in Engineering*, 60:213–232, 2004. xi, xii, 56, 108, 109

Batten P., Goldberg U., and Chakravarthy S. Interfacing statistical turbulence closures with large-eddy simulation. *AIAA paper 42-485*, 2004. 26, 48, 105

Bendat J. and Piersol A. *Measurement and Analysis of Random Data*. John Wiley & Sons, Inc., 1967. 21

Berselli L., Iliescu T., and Layton W. *Mathematics of Large Eddy Simulation of Turbulent Flows*. Springer, 2006. 9

Braun A. and Awruch A. Numerical simulation of the wind action on a long-span bridge deck. *Journal of the Brazilian Society of Mechanical Sciences and Engineering*, 25:352 – 363, 2003. ISSN 1678-5878. 63

Brooks A. and Hughes T. Streamline upwind/Petrov-Galerkin formulations for convection dominated flows with particular emphasis on the incompressible Navier-Stokes equations. *Computational Methods in Applied Mechanichs and Engineering*, 32:199–259, 1982. 4

Cheng S., Tsubokura M., Nakashima T., Nouzawa T., and Okada Y. A numerical analysis of transient flow past road vehicles subjected to pitching oscillation. *Journal of Wind Engineering and Industrial Aerodynamics*, 98:511–522, 2011. 71, 84

Cheng S., Tsubokura M., Nakashima T., Okada Y., and Nouzawa T. Numerical quantification of aerodynamic damping on pitching vehicle-inspired bluff body. *Journal of Fluids and Structures*, 30:188–204, 2012. 71, 84

Chong M., Perry A., and Cantwell B. A general classification of three-dimensional flow fields. *Phys. Fluids A*, 2 (5):765–777, 1990. 95

Clausen P., Koh S., and Wood H. Measurements of a swirling turbulent boundary layer developing in a conical diffuser. *Experimental Thermal and Fluid Science*, 6:39–48, 1993. x, 36, 39

REFERENCES

Cooper K. Commercial vehicle aerodynamic drag reduction: historical perspective as a guide. In *Aerodynamics of Heavy Vehicle: Trucks, Buses and Trains*, pages 9–28. Springer, 2004. xvi, 101

Davidson L. Using isotropic synthetic fluctuations as inlet boundary conditions for unsteady simulations. *Advances and Applications in Fluid Mechanics*, 1 (1):1–35, 2007. 36

Dettmer W. and Peric D. A computational framework for fluid-rigid body interaction: Finite element formulation and applications. *Computational Methods in Applied Mechanichs and Engineering*, 195:1633–1666, 2006. 50

di Mare L., Klein M., Jones W., and Janicka J. Synthetic turbulence inflow conditions for large-eddy simulation. *Physics of Fluids*, 18(2):025107, 2006. 12

Donea J. and Huerta A. *Finite Element Method for Flow Problems*. John Wiley & Sons Ltd, 2003. x, 4, 52, 53

Donea J., Huerta A., J. P., and A. R.F. Arbitrary lagrangian-eulerian methods. volume i: Fundamentals. In E. Stein, R. de Borst, and T. Hughes, editors, *Encyclopedia of Computational Mechanics*, pages 413–437. John Wiley & Sons, Ltd, 2004. 49

Dowell E., Crawley E., Curtiss H., Peters D., Scanlan R., and Sisto F. *A Modern Course in Aeroelasticity*. Kluwer Academic Publishers, Dordrecht, 1995. 50

Druault P., Lardeau S., Bonnet J.P., Coiffet F., Deville J., Lamballais E., Largeau J., and Perret L. Generation of three-dimensional turbulent inlet conditions for large-eddy simulation. *AIAA Journal*, 42(3):447–456, 2004. 12

Dubief Y. and Delcayre F. On coherent-vortex identification in turbulence. *Journal of Turbulence*, 1(11), 2000. 39

Durbin P. and Pettersson-Reif B. *Statistical Theory and Modeling of Turbulent Flow*. John Wiley & Sons Ltd, 2001. ix, 17

Farhat C., Lesoinne M., and LeTallec P. Load and motion transfer algorithms for fluid/structure interaction problems with non-matching discrete interfaces: Momentum and energy conservation, optimal discretization and application to aeroelasticity. *Computational Methods in Applied Mechanichs and Engineering*, 157:95–114, 1998. 56, 109

Felippa C., Park K., and Farhat C. Partitioned analysis of coupled mechanical systems. *Computational Methods in Applied Mechanichs and Engineering*, 190:3247–3270, 2001. 50

Fluent Inc. Fluent 12 user's guide. *Latin American Applied Research*, 2010. 13, 61

Franck G. *Aerodinámica de vehículos mediante una resolución de las ecuaciones de Navier-Stokes con cálculo distribuido*. Master's Thesis, Facultad de Ingeniería Química, Universidad Nacional del Litoral, 2004. 72

Franck G., Nigro N., Storti M., and D'Elía J. Numerical simulation of the flow around the ahmed vehicle model. *Latin American Applied Research*, 39:295–306, 2009. 72, 76

Frandsen J. Numerical bridge deck studies using finite elements. part i: flutter. *Journal of Fluids and Structures*, 19:171–191, 2004. 62, 63

Gilliéron P., Chometon F., and Laurent J. Analysis of hysteresis and phase shifting phenomena in unsteady three-dimensional wakes. *Experiments in Fluids*, 35:117–129, 2003. 84

Guilmineau E. Computational study of flow around a simplified car body. *Journal of Wind Engineering and Industrial Aerodynamics*, 96(6-7):1207 – 1217, 2008. ISSN 0167-6105. doi:DOI:10.1016/j.jweia.2007.06.041.

5th International Colloquium on Bluff Body Aerodynamics and Applications. 71

Gürlek C. *Study of the flow around a bus model.* Ph.D. thesis, Dept. of Mechanical Engineering, Çukurova University, 2008. 70

Hinterberger C., García-Villalba M., and Rodi W. Large eddy simulation of flow around the Ahmed body. *Lectures Notes in Applied and Computational Mechanics, The Aerodynamics of Heavy Vehicles: Trucks, Buses and Trains*, McCallen, F. Browand, J. Ross (Eds.), Springer Verlag, 2004. 71, 72

Howard R. and Pourquie M. Large eddy simulation of an Ahmed reference body. *Journal of Turbulence*, 3, 2002. 76

Huang S., Li Q., and Wu J. A general inflow turbulence generator for large eddy simulation. *Journal of Wind Engineering and Industrial Aerodynamics*, 98:600–617, 2010. 12, 13, 14, 19, 26, 28, 30, 34, 35, 47, 89, 102, 105, 110

Hucho W. *Aerodynamics of road vehicles.* SAE Publishing, 1998. 69

Hughes T. and Brooks A. A multi-dimensional upwind scheme with no crosswind diffusion. *In Finite Element Methods for Convection Dominated Flows, ASME ed.*, 34:19–35, 1979. 4

Hunt J., Wray A., and Moin P. Eddies, stream and convergence zones in turbulent flows. Technical Report, Center for Turbulence Research Report, 1988. 38

Kim J., Moin P., and Moser R. Turbulence statistics in fully developed channel flow at low reynolds number. *Journal of Fluid Mechanics*, 177:133–166, 1987. 11

Klein M., Sadiki A., and Janicka J. A digital filter based generation of inflow data for spatially developing direct numerical or large eddy simulations. *Journal of Computational Physics*, 186:652–665, 2003. 12

Kondo K., Murakami S., and Mochida A. Generation of velocity fluctuations for inflow boundary condition of les. *Journal of Wind Engineering and Industrial Aerodynamics*, 67 & 68:51–64, 1997. 12

Kraichnan R. Diffusion by a random velocity field. *The Physics of Fluids*, 13:22–31, 1970. 12, 13

Krajnovic S., Bengtsson A., and Basara B. Large eddy simulation investigation of the hysteresis effects in the flow around an oscillating ground vehicle. *Journal of Fluids Engineering*, 133, 121103, 2011. 71, 84

Krajnovic S. and Davison L. Large eddy simulation of the flow around a simplified car model. In *2004 SAE World Congress*, volume SAE Paper 2004-01-0227. Detroit, Michigan, USA, 2004. 71, 72, 74, 75

Krajnovic S. and Davison L. Flow around a simplified car, Part 1: Large Eddy Simulation. *Journal of Fluids Engineering*, 127:907–918, 2005. 71

Lee S., Lele S., and Moin P. Simulation of spatially evolving turbulence and the applicability of Taylor's hypothesis in compressible flow. *Phys Fluids A*, 4:1521–1530, 1992. 12

Lesieur M. *Turbulence in Fluids.* Springer, 2008. 2, 7, 8, 96

Lienhart H. and Becker S. Flow and turbulence structure in the wake of a simplified car model. *SAE paper*, 2003-01-0656, 2003. 74

Lilly D. The representation of small-scale turbulence in numerical simulation experiments. *Proc, IBM Sci. Comput. Symp. on Environ. Sci.*, pages 195–210, 1967. 9

Liu K. and Pletcher R. Inflow conditions for the large eddy simulation of turbulent boundary

layers: A dynamic recycling procedure. *Journal of Computational Physics*, 219:1–6, 2006. 11

Lund T., Wu X., and Squires K. Generation of turbulent inflow data for spatially-developing boundary layer simulations. *Journal of Computational Physics*, pages 233–258, 1998. 11

Mavriplis D.J. and Yang Z. Achieving higher-order time accuracy for dynamic unstructured mesh mesh fluid flow simulations: Role of the GCL. In *17th AIAA Computational Flow Dynamics Conference*, pages 1–16. 2005. 65

Park K. and Felippa C. A variational principle for the formulation of partitioned structural systems. *International Journal for Numerical Methods in Engineering*, 47:395–418, 2000. 50

Paz R. *Domain decomposition techniques and distributed programming in computational fluid dynamics*. Ph.D. thesis, Universidad Nacional del Litoral, Santa Fe, Argentina, 2006. 4

Paz R., Nigro N., and Storti M. On the efficiency and quality of numerical solutions in CFD problems using the interface strip preconditioner for domain decomposition methods. *International Journal for Numerical Methods in Fluids*, 52(1):89–118, 2006. xvii

Perret L., Delville J., Manceau R., and Bonnet J.P. Generation of turbulent inflow conditions for large eddy simulation from stereoscopic piv measurements. *International Journal of Heat and Fluid Flow*, 27:576–584, 2006. 12

Piomelli U. and Chasnov J. Large-eddy simulations: theory and applications. In D. Henningson, M. Hallbaeck, H. Alfreddson, and A. Johansson, editors, *Transition and Turbulence Modelling*, pages 269–336. Kluwer Academic Publishers, Dordrecht, 1996. 1, 7

Piperno R. and Farhat C. Partitioned procedures for the transient solution of coupled aeroelastic problems. part ii: energy transfer analysis and three-dimensional applications. *Computational Methods in Applied Mechanichs and Engineering*, 190:3147–3170, 2001. 50, 66

Pope S. *Turbulent Flows*. Cambridge University Press, 2003. 3

Rodi W. Comparison of LES and RANS calculation of the flow around bluff bodies. *Journal of Wind Engineering and Industrial Aerodynamics*, 69-71:55–75, 1997. 42

Selvam R., Govindaswamy S., and Bosch H. Aeroelastic analysis of bridges using FEM and moving grids. *Journal of Wind and Structures*, 25(2-4):257–266, 2002. 63

Serre E., Minguez M., Pasquetti R., Guilmineau E., Bo Deng G., Kornhaas M., Schäfer M., Fröhlich J., Hinterberger C., and Rodi W. On simulating the turbulent flow around the Ahmed body: A French-German collaborative evaluation of LES and DES. *Computers & Fluids*, In press, 2011. doi:DOI:10.1016/j.compfluid.2011.05.017. 71

Smirnov A., Celik I., and Shi S. LES of bubble dynamics in wake flows. *Computers and Fluids*, 34:351–373, 2005. 13

Smirnov A., Shi S., and Celik I. Random flow generation technique for large eddy simulations and particle-dynamics modeling. *Journal of Fluids Engineering*, 123:359–371, 2001. 12, 13, 19, 26, 48, 89, 102, 105, 110

Stein K., Tezduyar T., and Benney R. Automatic mesh update with the solid-extension mesh moving technique. *Computational Methods in Applied Mechanichs and Engineering*, 193:2019–2032, 2004. 81

Storti M., Nigro N., Paz R., and Dalcín L. PETSc-FEM: A general purpose, parallel, multi-physics FEM program. 2002. xvii

Storti M., Nigro N., Paz R., and Dalcín L. Strong coupling strategy for fluid-structure interaction problems in supersonic regime via fixed point iteration. *Journal of Sound and Vibration*, 320:859–877, 2009. 57, 110

Svácek P., Feistauer M., and Horácek J. Numerical simulation of flow induced airfoil vibrations with large amplitudes. *Journal of Fluids and Structures*, 23:391–411, 2007. 58

Tabor G. and Baba-Ahmadi M. Inlet conditions for large eddy simulation: A review. *Computers and Fluids*, 39:553–567, 2010. 11, 12

Tennekes H. and Lumley J. *A first course in turbulence.* MIT Press, 1972. 15, 18, 76

Tezduyar T., Franca L., and Balestra M. A new finite element formulation for computational fluid dynamics: V. circumventing the Babuška-Brezzi condition: A stable Petrov-Galerkin formulation of the stokes problem accommodating equal-order interpolations. *Computational Methods in Applied Mechanichs and Engineering*, 59:85–99, 1986. 4

Tezduyar T., Mittal S., Ray S., and Shih R. Incompressible flow computations with stabilized bilinear and linear equal order interpolation velocity-pressure elements. *Computational Methods in Applied Mechanichs and Engineering*, 95:221–242, 1992. 4

Tezduyar T. and Sathe S. Stabilization parameters in SUPG and PSPG formulations. *Journal of Computational and Applied Mechanics*, 4:71–88, 2003. 6

Thacker A., Loyer S., and Aubrun S. Comparison of turbulence length scales assessed with three measurement systems in increasingly complex turbulent flows. *Experimental Thermal and Fluid Science*, 34:638–645, 2010. 32

Uruba V. Lateral vortex dynamics behind ahmed body. In *Proceedings of Applied Mathematics and Mechanics*, volume 10, pages 455–456. 2010. 44

Wagner C., Hüttl T., and Sagaut P. *Large-Eddy Simulation for Acoustics.* Cambridge University Press, 2007. 9

Wittwer A. and Möller S. Characteristics of the low speed wind tunnel of the UNNE. *Journal of Wind Engineering and Industrial Aerodynamics*, 84:307–320, 2000. xiii, 41, 73, 74

Wood R. Impact of advanced aerodynamic technology on transportation energy consumption. *SAE paper*, 2004-01-1306, 2004. 70

Xie Z.T. and Castro I. Efficient generation of inflow conditions for large eddy simulation of street-scale flows. *Flow, Turbulence and Combustion*, 81(3):449–470, 2008. 12